Properties and recrystallization of radiation damaged pyrochlore and titanite

Dissertation with the aim of achieving a doctoral degree at the Faculty of Mathematics, Informatics and Natural Sciences, Department of Geosciences of University of Hamburg

Submitted by Peter Zietlow

2016 in Hamburg

The following evaluators recommend the admission of this dissertation:

Prof. Dr. Ulrich Bismayer

Prof. Dr. Shrinivas Viladkar

Date of the oral Ph.D. defense:

02.11.2016

Contents

Abstract

Radiation damage in minerals is caused by the alpha-decay of incorporated radionuclides, such as U and Th and their decay products. The effect of thermal annealing (400-1400 K) on radiation-damaged pyrochlores has been investigated by Raman scattering, X-ray powder diffraction (XRD), and combined differential scanning calorimetry/thermogravimetry (DSC/TG) (Zietlow *et al.*, in print). The analysis of three natural radiation-damaged pyrochlore samples from Miass/Russia (6.4 wt% Th, $23.1 \cdot 10^{18}$ α-decay events per gram (dpg)), Zlatoust/Russia (6.3 wt% Th, $23.1 \cdot 10^{18}$ dpg), Panda Hill/Tanzania (1.6 wt% Th, $1.6 \cdot 10^{18}$ dpg), and Blue River/Canada (10.5 wt% U, $115.4 \cdot 10^{18}$ dpg), are compared with a crystalline reference pyrochlore from Schelingen (Germany). The type of structural recovery depends on the initial degree of radiation damage (Panda Hill 28 %, Blue River 85 %, Zlatoust and Miass 100 % according to XRD), as the recrystallization temperature increases with increasing degree of amorphization. Raman spectra indicate reordering on the local scale during annealing-induced recrystallization. As Raman modes around 800 cm^{-1} are sensitive to radiation damage (Vandenborre & Husson 1983, Moll *et al.* 2011), the degree of local order was deduced from the ratio of the integrated intensities of the sum of the Raman bands between 605 and 680 cm^{-1} devided by the sum of the integrated intensities of the bands between 810 and 860 cm^{-1}. The most radiation damaged pyrochlores (Miass and Zlatoust) show an abrupt recovery of both, its short- (Raman) and long-range order (X-ray) between 800 and 850 K. The volume decrease upon recrystallization in Zlatoust pyrochlore was large enough to crack the sample repeatedly. In contrast, the weakly damaged pyrochlore (Panda Hill) begins to recover at considerably lower temperatures (near 500 K), extending over a temperature range of ca. 300 K, up to 800 K (Raman). The pyrochlore from Blue River shows in its initial state an amorphous x-ray diffraction pattern superimposed by weak Bragg-maxima that indicates the existence of ordered regions in a damaged matrix. Unlike the other studied pyrochlores, Raman spectra of the Blue River sample show the appearance of local modes above 560 K between 700 and 800 cm^{-1} resulting from its high content of U and Ta impurities. DSC measurements confirmed the observed structural recovery upon annealing. While the annealing-induced ordering of Panda Hill begins at a lower temperature (ca. 500 K) the recovery of the highly-damaged pyrochlore from Miass occurs at 800 K. The Blue-River pyrochlore shows a multi-step recovery which is similarly seen by XRD. Thermogravimetry showed a continuous mass loss on heating for all radiation-damaged pyrochlores (Panda Hill ca. 1%, Blue River ca. 1.5%, Miass ca. 2.9%).

Abstract

In order to elucidate local phenomena by NMR spectroscopy, a simpler structure of a metamict mineral such as titanite has been chosen. Hence, metamict titanite from Cardiff uranium mine (M28696) in Ontario, Canada, has been analysed using ^{29}Si magic angle spinning nuclear magnetic resonance spectroscopy (MAS NMR) (Zietlow *et al.*, 2014). A broad Gaussian shaped NMR signal at -81 ppm occurs at room temperature resulting from the mainly short range ordered metamict structural state. NMR signals were obtained at room temperature and after annealing at 600, 950, 1220 and 1470 K. Because of increasing crystallinity the full width at half maximum (FWHM) decreased from 24 ppm to 20 ppm respectively using a Pseudo-Voigt fit. For comparison well crystalline titanite from Rauris showed an NMR signal at -79.3 ppm with FWHM of 4.1 ppm and an almost Lorentzian profile because of its good long range order. Integrating synchrotron X-ray diffraction (XRD) signals of Cardiff titanite show an increase of the long range order at annealing temperatures considerably lower than the short range ordering seen by NMR.

1 Radiation damaged materials

1.1 Introduction

Ideal crystals are defined by their long range ordered periodicity (Friedrich, Knipping & Laue 1912). It is the lowest energetic state of atomic arrangements. This order can be disrupted by defects, e.g. interstitials, dislocations or inclusions. Radiation damage of the crystalline structure leads to disturbed periodicity and occurs when α-particles are emitted by decaying nuclei incorporated in the mineral (Ewing 1994). The order of the structure will be destroyed and the system can become completely amorphous by percolation and overlapping recoil cascades on the geological timescale. Depending on the degree of damage and chemical composition such damages will heal, e.g., by applying thermal treatment (Lumpkin & Ewing 1988).

Metamict minerals show preserved macroscopic crystallite shape (Ewing 1994). Their crystallographic long range order, however, disappears. Radiation damage, resulting from the decay of built-in thorium or uranium atoms, includes multiple overlapping processes starting with the α-decay, followed by the displacement of the primary knock-on recoil nucleus and its follow-up atomic displacement cascade, interactions of the emitted alpha particles, immediate healing processes, and the exchange of water or hydroxyl groups. The mineral stays in a resulting metastable radiation-damaged state until it receives enough energy to restore its former order.

Amorphization kinetics is controlled by stoichiometry, crystal structure and present lattice defects (Ewing 1994; Weber *et al.* 1998). Several intermediate domain structures were observed in metamict minerals with a distinct difference of border and core damaged volumes (Lumpkin & Ewing 1988). On different length scales, distinct structural changes are possible. Each atomic rearrangement can contribute to macroscopic material instability. Changes can be probed by analysing techniques sensitive to the crystallographic long range order (e.g. XRD, >300 Å), in the polyhedral neighbourhood (e.g. vibrational or NMR spectroscopy), on an atomic scale (e.g. TEM) or as a material property (e.g. DTA/TGA).

In nature several minerals are known to incorporate actinides while keeping their crystallographic long range order intact up to high irradiation doses, e.g. pyrochlore, perovskite, titanite, zircon, apatite, monazite or xenotime (G. R. Lumpkin & Geisler-

1.1 Introduction

Wierwille 2012). Radiation damages are known to have lifetimes of hundreds of millions of years until they heal; hence the recrystallization kinetics is very slow.

Synthetic, and to a smaller extent natural pyrochlores with a broad range of different cation substitutes have been thoroughly investigated (Lima-de-Faria 1958; Lumpkin, Foltyn, *et al.* 1986; Lumpkin & Ewing 1988; Digeos *et al.* 2003; Lian *et al.* 2003; Ewing *et al.* 2004; Strachan *et al.* 2005; Jafar *et al.* 2014). Structural damage has been studied after ion irradiation or actinide doping with several techniques due their different length-scale sensitivities (Weber *et al.* 1998).

Radiation damage and its healing behaviour upon thermal annealing is not only of pure crystallographical interest, but also to material sciences, especially in the context of a durable embedding material for highly radioactive nuclear waste (HLW) and spent nuclear fuel (Weber *et al.* 1998; G. R. Lumpkin & Geisler-Wierwille 2012). Pyrochlore ceramics are among other compounds considered as embedding materials for the long-term deposit of high-level radioactive waste, mainly produced in nuclear fission reactors. After long storage periods, actinides from spent nuclear fuel become the most active radionuclides and take over the radiotoxicity of other long-lived fission products like ^{99}Tc and ^{129}I (Hedin 1997; Ewing 2008; Ewing 2011).

Actinides U, Np, Pu, Am and Cm remaining from electric power generation and from the dismantling of nuclear weapons contribute to HLW (Weber *et al.* 1998; G. R. Lumpkin & Geisler-Wierwille 2012). While long living fission products like ^{99}Tc and ^{93}Zr are the most toxic radioactive nuclei for the human body upon ingestion or inhalation from some decades after the fission process on (Hedin 1997). They stay the most toxic isotopes for some hundred years. Actinides eventually become the most radiotoxic isotopes in the long run (see Fig. 1). All countries producing nuclear power nowadays consider the storage of HLW in geological 'stable' national repositories, concerning hundred thousands of years of disposal, until radiotoxicity of the embedded nuclei would become negligible. Although HLW accrue since the 1940's, none of the meanwhile 30 countries operating nuclear weapons and/or power plants have decided on a permanent HLW repository site yet. Licensing processes in Finland, France and Sweden are the first to start in the next years (International Atomic Energy Agency 2015).
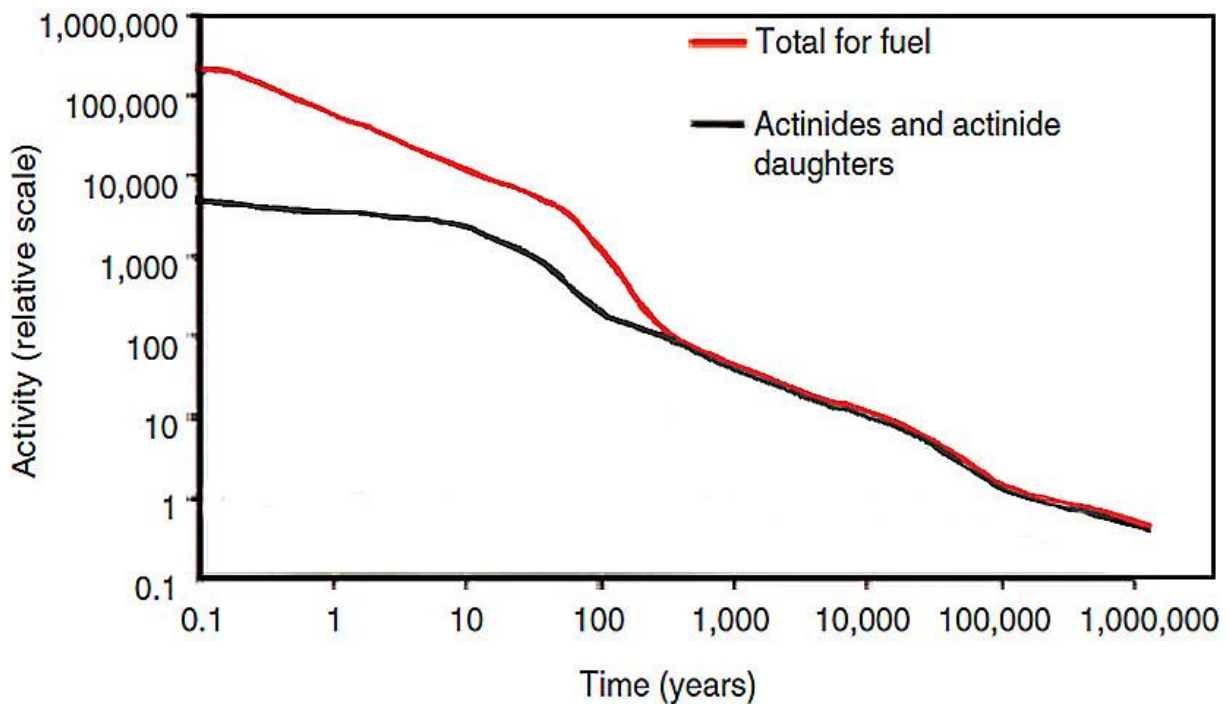
1.1 Introduction

Fig. 1. Radiotoxicity of actinides relative to U ore (modified after Hedin, 1997).

Because of their long term stability despite incorporating actinides, pyrochlore-type compounds and their properties have been analysed in great detail. Several studies emphasize the critical amorphization dose for synthesized pyrochlores of varying compositions (Lumpkin *et al.* 2001; Strachan *et al.* 2005; Ewing 2006; Park *et al.* 2014; Yudintsev *et al.* 2015) and leaching processes (Shoup *et al.* 1997; Lumpkin 2001; Begg *et al.* 2001; Zhang *et al.* 2001; Icenhower *et al.* 2003; Geisler *et al.* 2004; Lumpkin *et al.* 2004). Knowledge of the thermodynamic stability and physical properties is, however, still limited (Lumpkin, Foltyn, *et al.* 1986; Li *et al.* 2014).

In contrast to low and intermedium level nuclear waste, HLW radioactivity produces a considerable amount of heat (more than a few Watts per litre). In order to cool it is stored for decades in water ponds or steel caskets like the German "CASTOR", embodied in a borosilicate medium, at the sites of the more than 400 nuclear power reactors worldwide (International Atomic Energy Agency 2015). The embedding for a geological timescale requires a good leaching resistance. Radiation damage is known to disintegrate the crystallographic structural order leading to changes in mechanical properties which in the end would contribute to a raised solubility of incorporated radioactive nuclides (Begg *et al.* 2001).

1.1 Introduction

Pyrochlore is the main component of the "Synroc-F" concept (standing for synthetic rock) considered for some time in Australia and the US for actinide storage, but eventually abandoned in favour of mixed oxide (MOX) reprocessing technology (G R Lumpkin & Geisler-Wierwille 2012). Compared to most other considered materials, pyrochlore with the general formula $A_2B_2O_7$ has the advantage of allowing the incorporation of a broad range of cations with different charges and radii in its structure, especially at the A-site (Atencio *et al.* 2010; Cai *et al.* 2011). Instead of the common Ca and Na, pyrochlore minerals can built-in REEs, Y, Sn, Sr, Pb, Sb, Bi or actinides at the A site. Sn or W can replace B-site atoms. Natural pyrochlores are niobates ("pyrochlores" in strict sense), tantalates ("microlites") or titanates ("betafites"), that can incorporate a large amount of fluorine, OH^- groups or H_2O in their structure. To prevent a critical mass in the actinide matrix, some neutron absorbers like Gd or Hf should be present in the future embedding material − both can occur in the pyrochlore structure (G. R. Lumpkin & Geisler-Wierwille 2012). Therefore, synthetic Gd titanates and zirconates or rare earth hafnates are the most studied pyrochlores with respect to radiation damage or damage prevention .

Many studies of pyrochlore as a possible embedding material analyse critical radiation doses with respect to composition, as well as about leaching processes. Some studies also include the annealing behaviour (Yehuda Eyal & Fleischer 1985; Eyal *et al.* 1987). Most analyses focus on synthetic ion irradiated or radionuclide doped samples. The advantage of these studies is a rather defined structural and chemical actinide environment. Natural minerals, in contrast, have the advantage of carrying the information on disorder changes in the relevant geological timescale, and possibly show damaging and healing mechanisms closer to future embedding materials than those produced by artificial ion irradiation. The objective of this thesis is therefore to contribute to the understanding of the thermal annealing behaviour of pyrochlore and titanite (which has a simpler structure) and to relate local structural changes with features determined by the long range crystallographic order. Its emphasis is in the polyhedral rearrangement visible in Raman and NMR spectroscopy. Observed changes are related to long range annealing behaviour analysed by XRD. The influence of the initially damaged fraction upon the annealing behaviour is of special interest and will be described in detail.

1.2 Metamict minerals

Introduced in 1893 by the Norwegian mineralogist Brøgger the term "metamikte" was used to describe a special kind of amorphous material showing conchoidal fracture and optical isotropy but conserved crystal shape (Ewing 1994). Some metamict minerals release a significant amount of energy on heating, the so called "pyrognomic" behaviour which was first described by Berzelius (Berzelius 1815) for gadolinite and named by Scheerer (Scheerer 1840). Metamictization and its recovery were analysed by observing changes in density, refractive indices and unit cell volume, especially in zircons as they could be used for absolute age determination (Holland & Gottfried 1955). Isotropy on the crystallographic length scale was first described by (Vegard 1916) for metamict thorite ($ThSiO_4$) via powder X-ray diffraction. Goldschmidt (Goldschmidt 1924) stated as criteria for metamictization:

- weakly ionic structure possibly susceptible to hydrolysis,
- ions which may change their "state of ionization" under ambient conditions,
- exposed to strong radiation.

The idea of radioactivity causing the isotropization was first mentioned by Hamberg (1914) - almost two decades after Becquerel discovered radioactivity. For zircons Holland and Gottfried (1955) described the periodic-to-aperiodic transition as going along with

- 10^{15}-10^{16} α-decay events/mg,
- a density decrease of 17 %,
- a decrease in birefringence up to complete isotropy,
- anisotropic unit cell expansion of 5 %.

Metamictization has been observed in several actinide-bearing minerals including zirconolite (Lumpkin, Foltyn, *et al.* 1986; Lumpkin, Ewing, *et al.* 1986), brannerite (Lumpkin *et al.* 2012), titanite (Vance & Metson 1985; Hawthorne *et al.* 1991; Bismayer *et al.* 2010; Beirau 2012), zircon (Salje *et al.* 1999; Nasdala *et al.* 2001), monazite (Meldrum *et al.* 1996; Mathieu *et al.* 2001), apatite (Carpena *et al.* 1988), allanite, britholite (Arden & Halden 1999) or pyrochlore (Lumpkin & Ewing 1988). An overview is given by (G. R. Lumpkin & Geisler-Wierwille 2012). Not all structures lose their periodic long-range structure even on high radiation doses, e.g. thorianite (ThO_2) or uraninite (UO_2) (Weber 1981).

1.3 α-decay

Unstable nuclei decay (Meschede 2004). For α-decay, a helium core is ejected from the mother isotope X, leaving the daughter isotope Y with two protons and two neutrons less.

$$_Z^A X \rightarrow {}_{Z-2}^{A-4}Y + {}_2^4He^{2+} + energy$$
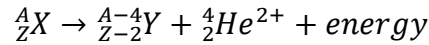
Thorium and uranium are the most common radioactive elements on earth's crust, except from β-decaying ^{40}K (https://earthref.org/GERMRD/). Upon α-decay with half-life times in the order of billions of years (λ_{U238} 4.5 Ga, λ_{U235} 0.7 Ga and λ_{Th232} 14.0 Ga (Meija *et al.* 2016) they produce He^{2+} particles and transform into lighter daughter isotopes. Their decay chains (Fig. 2) end with stable lead isotopes ^{206}Pb, ^{207}Pb and ^{208}Pb, including 8, 7 and 6 α-decay events, respectively. Most decay products have short half-life times of nanoseconds up to 5.8 years. Only four isotopes (^{234}U, ^{230}Th and ^{226}Ra resulting from ^{238}U decay and ^{231}Pa from ^{235}U decay) have half-lives of millennia and more.

Fig. 2. Decay series of radioactive isotopes occurring in natural pyrochlore, and their half-life times (Meija *et al.* 2016).

2 Metamict pyrochlore

2.1 Crystalline structure

Mineralogically, pyrochlore is catalogued under 04.DH.15 oxides and hydroxides, metal:oxygen = 1:2 and similar with large (± medium-sized) cations; sheets of edge-sharing octahedral (Strunz & Nickel 2001). Dana (Dana *et al.* 1997) groups it under 08.02.01.01 multiple oxides with Nb, Ta, Ti where $(A)_2 (B_2O_6) (O, OH, F)$ and Nb>Ta; (Nb+Ta)>2(Ti).

The pyrochlore structure ($NaCaNb_2O_7$) is a derivative of face centred cubic CaF_2 (Fig. 3). The cation sites are occupied by two different species (Wyckoff positions 16c and 16d). 16d sites (0, 0, 0) are occupied by A-cations Na^+, Ca^{2+}, REE, actinides or stay vacant. In nature, octahedral coordinated 16c B-site cations (1/2, 1/2, 1/2) are frequently Nb^{5+}, Ta^{5+} or Ti^{4+}, but can be substituted by Sb^{5+}, W, V^{5+}, Sn^{4+}, Zr, Hf, Fe^{3+}, Mg, Al or Si. The anion site is either occupied by oxygen in 48f position (x, 1/8, 1/8) and oxygen, fluorine, OH^-, H_2O or vacancies in 8b or Y position (1/8, 1/8, 1/8). Oxygen in 48f sites is tetrahedral coordinated (Fig. 4). The unit cell consists of 88 atoms (Z=8). The lattice parameter is around 1.04 nm. After the classification of Atencio *et al.* (Atencio *et al.* 2010) the species with Nb+Ta > 2Ti and Nb > Ta are called pyrochlores as such. Species with Ta as dominant 16c cation are called microlite and Ti-pyrochlores betafite.

2.1 Crystalline structure
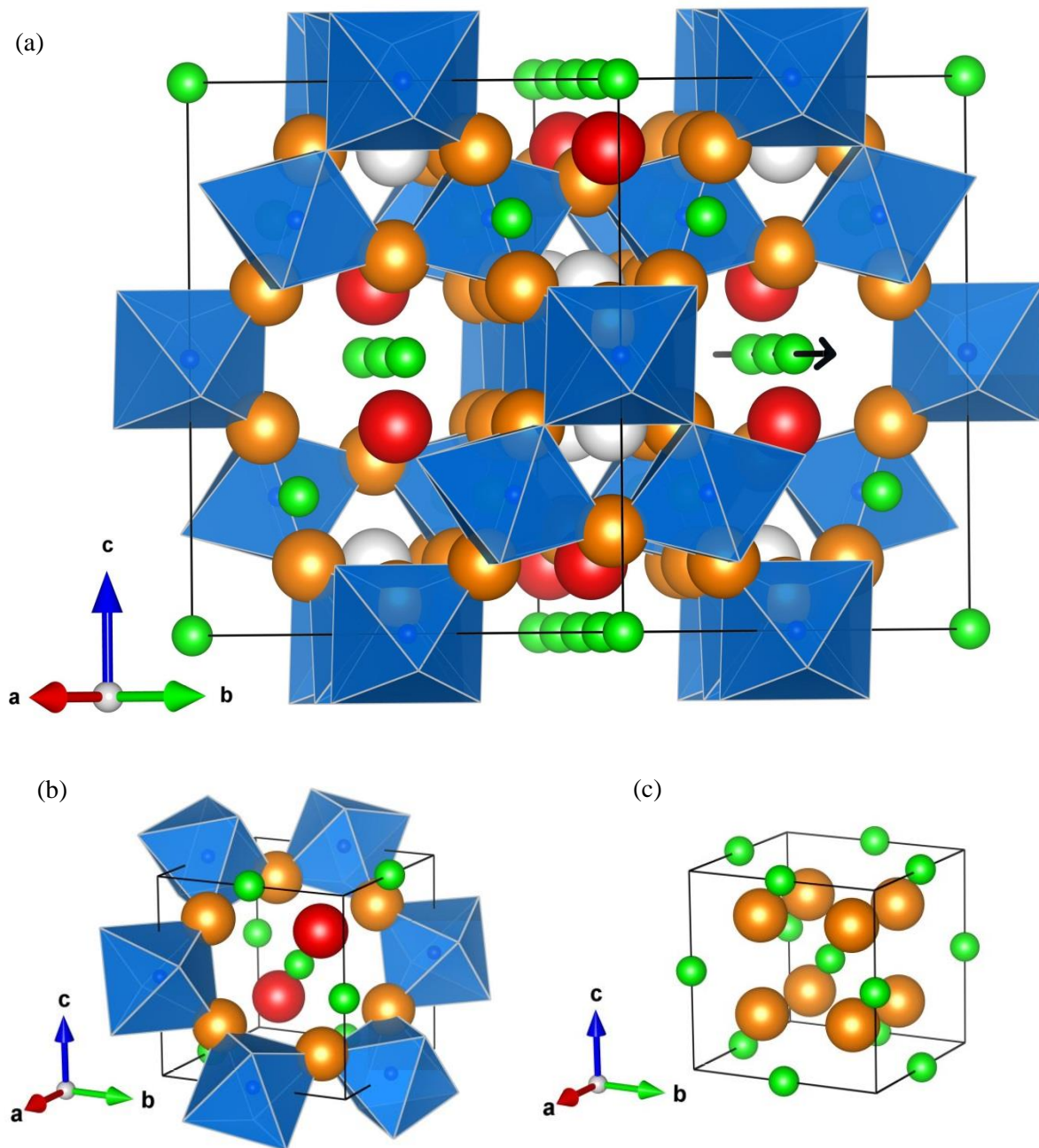
Fig. 3. (a) Pyrochlore structure with A-site cations (green), B-site cations (centres of octahedra), X-site oxygen anions (orange), Y-site anions (red) and vacancies compared to fluorite structure (white). The arrow marks channels of A-site cations along [110]. (b) A structural fragment along [111] visualizing a ring of corner-sharing BX_6 octahedra. (c) Fluorite unit cell.

There is only one free atomic coordinate parameter in an ideal pyrochlore unit cell: the x-parameter of 48f oxygens. It ranges from 0.375 to 0.4375, resulting in either undistorted A-site cubes (for 0.375), undistorted B-site octahedra (for x=0.4375) or anything between (Lumpkin & Ewing 1988).

2.1 Crystalline structure

Oxygen atoms are tetrahedrally coordinated – either in A_2B_2- (48f-site oxygen atoms) or tetragonal A_4-configuration (8b-site oxygen atoms), shown in Fig. 4. Oxygen coordination is used to calculate a tolerance factor for site occupation in the pyrochlore structure, e.g. in a study of 315 compositions (Cai *et al.* 2011).

Fig. 4. (a) Tetragonal oxygen coordination in 1/8 pyrochlore unit cell. (b) A_2B_2 coordination of 48f oxygen atoms. (c) A_4 coordination of 8b anions. (Cai *et al.* 2011)

2.2 Structural damage

Decay energies of the emitted α-particles (between 4.5-5.8 MeV in the whole decay chain) ionize atoms on their alpha-recoil tracks of around 15-20 µm length (see Fig. 5, (G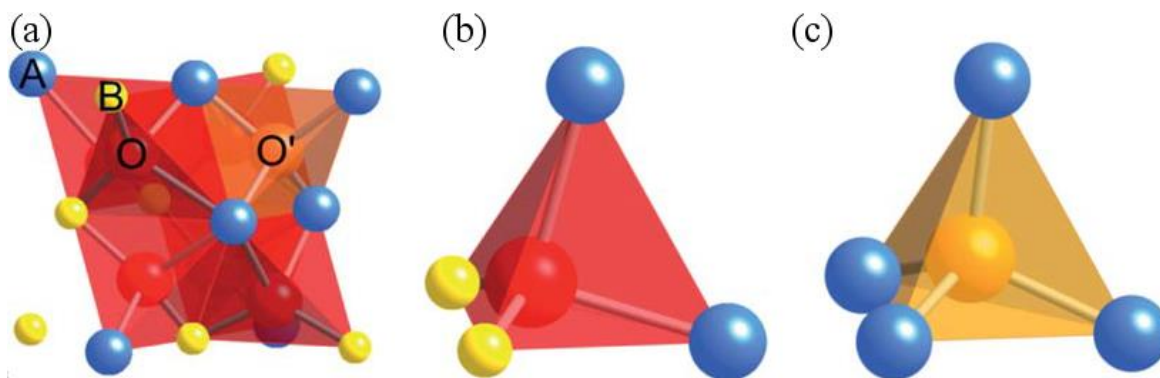. R. Lumpkin & Geisler-Wierwille 2012)). At the end of their paths, their kinetic energy is low enough to displace some hundred atoms. The main displacement takes place through a cascade of Frenkel pairs (vacancy-interstitial pairs, 70 − 100 keV) knocked on by the decaying heavy atom which is recoiled by the α-particle emission. The resulting displacement avalanche leads up to some thousand lattice defects depending on the host material (e.g. ca. 2300 in $Gd_2Zr_2O_7$ pyrochlore after 0.5 ps and ca. 8800 in $Gd_2Ti_2O_7$ pyrochlore after 0.8 ps (Urusov *et al.* 2014), ca. 1000 atoms in $CaTiSiO_5$ titanite (Trachenko *et al.* 2001)), relaxing to the metastable state of some dozen displacements after several picoseconds. Another study estimated lattice defects in the order of just some 80 Frenkel pairs for irradiated uraninite UO_2 single crystals (Weber 1981). The whole structural damage process takes place within some picoseconds and is accompanied by immediate partial healing if the temperature is above absolute zero (Archer *et al.* 2014). In dependence of present thermal energy, there is also some reordering over geological timescale or related to shorter-term thermal geological events, respectively (Lumpkin & Ewing 1988). β-decays only contribute in the order of 0.1 displacements per decay event (Ewing 2011), so that they are almost negligible for structural order changes.

Fig. 5. Schematic representation of an α-decay event.
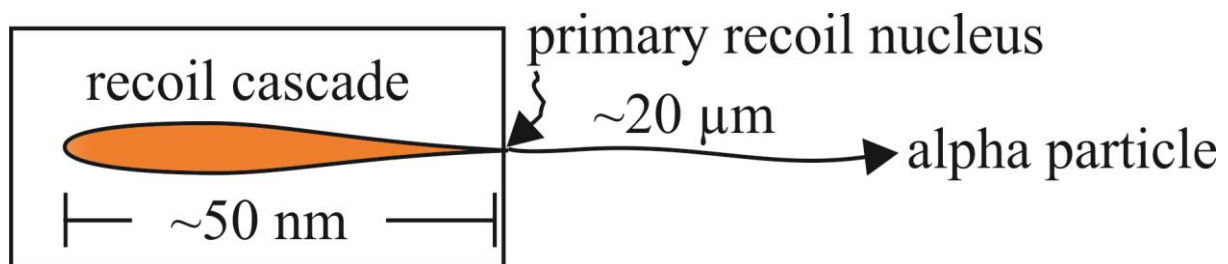
Irradiation studies of natural pyrochlores and synthetic rare earth titanates have been carried out by Lumpkin and Ewing (1988) and Lian *et al.* (2003), respectively. The authors described several steps of increased disorder prior to amorphization in their high-resolution transmission electron microscopy (HRTEM) and selected area electron diffraction (SAED) studies.

2.2 Structural damage

In pyrochlore, actinides occupy the 16d Wyckoff positions. Under continued irradiation, recoil paths overlap and, although they are simultaneously healed in parts, the process leads to increasing amorphization with time. From TEM images and X-ray diffraction patterns five steps of amorphization with increasing radiation have been distinguished, starting with (1) a "mottled" diffraction contrast, then (2) isolated aperiodic regions extending 1-5 nm, then (3) coexistence of aperiodic and crystalline nanoregions, (4) predominant amorphous matter with relict crystalline "islands" and, eventually, (5) the lattice fringe periodicity is completely lost, and hence, the metamict state is established (Lumpkin & Ewing 1988; Lian *et al.* 2003). Critical amorphization doses are reported in the order of 10^{18} to 10^{20} α-decay events per gram. Other typical effects include changes in the unit cell parameters, as well as loss of hydrous species incorporated in the radiation-damaged structure. X-ray diffraction studies of radiation-damaged pyrochlore revealed critical radiation doses in the range of (0.2-12) x 10^{18} alpha decays per gram (Lumpkin & Ewing 1988). Cell parameters in this transition zone are reported to increase. A mean lifetime of 100 Ma was estimated for singular alpha-recoil tracks.

Extended X-ray absorption fine structure / X-ray absorption near edge structure (EXAFS/XANES) analyses (Greegor *et al.* 1985; Greegor *et al.* 1989; Aluri & Grosvenor 2014) of metamict pyrochlore group minerals and synthetic titanates showed a reduction in coordination number and minor changes in bond distances for nearest B-site neighbours, but strong disorder in the second coordination sphere upon annealing.

Synthetic pyrochlore-type materials have been extensively studied by Raman spectroscopy and the observed Raman signals have been assigned to certain phonon modes on the basis of model calculations. Several vibrational modes of components having the pyrochlore structure type have been assigned and compared with model calculations (Vandenborre *et al.* 1983; Mihailova *et al.* 1997; Begg *et al.* 2001; Kamba *et al.* 2002; Ronconi & Alves 2003; Hong *et al.* 2003; Geisler *et al.* 2004; Fischer *et al.* 2008; Lummen *et al.* 2008; Arenas *et al.* 2010; Sattonnay *et al.* 2010; Radhakrishnan *et al.* 2011; Moll *et al.* 2011; Park *et al.* 2014; Kulriya *et al.* 2015).

Differential thermal and thermogravimetric analysis (DTA/TGA) of moderately to fully metamict, altered, natural pyrochlores by Lumpkin *et al.* (Lumpkin, Foltyn, *et al.* 1986) found strong exothermic reactions around 680 to 700 K accompanied by a total weight loss of 1.0 to 7.2 % (Tomašić *et al.* 2008).

2.2 Structural damage

Urusov *et al.* (Urusov *et al.* 2014) and Gunn *et al.* (Gunn *et al.* 2012) performed molecular dynamic calculations on the pyrochlore structure. A recent simulation by Archer *et al.* (Archer *et al.* 2014) of radiation damage by a primary knock on atom in $Gd_2Ti_2O_7$ pyrochlore showed large regions of anion disordered pyrochlore (anions distributed over 8a- and 8b-sites) with only minor amorphization at the boundary of the cascade (Fig. 6). The authors applied an order parameter to represent different structural disorder: ideal pyrochlore, an anion disordered pyrochlore, defect fluorite, two intermediate and the amorphous phase.
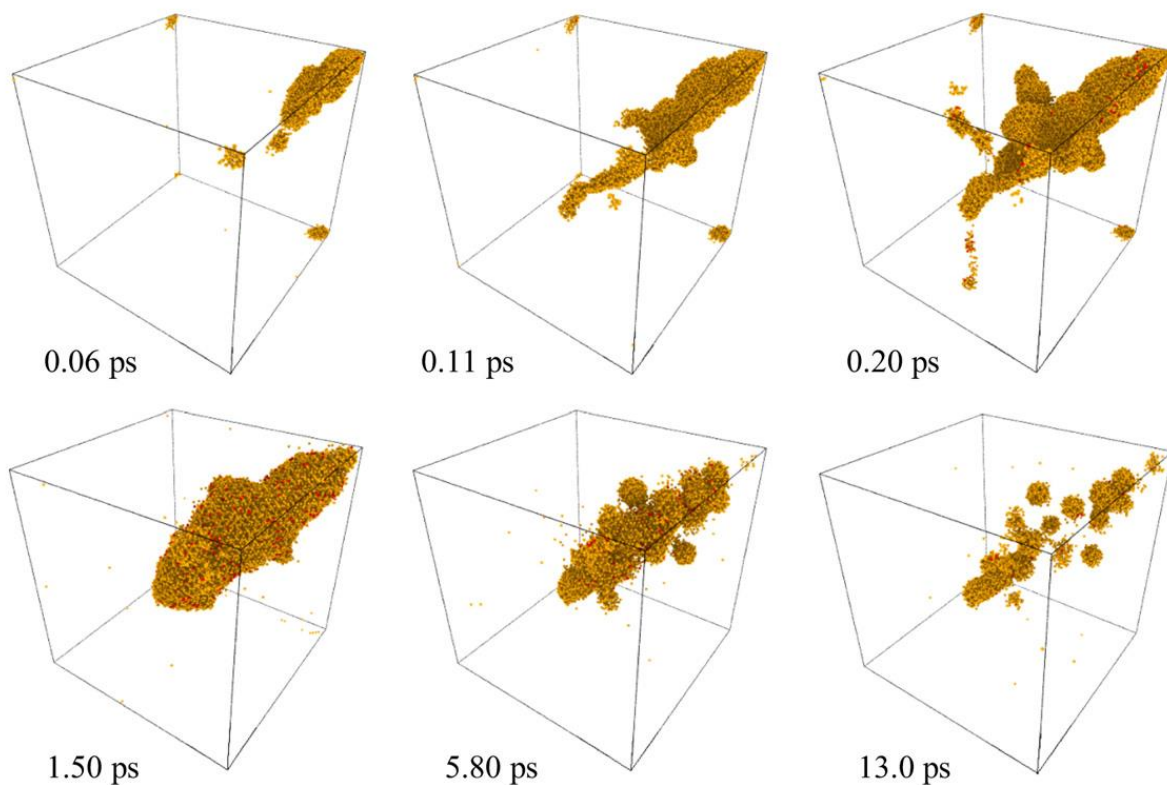
Fig. 6. Modelled recoil cascade in pyrochlore structure ($Gd_2Ti_2O_7$) 0.06, 0.11, 0.20, 1.5, 5.8 and 13 ps after the decay event with orange spheres representing regions of anion disordered pyrochlore (Archer *et al.* 2014). Red spheres represent amorphous areas. Cube sides are 14 Å.

Apart from Frenkel pairs and anion defects preceding a complete metamictization, disorder has also been reported for the cation sites (16c and 16d), (Sattonnay & Tétot 2014). For an atomistic $Gd_2Ti_2O_7$ simulation, the authors found a reduced oxygen-coordination for the Ti-antisite (see Fig. 7).

2.2 Structural damage

Fig. 7. Distortions from cation anti-site defects in $Gd_2Ti_2O_7$ (Sattonnay & Tétot 2014) with initial cation exchange (a) and consequently moved downwards Ti atom (grey), now in fivefold coordination (b).

Overlapping alpha-recoil tracks eventually form clusters. In SAED diffractograms of HRTEM pictures, areas of 1-5 nm in diameter are characterized by "mottled" diffraction contrast (Lumpkin & Ewing 1988). Crystallites of 50-100 nm size dominated up to 0.7 displacements per atom due to radiation. With radiation doses larger 7×10^{15} decay events per mg only small crystalline islands with sizes of 15 nm remained. In excess of 1 displacement per atom no long range order was observed in natural pyrochlores whatsoever.
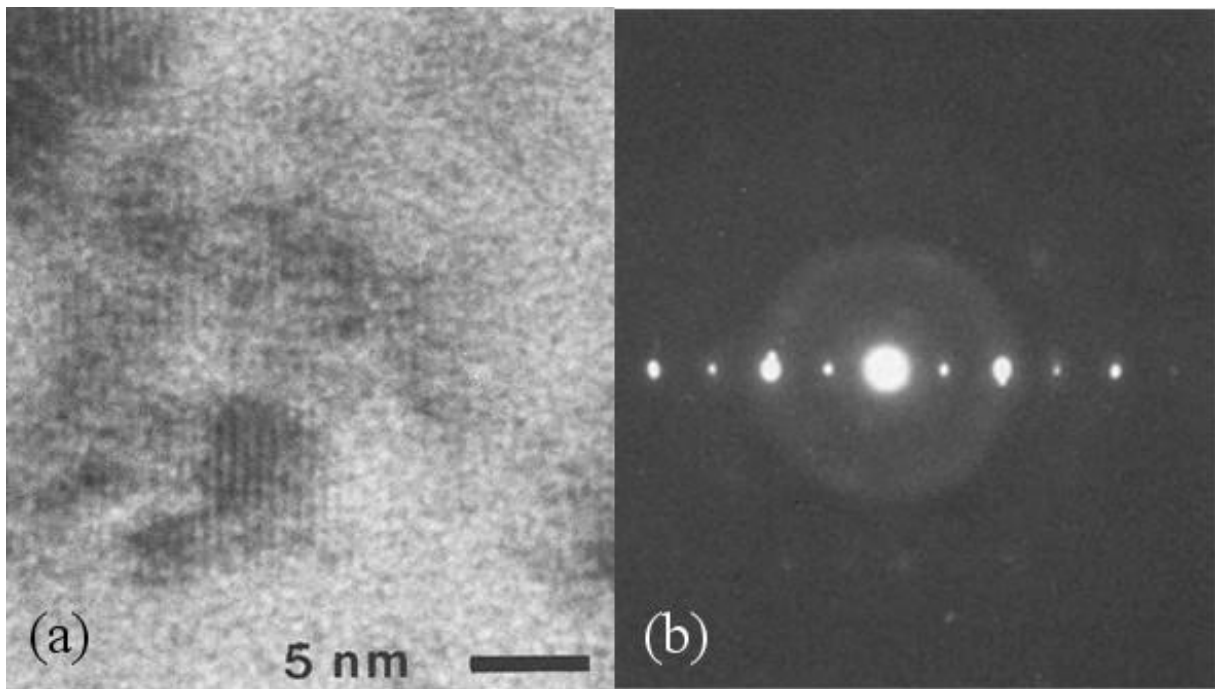
Fig. 8. (a) HRTEM image showing a heavily radiation-damaged Harding microlite by a dose of 7×10^{18} α-decays/g. (b) SAED pattern of (111) zone (Lumpkin & Ewing 1988).
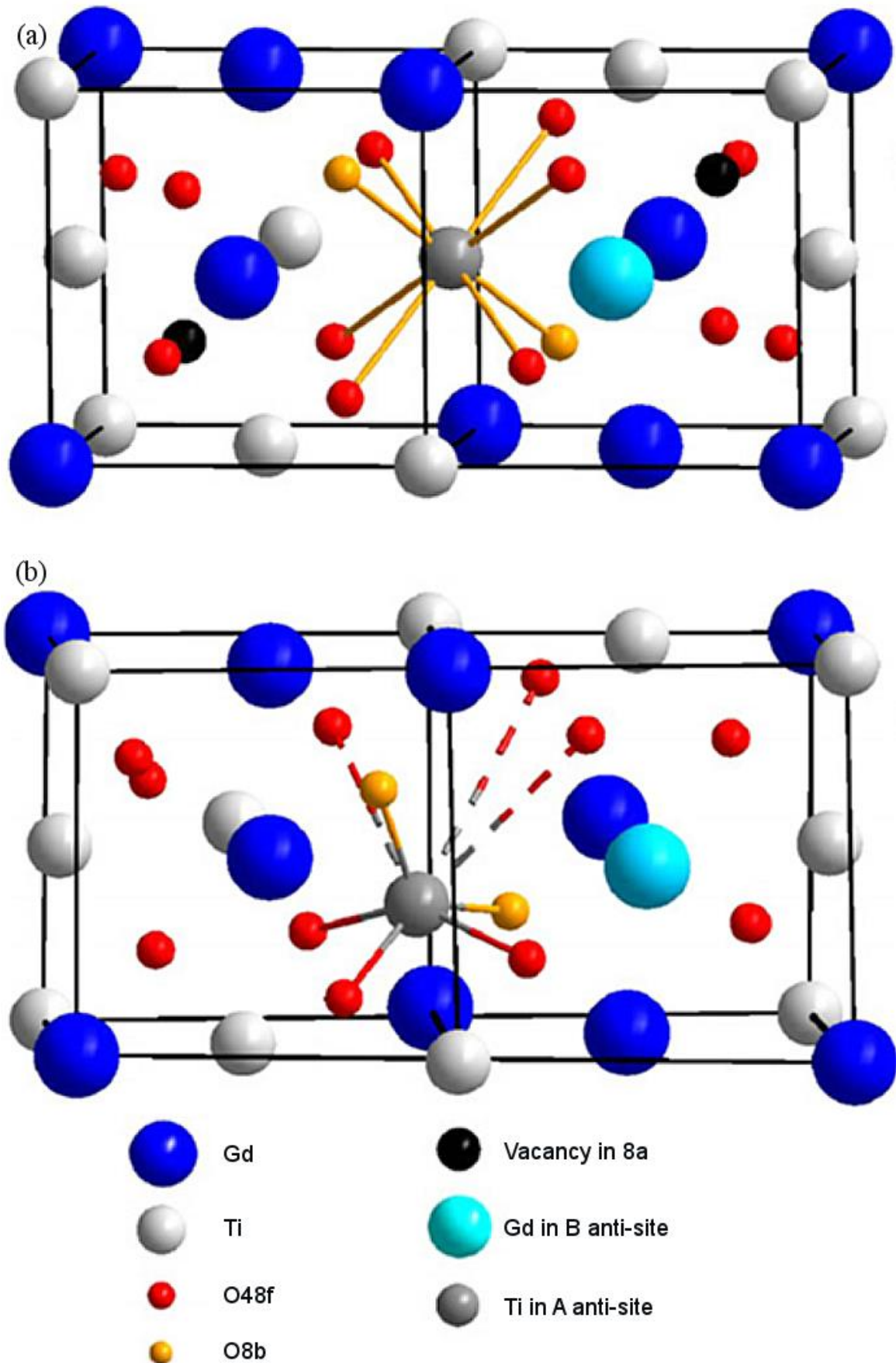
2.3 Self-annealing

Immediate as well as long term annealing affects the life-time of isolated alpha-recoil tracks. Crystalline order should recover as a function of heat, time, defect species and lattice structure. While an XRD and TEM study of 51 natural pyrochlore group minerals concluded mean track lives of 100 Ma (Lumpkin & Ewing 1988) from increasing saturation doses with mineral age, zircon ($ZrSiO_4$) and zirconolite ($CaZrTi_2O_7$, also a derivative of the fluorite structure) recoil tracks were estimated of having even longer mean life times of 400 and 700 Ma, respectively (Sinclair & Ringwood 1981; Ewing *et al.* 1982; Ewing & Headley 1983; Hurley & Fairbairn 1953). These conclusions are based on the assumption of one

2.3 Self-annealing

displacement per atom for complete amorphization, reported in line with a calculated saturation dose of 1.1×10^{16} α-decay events per mg for synthetic pyrochlore and zirconolite.

In contrast to such slow annealing kinetics, Eyal and Fleischer (Y Eyal & Fleischer 1985) observed faster processes in uraninite and thorianite solid solution. They calculated mean annealing times from decay product fractionation, sensitive to enhanced dissolution of daughter isotopes in the damaged volume compared to crystalline structure mother isotopes, and following the observation that long-lived ^{234}U shows slight fractionation while shorter lived ^{228}Th fractionates significantly. Calculated mean annealing time periods were in the order of just 7800 to 25000 years for three different samples. As the authors state themselves, these damage life-times should be considered carefully, at least for the fact that already metamict irradiated samples were observed to anneal back to a metamict state (Lumpkin *et al.* 1988) and the above mentioned annealing phenomena only consider isolated alpha-recoil tracks. More complex defects than just isolated Frenkel vacancy-interstitial-pairs (e.g. dislocations, clusters, hydration) resulted in higher annealing temperature or slower kinetics of uraninite single crystals (Weber 1981). Analysing natural pyrochlores as analogues for actinide embedding material allows us to access structures that have been exposed to alpha radiation for millions of years (Ewing *et al.* 1988). Hence, such materials enable us to study phenomena with regard to long living radioactive isotopes in radioactive waste, when actinides become the elements with the largest activity after several hundred years of deposition (Hedin 1997). Geological samples similar to those used in this study were used in the XRD study of Lumpkin and Ewing (1988).

2.4 Sample description

The mineral pyrochlore was first described by the German chemist Friedrich Wöhler in 1826. The term pyrochlore goes back to greek words pyros (fire) and chloros (green). The name was given due to its greenish glow on blowpipe annealing (Wöhler 1826).

Five pyrochlores with different degrees of radiation damage were chosen in order to characterize and to compare possible differences in their annealing behaviour. Samples are obtained from the Mineralogisches Museum Hamburg (Schelingen, Zlatoust, Miass), the Pacific Museum of the Earth, Vancouver, Canada (Panda Hill), and collected by T. Chudy, University of British Columbia, Canada, (Blue River).

Geologically, all five samples are accessories in carbonatite host rock. All samples exhibit octahedral habit. The metamict samples show a glassy lustre.
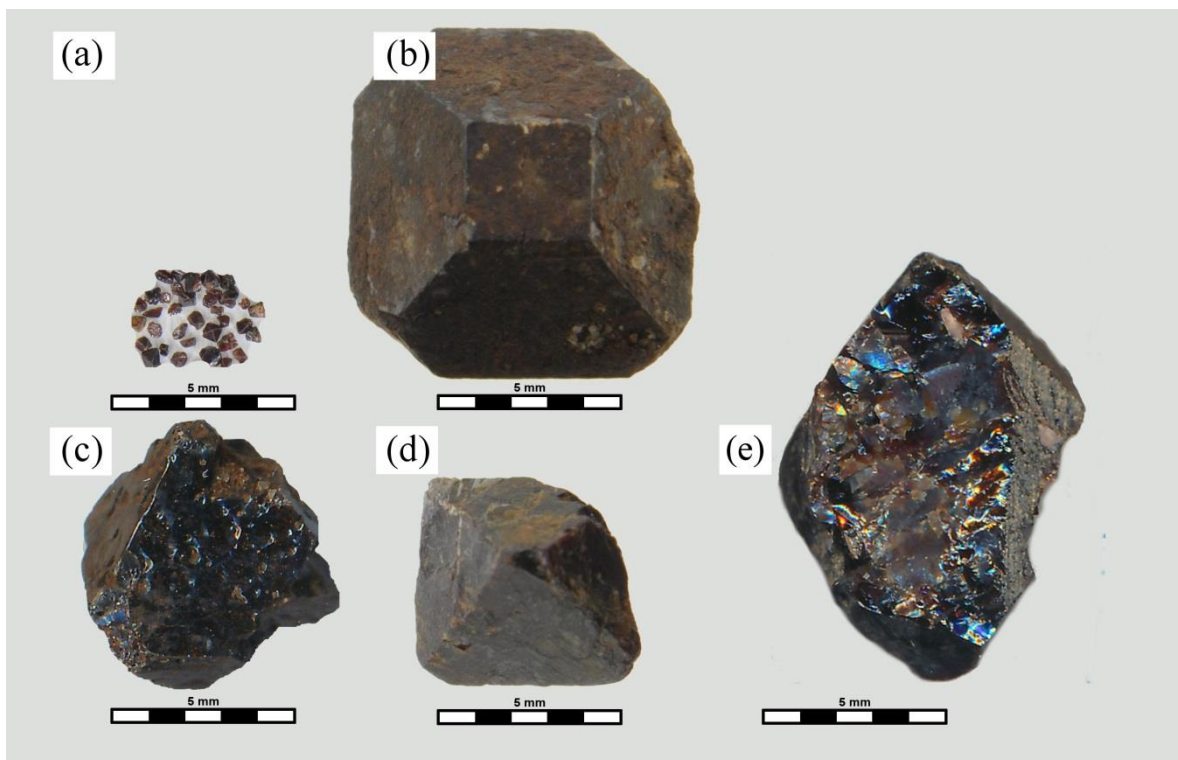

Fig. 9. Pyrochlores from (a) Schelingen, Germany, (b) Panda Hill, Tanzania, (c) Blue River, Canada, (d) Miass, Russia, and (e) Zlatoust, Russia.

Schelingen pyrochlore is from an intrusion at Kaiserstuhl, southwestern Germany. Macroscopic crystal shapes are well preserved and sample size is 1-2 mm diameter.

2.4 Sample description

Kaiserstuhl magmatism occurred 16 Ma ago, dated using K-Ar as 16 Ma (Lippolt 1963). Pyrochlores form small brown to black accessory phenocrysts in the carbonatite matrix.

Panda Hill pyrochlore is from the Mbeya mountain range in southwestern Tanzania. Idiomorphic octahedral of mid-brown colour and diameters of 1-3 cm are frequent. Carbonate intrusions are reported to be 116 Ma old (Bell & Blenkinsop 1987).

Black pyrochlore from the Blue River valley (Upper Fir location) in the Monashee Mountains, Canada, had a partially preserved octahedral shape, but showed iridescent reflexion and conchoidal fracture. Carbonatite intrusions in that area formed some 328 Ma ago (Berger *et al.* 2009).

Dark brownish Zlatoust and Miass pyrochlores from the Ilmen Mountain carbonatites of southern Ural, Russia, are 432 Ma old (Krasnobaev *et al.* 2010). They also show iridescence at conchoidal fractures and at some preserved octahedral faces.

Similar samples have been analysed by Lumpkin and Ewing (Lumpkin & Ewing 1988) in order to learn about structure and radiation tolerance. Among others, Schelingen (similar to "194a", AMNH 35522), Panda Hill (similar to "162b", AMNH 25592), Blue River (similar to "2E37", A. Mariano), Zlatoust and Miass (similar to "088", USNM 155714) were analysed by Lumpkin and Ewing using XRD and HRTEM to determine the critical amorphization dose. The analyses shown in this thesis is related to their findings in structural damage and a previous recrystallization study including one pyrochlore from southern Ural (Lumpkin, Foltyn, *et al.* 1986). The studies now added in this work concerning the recrystallization behaviour complement the authors' findings using optical spectroscopy, calorimetric measurements, diffraction techniques and local probes. The chemical compositions of the samples were thoroughly analysed using an electron microprobe.

2.5 Experimental methods

2.5.1 Electron microprobe

Principle of backscatter electron and wavelength dispersive X-ray analysis

First electron microprobe was built in 1932 by E. Ruska (Knoll & Ruska 1932). The first scanning electron microscope was built by M. v. Ardenne in the mid 1930's (von Ardenne 1938). Finally, the integration of the evaluation of characteristic X-rays using a monochromator crystal was included by Guinier and Castaing in the late 1940 and early 1950 (Castaing & Guinier 1950).

Reed (2005) gives an overview of the usage of an electron microprobe. The following description refers to this book. Electron microprobe probes the interaction of an electron beam with the uppermost ~ 1-2 micrometers of a sample by backscatter electron (BSE) images and wavelength dispersive X-ray (WDX) analysis. Electrons are emitted from the tip of a cathode by applying high voltage. They are accelerated towards an earthed anode. After passing the anode, several electromagnets stable and condense them on the sample surface. The penetration depth of the backscattered electrons and the emitted characteristic X-rays mainly depend on mass and density of the sample atoms.

BSE images show mass contrasts on the sample surface resulting from the scattering of the primary beam electrons and the random walk electrons exiting the sample in almost 180° with respect to the incident beam. Two solid-state half ring detectors arranged concentric around the primary beam register the BSE. The higher the mass density of the probed volume, the brighter is the spot on the image. The electron beam scans a surface area in lines by changing the magnetic field with electromagnetic coils along the primary beam.

Characteristic X-rays of an atom are emitted, if inner electrons of the sample atoms interact elastically with the incident electron beam. The incident electrons can excite inner electrons to higher energy levels. When returning to their original energy level, they emit an element specific radiation. This radiation is dispersed for its wavelength by an analysing crystal in order to exclude radiation of energetically similar excitations. Experimentally, the sample, a monochromator crystal and the detector are arranged on the so called Rowland circle (Fig. 10).

2.5 Experimental methods
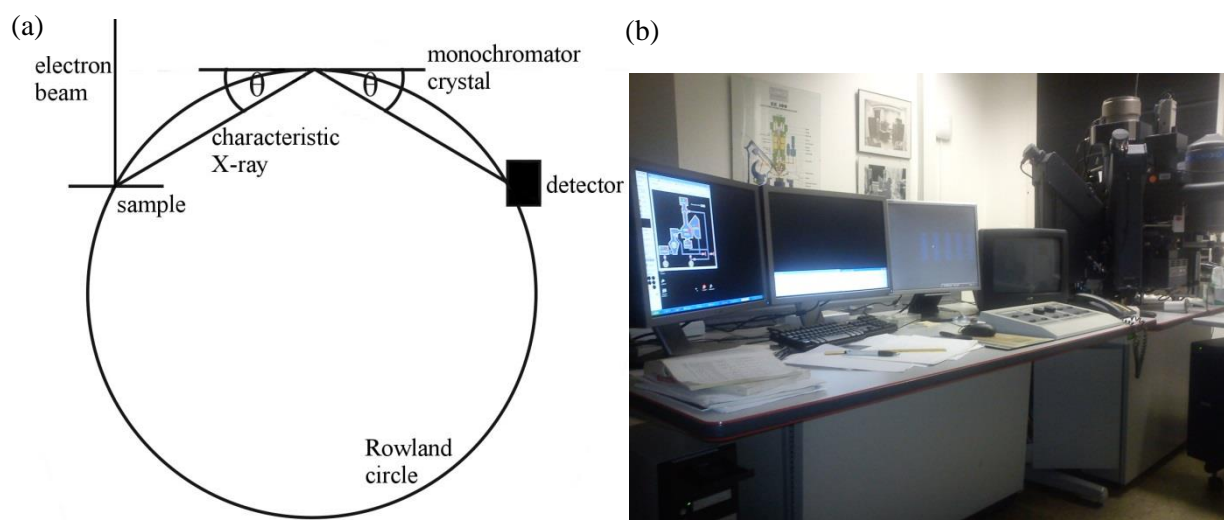
Fig. 10. (a) Rowland circle arrangement to probe WDX on an electron microprobe. (b) Cameca Camebax SX100, Hamburg.

Experimental conditions

Electron microprobe analysis was applied to analyse the composition of the samples and to probe their homogeneity. The samples were cut along (111), polished with colloidal SiO_2 grains (0.1 µm) and coated by carbon sputtering. Samples from Schelingen, Panda Hill, Blue River and Miass were analysed with a CAMECA Camebax microbeam SEM at the Mineralogisch-Petrographisches Institut, Hamburg, and a CAMECA SX100 at the Joint Microprobe Laboratory of the Masaryk University & Czech Geological Survey in Brno, Czech Republic. Acceleration voltage of 15 kV and a beam current of 20 nA were used for both, BSE and WDX analyses in Hamburg and Brno, respectively.

Analyses were averaged over 9 to 64 points. Probed elements were measured relative against reference standards as listed in Table 1. Monochromator crystals PC1, thallium phthalate (TAP, d: 12.88 Å), 'large' pentaerythrite (LPET, d: 4.37 Å), PET and 'large' lithiumfluoride (LLIF, d: 2.01 Å) were used for Brno analyses and LiF, PET, LPET and TAP in Hamburg. Ca, Ti and Nb were measured for 20 s, Na, Si, Fe, Sr, Zr, Ba and La for 30 s and F, Mg, Ce, Nd, Sm, Ta, Pb, Th and U for 60 s in Hamburg. Background accumulation times were half the peak counting times at both sides of the signal. Polished cuts parallel to (111) were prepared for spectroscopic and chemical analyses.

2.5 Experimental methods

Table 1. Microprobe standards, monochromator crystals and

Standard	Radiation	Monochromator crystal	Peak count time (s)	Detection limit (%)
LiF	F K_α	TAP	60	0.14
Albite	Na K_α	TAP	30	0.03
MgO	Mg K_α	TAP	60	0.01
Andradite	Ca K_α,	LPET	20	0.04
Andradite	Fe K_α	LiF	30	0.08
Andradite	Si K_α	TAP	30	0.02
$MnTiO_3$	Ti K_α	PET	20	0.05
$SrTiO_3$	Sr L_α	LPET	60	0.06
$ZrSiO_4$	Zr L_α	PET	60	0.06
Nb_2O_5	Nb L_α	TAP	20	0.12
Ba glass	Ba L_α	LPET	30	0.12
ree3	La L_α	LPET	60	0.07
ree2	Ce L_β	LPET	60	0.14
ree4	Nd L_β	LPET	60	0.12
ree3	Sm L_β	LPET	60	0.14
Ta_2O_5	Ta L_α	LPET	60	0.15
Vanadinit	Pb M_α	PET	60	0.16
Th glass	Th M_α	PET	60	0.14
UO_2	U M_β	PET	60	0.14

The signal intensity is proportional to the square of the magnitude of the X-rays electric field vector. Mass fractions were calculated using the ZAF correction (Z: atomic number, A: absorption, F: fluorescence) of integrated signal intensities. This takes into account the sample mass density ρ and the penetration depth z as main influence values of the activation volume of the emitted characteristic X-rays.

Site occupancies were calculated via molecular weights and with respect to 2 B cations − following the assumption that Nb, Ti, Ta, Zr, Si and W occupy only B sites of $(A_2)(B_2O_6)(O,OH,F)$. The water content was calculated in order to reach charge balance.

2.5 Experimental methods

2.5.2 X-ray powder diffraction

Principle of X-ray diffraction

As Laue predicted theoretically in 1912 (Friedrich, Knipping & Laue 1912) and W.H. and W.L. Bragg confirmed in their experiments in 1913 (Bragg & Bragg 1913), X-rays form distinctive patterns, if a crystal is irradiated and a detector probes the focal plane. Their conclusion was that the crystal must consist of a regular 3D lattice. With this discovery crystal structures became accessible for analysis up to very complex materials as well as proteins or less ordered structures that constitute much of the scientific focus of crystallography today.

X-ray diffraction (XRD) probes the diffraction angle θ of constructively interfering X-rays on their path difference between two or more reciprocal lattice planes of the same family (Fig. 11), e.g. (Meschede 2004). Constructive interference occurs if the Laue conditions of integer products for all three lattice vectors with the diffraction vector. In that case the Bragg equation

$$n\lambda = 2d_{hkl}\sin(\theta_{hkl})$$

is fulfilled. n is an integer number, λ is the wavelength of incident and scattered X-rays in Å, d_{hkl} the distance of equivalent lattice planes {hkl} and θ_{hkl} the corresponding Bragg or diffraction angle.
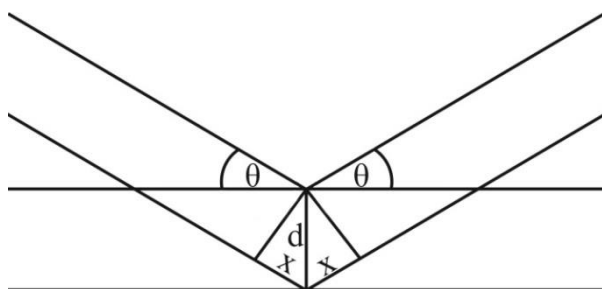
(a)   (b)

Fig. 11. (a) Constructive interference of parallel waves in case of $2x = n\lambda$ (Bragg's law). (b) Stoe Multipurpose Diffractometer, Hamburg.

2.5 Experimental methods

Ground fine powder of a sample ensures that each orientation of a crystal lattice plane is present parallel to the sample surface, and normal to diffraction vector k_i-k_s, respectively, leading to superimposed signals depending on orientation and phase.

The intensity of the scattered beam can either be measured directly on the focussing circle, or, for better resolution in the focal plane of a further monochromator crystal (cutting of K_{α_2} signal). By tilting the sample and the detector, the diffraction angle θ is probed.

Experimental conditions

XRD measurements were performed on a Philips XPert Bragg-Brentano diffractometer. A copper anode with Cu K_α radiation of wavelength $\lambda = 1.54$ Å was used. The 2-theta step width was 0.02°. Measuring range was $15° \leq 2\theta \leq 70°$. Powders were annealed for 1 hour in a Thermo Scientific Heraeus K114 chamber furnace with a temperature resolution of $\pm$ 6 K. The temperature was independently verified by an Ahlborn Therm 2420 thermocouple.

Measurements of high-temperature annealing steps above the recrystallization were performed on a Stoe Multipurpose Diffractometer (Cu $K_{\alpha1}$, 40 kV, 30 nA, Ge (111) monochromator, step width 0.005°). The (111) signal of a Si waver was used for zero-point calibration. 2 measurements after the same annealing step were used to combine the data of both diffractometers.

Diffraction signals were fitted with OriginPro 8.6G software using a least squares regression of pure Lorentzian function for each Bragg signal, and Pseudo-Voigt function for the amorphous background signal, respectively.

2.5.3 Raman spectroscopy

Raman scattering

Inelastic light scattering on molecular vibrations was discussed for the first time theoretically by Smekal (Smekal 1923). A scattering process is called inelastic if the energy of an irradiated system is different from the previous state in response to the interaction. As Raman and Krishnan showed in their experiments with carbon dioxide and several organics, scattered radiation had a different spectrum from the incident light with characteristic additional bands

for molecular groups (Raman 1928). Today, monochromatic laser sources and elaborated monochromator systems are applied for a well resolved spectrum of the weak Raman scattering in order to study structural changes with highest resolution (Bismayer 1988, Bismayer 1990, Nasdala *et al.* 2004).

The propagation of light can be described by its electric field vector E that oscillates in space with the angular frequency ω and with time t

$$E = E_0 \cos(\omega t).$$

An energy quantum of light is called a photon with energy E

$$E = \hbar \omega$$

and momentum p of

$$p = \hbar k$$

$\hbar$ is the reduced Planck constant (1.055×10^{-34} Js) and k is the wave vector.

Atoms in solid-state bodies can move with 3N degrees of freedom. N is the number of involved atoms. For non-linear molecules there are 3 translational, 3 rotational and 3N-6 vibrational degrees of freedom. In a primitive unit cell, there are 3 so called 'acoustic' modes along and 3N-3 in 'optical' modes transverse to the propagation direction. These modes are called phonons. They have a quantum energy E

$$E_n = (n+1/2)\, \hbar \omega$$

with the order n of energy state harmonics and a quasi-momentum p

$$p = \hbar q$$

q is the difference vector of the incident and scattered wavenumber vector.

The electromagnetic field of the incident beam interacts with the atomic, molecular or crystal vibrations. Mainly, the vibrational energy is rereleased elastically as the so called Rayleigh scattering. Additionally, a dipole moment can be induced either because of the polarity of the molecules themselves, or into the electron cloud. While the former will result in the absorption of infrared light, the latter causes inelastic Raman scattering. In the case of Raman scattering, this dipole moment μ depends on the polarizability or Raman tensor α and

2.5 Experimental methods

the electric field vector of the incident beam. The Polarization P (dipole moment per unit volume) is

$$P = \alpha.E$$

Hence, the induced dipole moment depends on the vibrational symmetries of the involved atoms and their orientation with respect to the lights' electric field vector. The deformed electron cloud then can also affect the nuclei vibration, together resulting in the Raman effect.

Developing the polarizability in a Taylor series with respect to a displacement vector q_k,

$$\alpha = \alpha_0 + \Sigma(d\alpha/dq_k)_0 q_k + \dots$$

leads to a polarization of

$$P = \alpha_0 \, E_0 \cos(\omega_0 t) + (d\alpha_0/dq_0) \times \cos[\omega(q)t] \cos(\omega_0 t)$$

$$= \alpha_0 E_0 \cos(\omega_0 t) + \tfrac{1}{2}(d\alpha_0/dq_0) \, E_0 \times \{\cos[\omega_0 + \omega(q)]t + \cos[\omega_0 - \omega(q)]t\}$$

close to the centre of the Brillouin zone $k \approx 0$. The quantum transitions of vibrational modes are called phonons. Vibrational states can be described by group theory via selection rules for symmetrically allowed degenerations of a given atomic group. Because of the quantum nature of allowed vibrational states, the frequency change called Raman shift is also quantized. Phonons apart from those of the Brillouin zone centre generally have much lower impulses so that their contribution to the change in scattered frequency is minor in general. Vibrational modes are only Raman active, if

$$(d\alpha_0/dq_0) \neq 0.$$

The observed energy bands are called Stokes for $(\omega_0 - \omega)$ or Anti-Stokes for $(\omega_0 + \omega)$ depending on whether the energy difference is negative or positive, respectively. For ambient temperature measurements as used in the work, Stokes shifts are used. The q independent term is the Rayleigh scattering. In a quantum energy model, elastic Rayleigh scattering can be described as an excitation from a ground state to a virtual state and back to the initial energy level. In the Stokes case the final energy level is higher than the initial and for anti-Stokes it is

lower. Phonon frequencies ω depend on the bond strength and mass of the atms involved according to

$$\omega \sim \sqrt{\frac{K}{m_{eff}}}$$

where K is the 'spring' constant and m_{eff} is the effective mass.

Experimental conditions

Raman spectra were collected with a Horiba Jobin-Yvon T64000 triple monochromator system, using the 514.5 nm line of Ar^+, surface laser power was ~ 8 mW with a spot diameter of ca. 2 µm (50x magnification objective, 0.5 aperture on an Olympus BX41 microscope). The wavenumber resolution was ~2 cm^{-1}. Acquisition times were 15-60 s depending on the Raman intensity at room temperature. Before annealing and after the last annealing step the samples were checked for photoluminescence with the 488 nm-laser line and for homogeneity at different spots on the polished (0.1 µm colloidal SiO_2) (111) surfaces.

For vibrational mode assignment the parallel polarized measurements were compared to the cross-polarized incident and outgoing beam. As moderately damaged the Panda Hill and Blue River samples showed varying 810 cm^{-1} intensities before annealing, areas with a low 605 to 810 cm^{-1} intensity ratio were chosen for analysis. Annealing was conducted ex-situ using a Linkam stage TS1200EV-10/5 with annealing times of 1h and a heating/cooling ramp of 15 min for each annealing step. Raman measurements were performed at room temperature. The measurements were calibrated using the 520.5 cm^{-1} peak of a silicon waver. Analyses were operated with LabSpec 5 software.

All samples were also measured in the higher wavenumber range up to 3800 cm^{-1} before annealing in order to detect OH groups or water. Spectra of Panda Hill pyrochlore were additionally collected in (100) to investigate the influence of orientation effects. For vibrational mode assignment the parallel polarized measurements were compared to cross polarized incident and outgoing beam. Annealing was conducted with a Linkam stage TS1200EV-10/5 and annealing times of 1h. Heating and cooling ramps were 15 min each. Annealing temperatures were the same as for the powder X-ray diffraction studies: 295, 400, 500, 600, 700, 800, 900, 1000, 1200, and 1400 K.

2.5 Experimental methods

The data was processed with OriginPro 8.6G software. After background subtraction the spectra were corrected for a constant baseline. As no wavenumber range below 1000 cm^{-1} shows a base intensity, a simple constant was subtracted in order to not distort the spectra arbitrarily. All spectra were reduced according to Bose-Einstein statistics of temperature dependent energetic states. Background and baseline corrected intensities were divided by the Bose-Einstein factor

$$n(\omega) + 1 = \frac{1}{e^{\frac{\hbar\omega}{k_B T}} - 1} + 1$$

for first order Stokes signals. ħ is the reduced Planck constant (1.055 x 10^{-34} Js), ω the angular frequency, k_B the Boltzmann constant (1.38 x 10^{-23} J/K) and T the absolute temperature. After dividing by the exposition time and laser power all spectra are normalized to intensity 1 and smoothed by a 3 point averaging. A spectral range of 15 to 1000 cm^{-1} were used for the analyses.

The spectral bands were fitted with Lorentzian functions

$$L(x) = y_0 + \frac{2A\omega}{\pi 4(x - x_c)^2 + \omega^2}$$

(y_0: offset, x_c: center of Lorentzian function, ω: width, A: intensity scaling factor) in order to have a clear signal identification. Fittings with pseudo-Voigt functions were also performed, but they yielded larger uncertainties in the spectral parameters without changing the trends with the annealing temperature. Using a Pseudo-Voigt function (linear combination of Gaussian and Lorentzian functions) would give better fitting results, especially in case of the expected radiation derived disorder. However, the advantage of using Lorentzians is that the signal is not additionally biased by broadening effects that would result in stronger overlapping and larger fitting errors.

2.5.4 Fourier Transform Infrared spectroscopy

The vibration of a polar atomic group (i.e. the group has a charge centre apart from its mass centre) directly absorbs incident radiation in an inelastic scattering process (Günzler 2003). This is due to photon-phonon interactions resulting in a change of the dipole moment of the

involved atomic group. The time resolved detector signal is Fourier-transformed into frequency space.

Experimental conditions

To verify whether in general the compositional disorder violates the phonon selection rules, infrared spectra from the crystalline reference sample were collected with a Bruker Equinox Fourier Transform Infrared spectrometer. 1 mg of sample powder was mixed with 200 mg of KBr reference and pressed into a pellet. The applied pressure on the powders was 10 t cm^{-2}. Spectra were collected in 128 scans for a range of 400 to 4000 cm^{-1} in transmission mode. The light absorption is measured by an interferometer. The Bruker Opus/2 software was used to operate the analyses. OriginPro 8.6G was used to process the data.

2.5.5 Differential scanning calometry / Thermogravimetry

Differential scanning calometry / thermogravimetry (DSC/TG) probes weight and differential energy change upon heating of a sample. Energy change is probed by simultaneous heat flux measurement of the sample and a reference material. Exothermal reactions (like ordering processes) are visible as a positive, endothermal reactions (like increasing disorder) as a negative differential heat flux dH/dT (Hemminga & Cammenga 1989).

Experimental conditions

Simultaneous DSC-TG analyses were performed using a Netzsch STA 449 C instrument. The samples were annealed in a Pt pan in air from room temperature up to 1000 K with a heating rate of 10 K per min.

2.6 Group theoretical analysis of the pyrochlore structure

According to the SAM software of the Bilbao Crystallographic Server at www.cryst.ehu.es (Kroumova *et al.* 2003) for space group 227 and Wyckoff positions 8b, 16c, 16d and 48f of the ideal pyrochlore structure, there are 26 fundamental phonon modes symmetry allowed. As the electric field of electromagnetic radiation is perpendicular to its propagation, light probes the so called optical vibrational modes transverse to the propagation direction. Acoustic

2.6 Group theoretical analysis of the pyrochlore structure

modes along the propagation direction cannot be seen in Raman or infrared analysis. Of the 26 first-order modes, 6 are Raman- and 7 are infrared-active optical modes (listed in Table 2).

Table 2. Vibrational modes of the pyrochlore structure ($Fd\overline{3}m$).

Wyckoff position	Mode (R: Raman-active, IR: IR-active, ina: inactive)*
A(16d)	A_{2u}(ina)+E_u(ina)+T_{2u}(ina)+$2T_{1u}$(IR)
B(16c)	A_{2u}(ina)+E_u(ina)+T_{2u}(ina)+$2T_{1u}$(IR)
X(48f)	A_{1g}(R)+A_{2u}(ina)+E_u(ina)+E_g(R)+$2T_{2u}$(ina)+$3T_{2g}$(R)+$3T_{1u}$(IR)+$2T_{1g}$(ina)
Y(8b)	T_{2g}(R) +T_{1u}(IR)

* One T_{1u} mode is acoustic, most probably that one related to the lowest-energy cation vibration.

2.7 Results

2.7.1 Microscopy and macroscopic sample change

Upon annealing in air all samples strongly bleached to a light brown colour. Light microscopy was used to control whether the probed volume remains comparable in the order of the laser spot size (~2 μm), as the samples were removed from its position before each annealing step. Visible microscopic irregularities were used to realign the sample in all experiments sensitive to lateral movements. Partially, surface features changed with annealing temperature, but they remained recognizable (Fig. 12 and Fig. 13). In Panda Hill fissures formed below an annealing temperature of 500 K (Fig. 12).
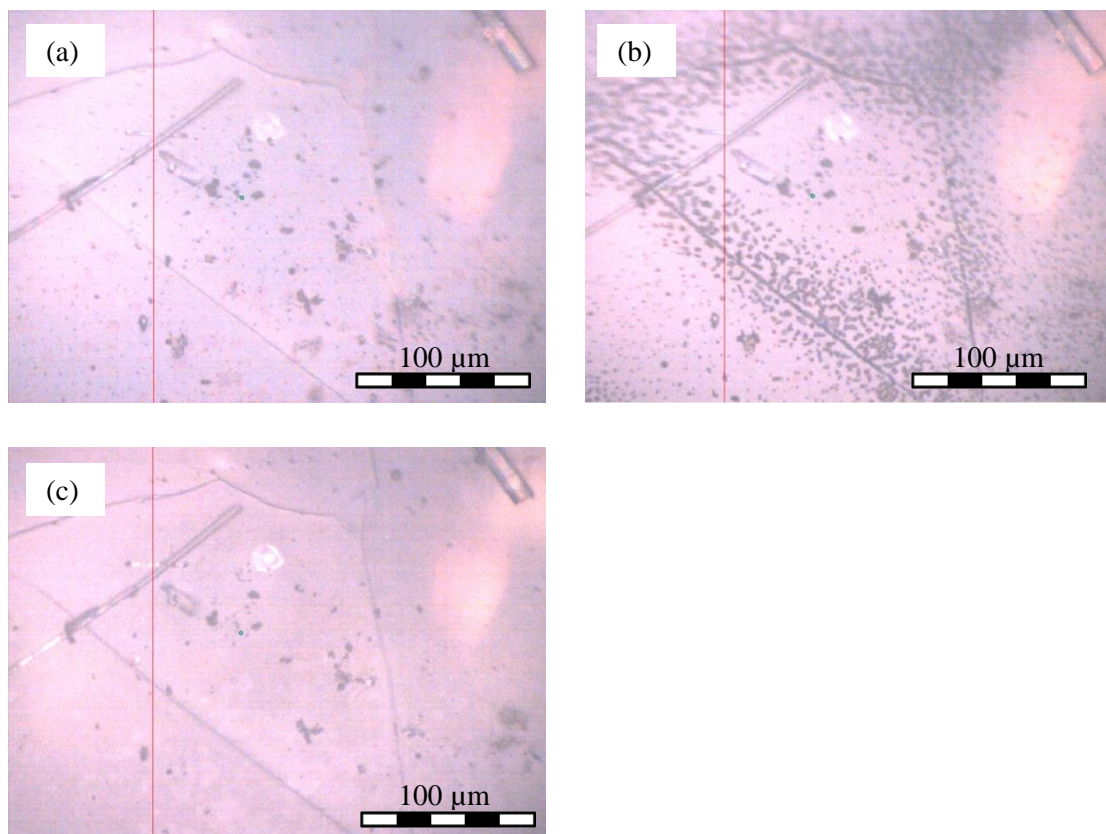

Fig. 12. Microscopic pictures at the Miass pyrochlore surface after annealing steps 900 K (a), 1000 K (b) and 1200K (c).

In Panda Hill and Blue River sample, some surface reaction occurred along these fissures after an annealing step of 1000 K each (see Fig. 12b, Fig. 13b) which disappeared after annealing at higher temperature.
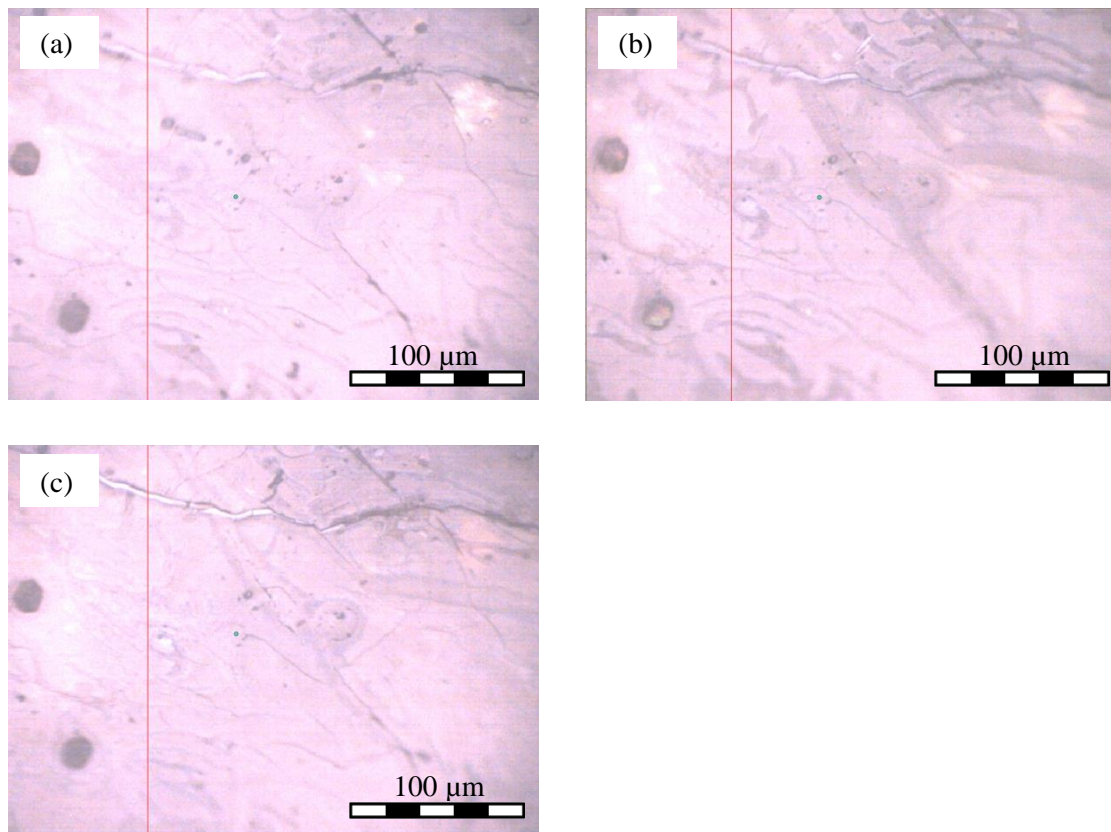
[29]

Fig. 13. Microscopic pictures of Blue River pyrochlore surface after annealing steps 800 K (a), 1000 K (b) and 1200K (c).

2.7.2 Electron microprobe

Backscatter electron images

Due to its structural variability and built-in vacancies of pyrochlore, the element species can vary to a larger extent. This is a favourable material property for the embedding of different radioactive isotopes and their decay products. A good chemical classification is essential for relating structural changes not only to structural features, but also to the influence of a partially deviating chemistry.

Electron microprobe BSE images show a rather uniform major element distribution in all samples (Fig. 14). Panda Hill pyrochlore shows some zoning visible especially in the thorium content with almost doubled Th concentrations in the narrow zones of a few micrometres layer thickness. These zone areas were not included in the averaged microprobe results of the Panda Hill sample.
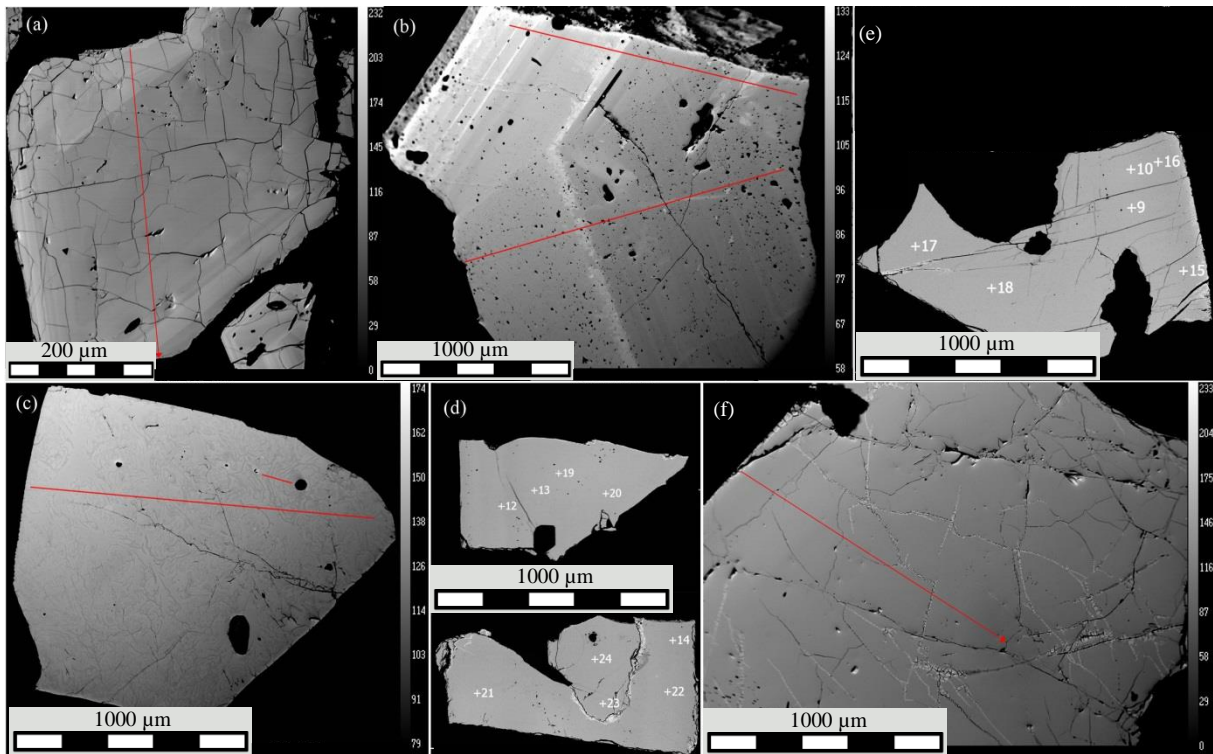
2.7 Results

Fig. 14. Back-scattered electron images of pyrochlores Schelingen (a), Panda Hill (b), Blue River (c), Miass (d) and Zlatoust (e, f). Points at white plus and along red lines were probed.

Wavelength dispersive X-ray analysis

WDX analyses are reported as average weight percent of 25 spots along a 443 µm line on Schelingen (Fig. 14a), 44 points along two lines of 1572 µm and 1783 µm length on Panda Hill (Fig. 14b), 64 points along two lines of 146 and 1577 µm length on Blue River (Fig. 14c), 31 points along a 1249 µm line and random points, respectively, on Zlatoust (Fig. 14 e,f), and 9 random points on Miass pyrochlore (Fig. 14d). Standard deviations show variations from the average. Zoned regions (in Schelingen and Panda Hill) were excluded from the analyses.

Major oxides are Nb_2O_5, in average ranging from 46.5±0.8 wt% in Blue River to 61.5±1.2 wt% in Panda Hill pyrochlore, and CaO ranging from 10.4±0.3 wt% in Blue River to 18.6±0.4 wt% in Schelingen pyrochlore (Table 3).

From chemical classification according to Arroyo *et al.* (2010) all five pyrochlore samples can be described as fluorcalciopyrochlores according to their principal Y-, A- and B-site atoms, respectively. Fluorine content ranges from 1.8±0.3 wt% in Schelingen to 4.2±0.1 wt% in Miass pyrochlore. High totals suggest a rather small amount of $(OH)^-$ groups which cannot be measured by electron microprobe.

[31]

2.7 Results

Less abundant major oxides comprise TiO_2 with 1.1 ± 0.2 wt% (Schelingen) to 10.0 ± 0.3 wt% (Miass), Na_2O 2.3 ± 0.2 wt% (Schelingen) to 5.8 ± 0.2 wt% (Miass) and Ce_2O_3 <0.1 (Blue River) to 5.8 ± 0.5 wt% (Schelingen). Si, Zr, Mg, Fe, Sr, La, Nd occur as minor elements in all samples. Minor amounts of W, Mn, Y, Pr and Dy were also present in Zlatoust and Miass samples.

The main compositional difference of the probed samples is the high Ta_2O_5 and UO_2 content in Blue River pyrochlore of 18.3 ± 0.4 wt% and 11.9 ± 0.4 wt%, respectively. In contrast, UO_2 is only built-in as trace element in the magnitude of the quantitative microprobe detection limit (0.1 wt%), and Ta_2O_5 in amounts of <0.1 wt% (Schelingen) to 2.0 ± 0.4 wt% (Miass).

Thorium is the major radiogenic element in Panda Hill, Zlatoust and Miass samples with ThO_2 concentrations of 1.8 ± 0.4 wt% to 7.2 ± 0.6 wt%. In Schelingen and Blue River pyrochlore, however, Th is below the detection limit.

2.7 Results

Table 3. Chemical composition of pyrochlore samples in wt% oxides. Total oxide equivalent corrected for overestimated oxygen $(m_O/m_F)/2$.

	Schelingen	σ	Panda Hill	σ	Blue River	σ	Zlatoust	σ	Miass	σ
	($n = 25$)		($n = 44$)		($n = 64$)		(n = 31)		($n = 9$)	
TiO_2	1.1	0.2	5.1	0.3	2.9	0.1	9.9	0.3	10.0	0.3
ZrO_2	2.0	0.4	1.0	0.4	<det.lim.		<det.lim.		<det.lim.	
Nb_2O_5	60.1	1.3	61.5	1.2	46.5	0.8	51.5	0.9	50.6	0.5
Ta_2O_5	<det.lim.		0.7	0.3	18.3	0.4	2.1	0.3	2.0	0.4
Na_2O	2.3	0.2	5.3	0.7	4.5	1.2	5.6	0.3	5.8	0.2
MgO	0.5	0.1	<det.lim.		<det.lim.		<det.lim.		<det.lim.	
CaO	18.6	0.4	17.5	1.7	10.4	0.3	15.1	0.3	14.5	0.3
					-		0.3	0.1	0.3	0.1
FeO	1.3	0.1	0.2	0.1	0.2	0.4	0.3	0.1	0.2	0.1
SrO	0.2	0.1	0.5	1.0	0.6	0.4	<det.lim.		-	
Y_2O_3					-		0.2	0.1	0.3	0.1
La_2O_3	0.9	0.1	<det.lim.		<det.lim.		1.1	0.1	1.2	0.1
Ce_2O_3	5.8	0.5	0.9	0.1	<det.lim.		2.9	0.1	3.2	0.2
Pr_2O_3					-		0.3	0.1	0.3	0.1
Nd_2O_3	0.8	0.1	0.2	0.1	<det.lim.		0.7	0.1	1.0	0.1
ThO_2	<det.lim.		1.8	0.4	<det.lim.		6.9	0.5	7.2	0.6
UO_2	<det.lim.		<det.lim.		11.9	0.4	0.2	0.3	<det.lim.	
F^-	1.8	0.2	3.9	0.5	2.3	0.3	4.1	0.3	4.2	0.1
Sum	95.9	1.5	98.9	1.6	97.9	1.1	101.3	1.1	101.8	0.6
-O of F	-0.8		-1.6		-1.0		-1.7		-1.8	
Total	95.1		97.3		96.9		99.5		100.0	

* '<det.lim.': below quantitative detection limit, '-': not observed

2.7 Results

Atoms per formula unit

	Schelingen	σ	Panda Hill	σ	Blue River	σ	Zlatoust	σ	Miass	σ
X, Y anions										
O	6.92	0.11	6.47	0.04	6.33	0.06	6.54	0.06	6.60	0.03
F	0.38	0.07	0.77	0.04	0.52	0.06	0.83	0.05	0.86	0.02
B cations										
Ti	0.05	0.01	0.24	0.01	0.15	0.01	0.48	0.02	0.48	0.02
Zr	0.07	0.02	0.03	0.01	< det.lim.		< det.lim.		< det.lim.	
Nb	1.86	0.03	1.72	0.02	1.48	0.02	1.48	0.03	1.48	0.01
Ta	< det.lim.		< det.lim.		0.35	0.01	0.04	0.01	0.04	0.01
A cations										
Na	0.29	0.04	0.64	0.03	0.61	0.16	0.69	0.03	0.72	0.02
Mg	0.06	0.01	< det.lim.		< det.lim.		< det.lim.		< det.lim.	
Ca	1.37	0.04	1.17	0.04	0.79	0.02	1.03	0.02	1.00	0.02
Mn	-		-		-		< det.lim.		0.02	0.01
Fe	0.08	0.02	0.01	0.01	< det.lim.		0.02	0.01	0.01	0.01
Sr	0.01	0.01	0.02	0.01	0.02	0.01	< det.lim.		-	
Y	-		-		-		0.01	0.01	0.01	0.01
Ba	< det.lim.		< det.lim.		< det.lim.		0.01	0.01	-	
La	0.03	0.01	< det.lim.		< det.lim.		0.03	0.01	0.03	0.01
Ce	0.17	0.04	0.02	0.01	< det.lim.		0.07	0.01	0.08	0.01
Pr	-		-		-		0.01	0.01	0.01	0.01
Nd	0.03	0.01	< det.lim.		< det.lim.		0.02	0.01	0.02	0.01
Th	< det.lim.		0.03	0.01	< det.lim.		0.10	0.01	0.11	0.01
U	< det.lim.		< det.lim.		0.19	0.01	< det.lim.		< det.lim.	

* "<det.lim.": below detection limit, "-": not observed

In terms of Wyckoff sites, structural A sites are occupied mainly by Ca and Na. Together, they make up 69.9 weight percent in Blue River, 82.7% in Schelingen, 85.9% in Zlatoust, 86.3% in Miass and 90.4% in Panda Hill pyrochlore (calculated from atoms per formula unit, Table 3, second part). While Ca is more abundant in all pyrochlores, the Ca/Na site ratio is closest to 1:1 in Blue River, Miass and Zlatoust pyrochlore, rather 2:1 in Panda Hill, and almost 5:1 in Schelingen pyrochlore. The remaining fractions to 2 cations, which would be the full occupation, are primarily occupied by rare earth elements (esp. Schelingen), actinides (the highly radiation damaged and metamict samples) or stay vacant.

B sites are occupied by niobium in fractions of 73.8% (Miass) up to 93.1% (Schelingen). The remainder is titanium (2.5% in Schelingen, 7.6% in Blue River, 11.7% in Panda Hill, 23.8% in Zlatoust and 24.1% in Miass pyrochlore), zirconium (<0.1% in Blue River, 0.2% in Zlatoust and Miass, 1.5% in Panda Hill and 3.7% in Schelingen pyrochlore)

and tantalum (<0.1% in Schelingen, 0.5% in Panda Hill, 1.7% in Zlatoust and Miass, and 17.5% in Blue River pyrochlore). For simplification, X sites are assumed to be completely occupied by oxygen. In reality there may also be minor OH^- groups or even H_2O on the 48f sites. Fluorine is positioned on more than half of each Y sites in all the metamict pyrochlores. Only the Schelingen reference pyrochlore builds-in just 38.4% of F. This position is assumed to be shared by O^{2-}, but OH^-, H_2O and vacancies are also reported and may be present here. Hydrogen cannot be detected by electron microprobe measurements as its characteristic radiation has a too large wavelength, i.e. too low energies for detectors.

Calculated hydrogen is assumed to occur only in molecular OH^- for simplification. The absence of clear OH^- or H_2O signals in vibrational spectroscopy also suggests only minor contents of hydrous species. Element total weight percentages leave 4.3 % (Schelingen) up to zero (Miass) for hydrous species. For the Miass sample, this contradicts the weight loss of almost 3% at 1000 K seen in thermogravimetry if weight loss is purely associated with gradual leakage of hydrous species.

2.7.3 Powder X-ray diffraction

X-ray diffraction patterns

Powder X-ray diffraction patterns show minor amorphous background intensities for the Schelingen reference pyrochlore, but two major pronounced humps in the other metamict samples. The amorphous background intensity at higher 2θ angles is fitted best with two Gaussian peaks. Additionally, weakly damaged Panda Hill and strongly radiation-damaged Blue River and Zlatoust pyrochlores show narrow Bragg diffraction signals, which indicate the presence of small crystalline clusters in the natural, untreated samples. The untreated Miass sample showed no Bragg signals whatsoever (Fig. 15).
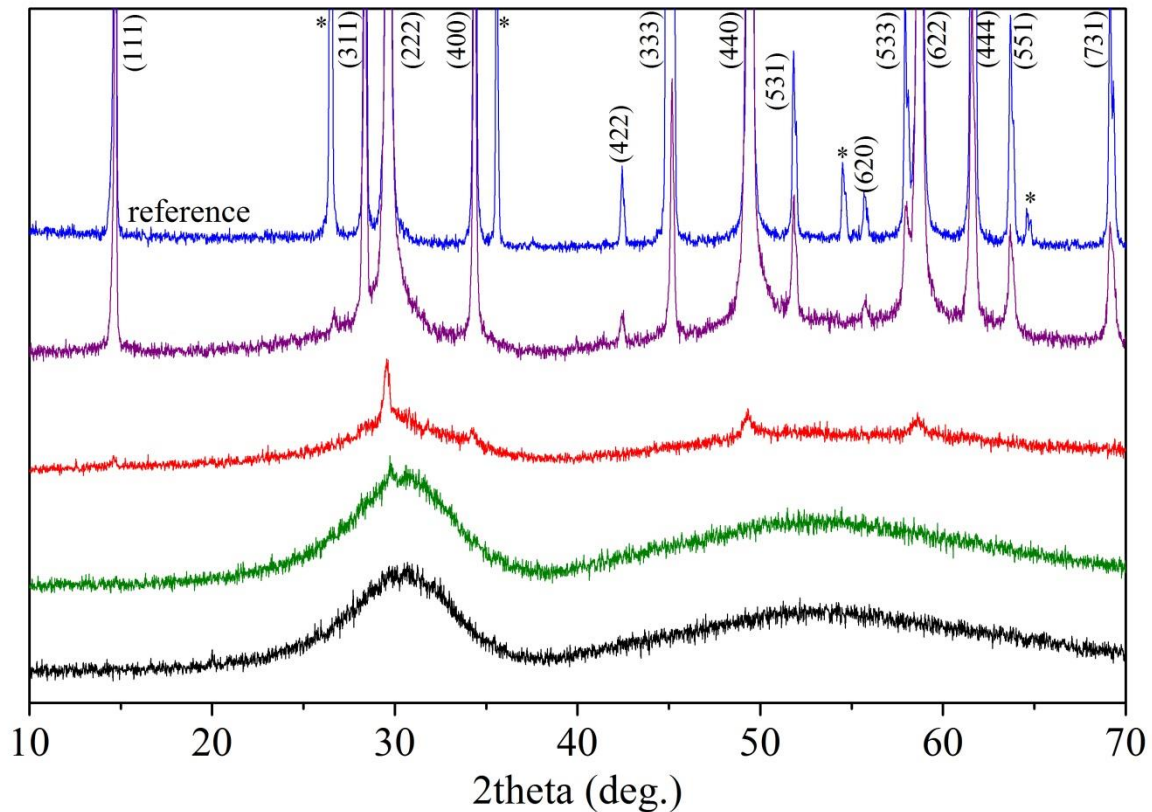
2.7 Results

Fig. 15. Diffractograms of untreated pyrochlores Miass (black), Zlatoust (green), Blue River (red), Panda Hill (violet) and Schelingen (blue).

The intensity of Panda Hill and Blue River Bragg signals increase on heating between 500 and 700 K and remain constant above 730 K. The Miass pyrochlore is fully "XRD amorphous" up to 790 K. Bragg signals increase considerably above the 830 K annealing temperature. In all samples a small amorphous fraction of the diffraction signal remains visible up to 1000 K annealing temperature.

In Schelingen and Panda Hill pyrochlore only two minor Bragg signals ($2\theta=26.6°$ and $44.5°$) can result from carbon impurities. Very weak signals in Schelingen diffraction pattern (at $2\theta=35.6, 54.5, 64.7$ and $67.2°$) are also not caused by the pyrochlore structure. They are marked '*' in the diffragtograms (Fig. 15, Fig. 17, Fig. 18).

Additional phases at 1400 K could be identified as lueshite $NaNbO_3$, fersmite/columbite $CaNb_2O_6$ and possibly Nb-bearing rutile $(Ti,Nb)O_2$ using the Crystallographica SearchMatch software, version 3.1. Some pyrochlore fraction kept intact in all samples even after 1400 K annealing for 60 minutes.

2.7 Results

The Blue River sample with crystalline clusters showed no minor impurities in XRD and the XRD pattern after annealing at 1000 K was used for a Rietveld refinement with the GSAS code (Larson & Von Dreele 2004). The main fitting difficulty was to adapt the tip intensities of the diffraction signals at low and high 2-theta angles (

Fig. 16). A minor texture would improve the fit but was not applied here. The best fit was achieved with a resulting weighted R-value of 0.2028 and a reduced χ^2 of 1.509. The only free structure parameter (x-position of 48f anions) of 0.4368 (Table 4) means that the B-site coordination is almost perfectly octahedral (x=0.4375) and A-site 'cubes' are strongly distorted into trigonal scalenohedra. The fitted lattice parameter of 10.394 Å is very close to the LCLS-Fit of 10.402 Å.
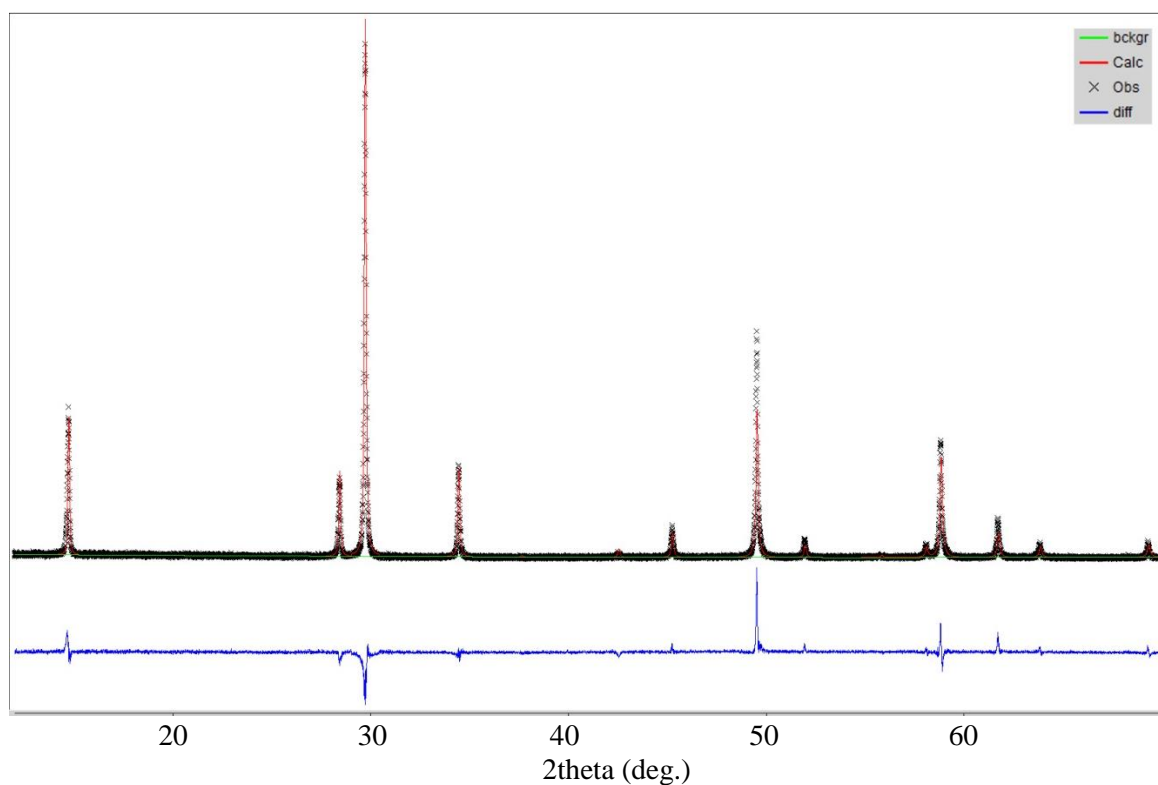
Fig. 16. GSAS Rietveld-Fit of Blue River pyrochlore powder XRD pattern after sample annealing at 1000 K.

EMPA data was used as starting site occupancy (Table 4). Hydrous species are not included in the fit, but will most likely vanish upon annealing.

2.7 Results

Table 4. Rietveld-Fit of powder XRD data with GSAS.

At. name	multiplicity	site symmetry	site occupancy	X	Y	Z
Ca1	16	-3M(111)	0.4854	0	0	0
Na1	16	-3M(111)	0.3918	0	0	0
Sr1	16	-3M(111)	0.0117	0	0	0
U1	16	-3M(111)	0.1111	0	0	0
Ti1	16	-3M(111)	0.0761	0.5	0.5	0.5
Nb1	16	-3M(111)	0.7477	0.5	0.5	0.5
Ta1	16	-3M(111)	0.1721	0.5	0.5	0.5
O1	48	MM2d100	1	0.4368	0.125	0.125
O2	8	-43M	0.4971	0.125	0.125	0.125
F1	8	-43M	0.4123	0.125	0.125	0.125

X-ray patterns show three broad amorphous background diffraction features centred at 28.9, 50.0 and 58.4° 2θ (Panda Hill), 30.3, 51.5 and 61.4° 2θ (Blue River), 30.4, 50.9, 60.8 (Zlatoust) and 30.3, 50.9 and 59.4° 2θ (Miass). Schelingen pyrochlore showed a very shallow amorphous background. Amorphous background intensities decrease with increasing annealing temperature, but never fully disappeared in any pyrochlore. Schelingen reference pyrochlore shows almost no shift of Bragg signals with rising annealing temperature (Fig. 17).
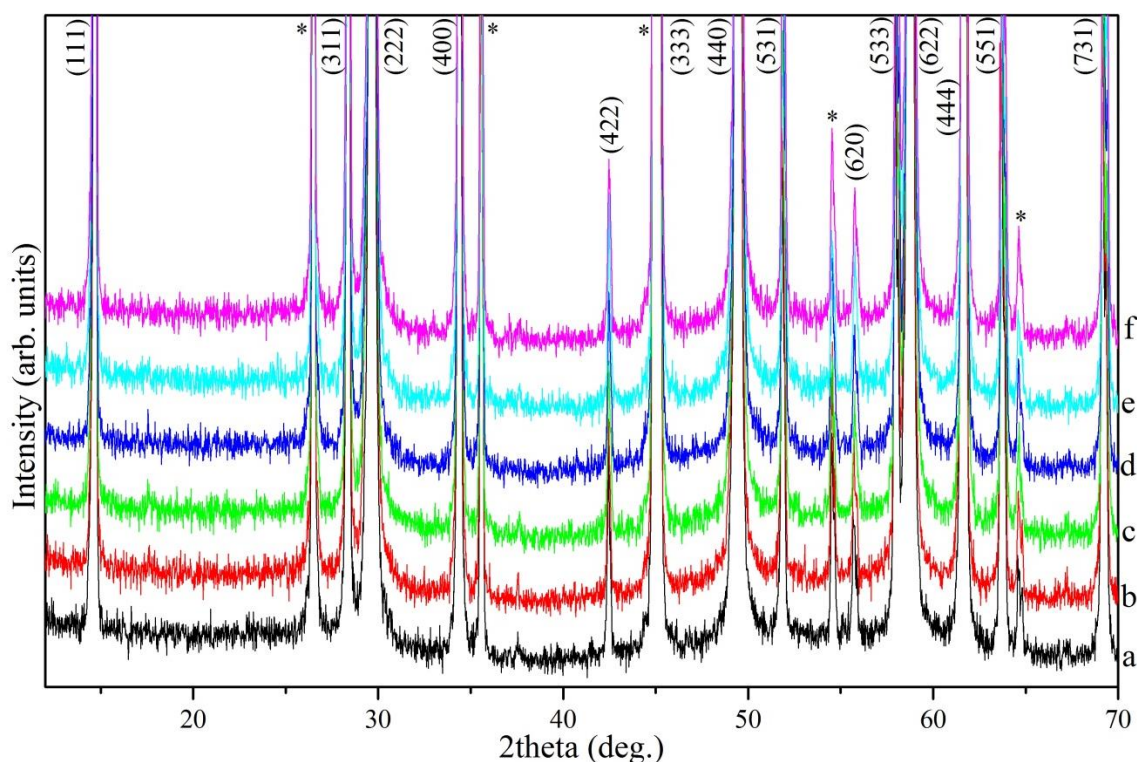
Fig. 17. Powder XRD patterns of Schelingen pyrochlore at room temperature (a) and annealed at 500 K (b), 700 K (c), 750 K (d), 770 K (e), 780 K (f).

2.7 Results

Bragg signals of Panda Hill sample show the largest changes in 2θ angles at annealing temperatures between 500 and 700 K (Fig. 18). Most signals also include a minor shift towards lower 2θ angles between 900 and 1000 K annealing. 500-700 K shifts are in the order of 0.05° 2θ.
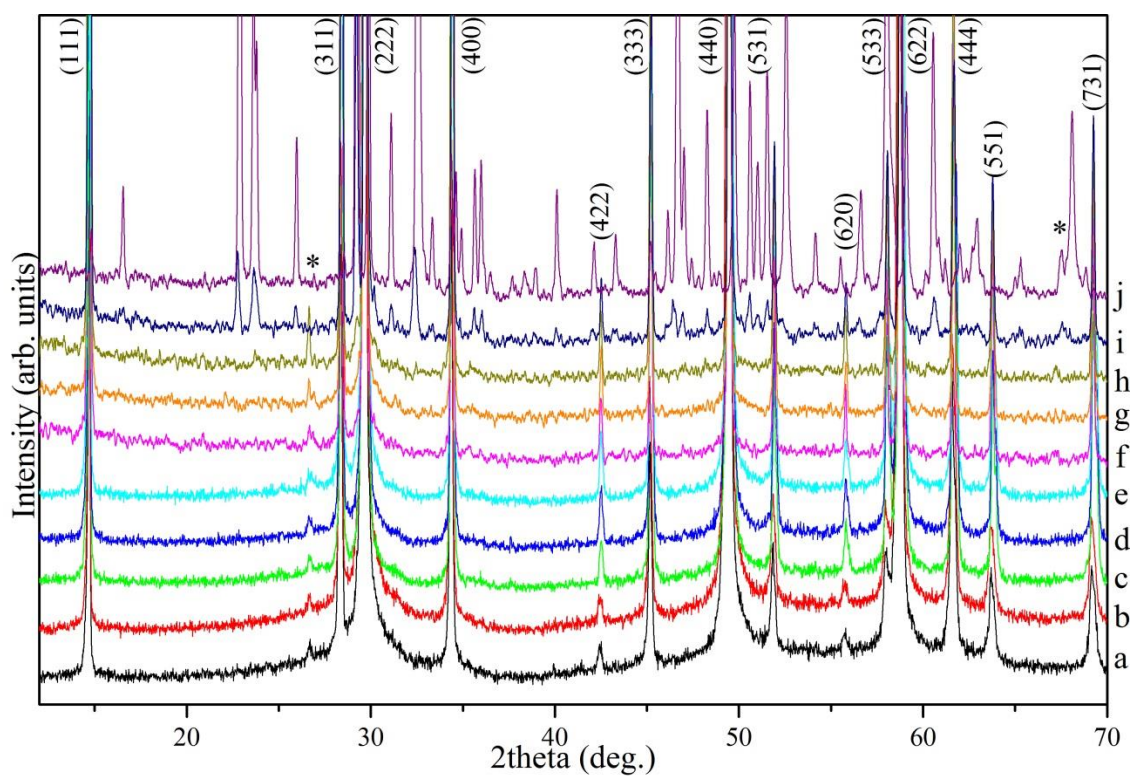

Fig. 18. Powder XRD patterns of Panda Hill pyrochlore at room temperature (a) and annealed at 500 K (b), 700 K (c), 710 K (d), 720 K (e), 800 K (f), 900 K (g), 1000 K (h), 1200 K (i), 1400 K (j).

2.7 Results

Blue River Bragg signal positions shifts in the order of 0.25° to higher 2θ values between ambient temperature and 1000 K (Fig. 19). Most signals show a linear trend with a plateau of almost unchanged positions between annealing temperatures of 550 and 800 K. Diffractograms at 550, 600 and 650 K were measured using a second batch of powder. The diffractograms of untreated batches matched very well and chemical variation in microprobe analysis was also minor.
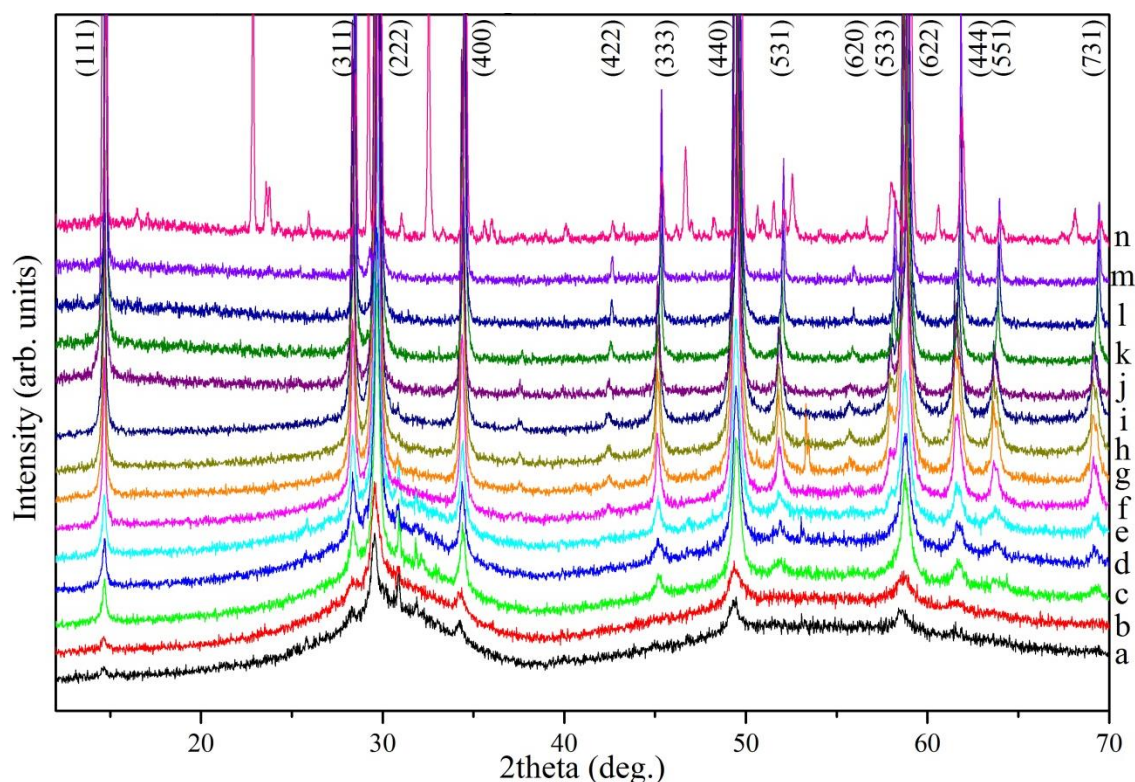

Fig. 19. Powder XRD patterns of Blue River pyrochlore at room temperature (a) and annealed at 500 K (b), 550 K (c), 600 K (d), 650 K (e), 700 K (f), 710 K (g), 720 K (h), 730 K (i), 800 K (j), 900 K (k), 1000 K (l), 1200 K (m), 1400 K (n).

2.7 Results

Zlatoust pyrochlore has a very small crystalline fraction in the untreated state, visible as tiny spike at the position of the (222) signal ($2\theta = 29.7°$) above the amorphous diffraction background (Fig. 20). The (222) Bragg signal increases starting at 750 K. The amorphous background strongly reduces up to 900 K. Decomposition to lueshite and columbite starts after annealing at 820 K, but up to 1200 K pyrochlore remains the main phase. After annealing at the 1400 K, the pyrochlore fraction is strongly reduced.
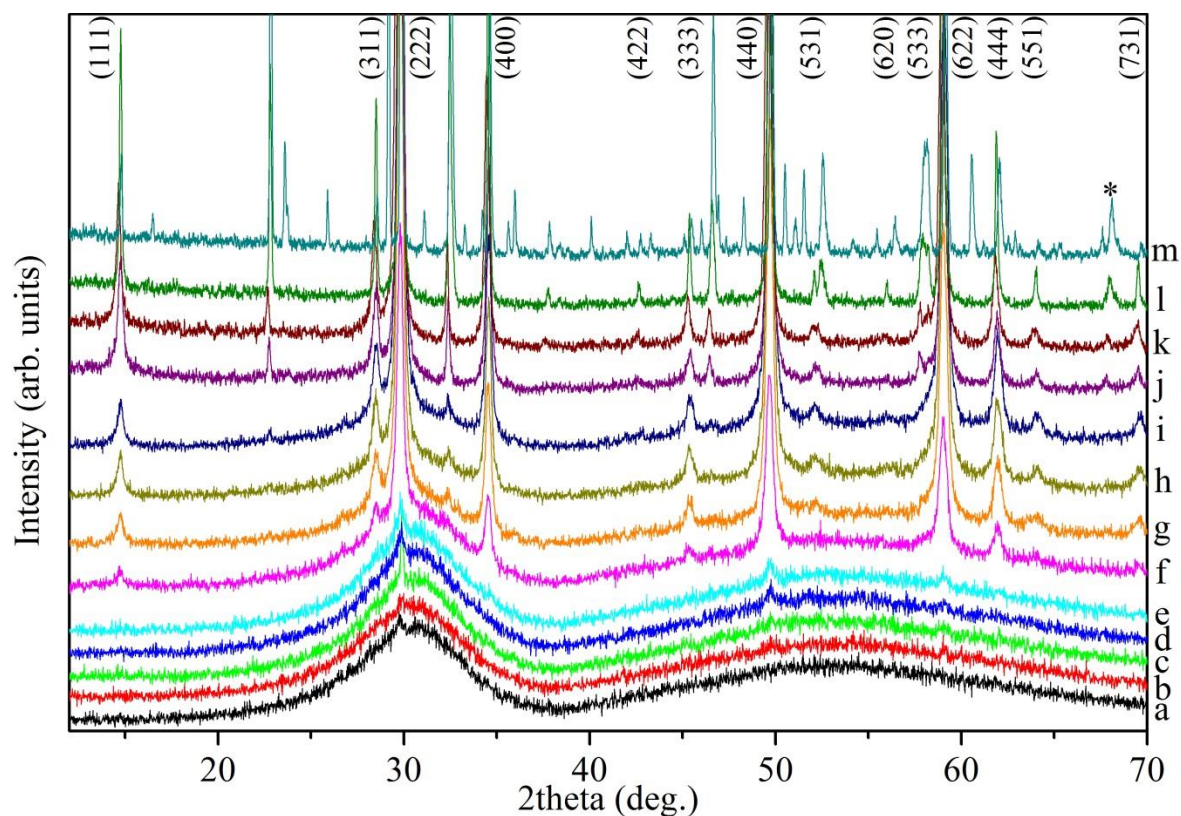
Fig. 20. Powder XRD patterns of Zlatoust pyrochlore at room temperature (a) and annealed at 500 K (b), 750 K (c), 770 K (d), 780 K (e), 790 K (f), 800 K (g), 810 K (h), 820 K (i), 900 K (j), 1000 K (k), 1200 K (l), 1400 K (m).

2.7 Results

Miass sample shows no Bragg signals up to annealing temperature of 790 K where a small fraction crystallized (Fig. 21). Very well crystallinity is reached at 830 K. At that temperature, decomposition (to lueshite (Na,Ca,Th)(Nb,Ti)O_3) also started.
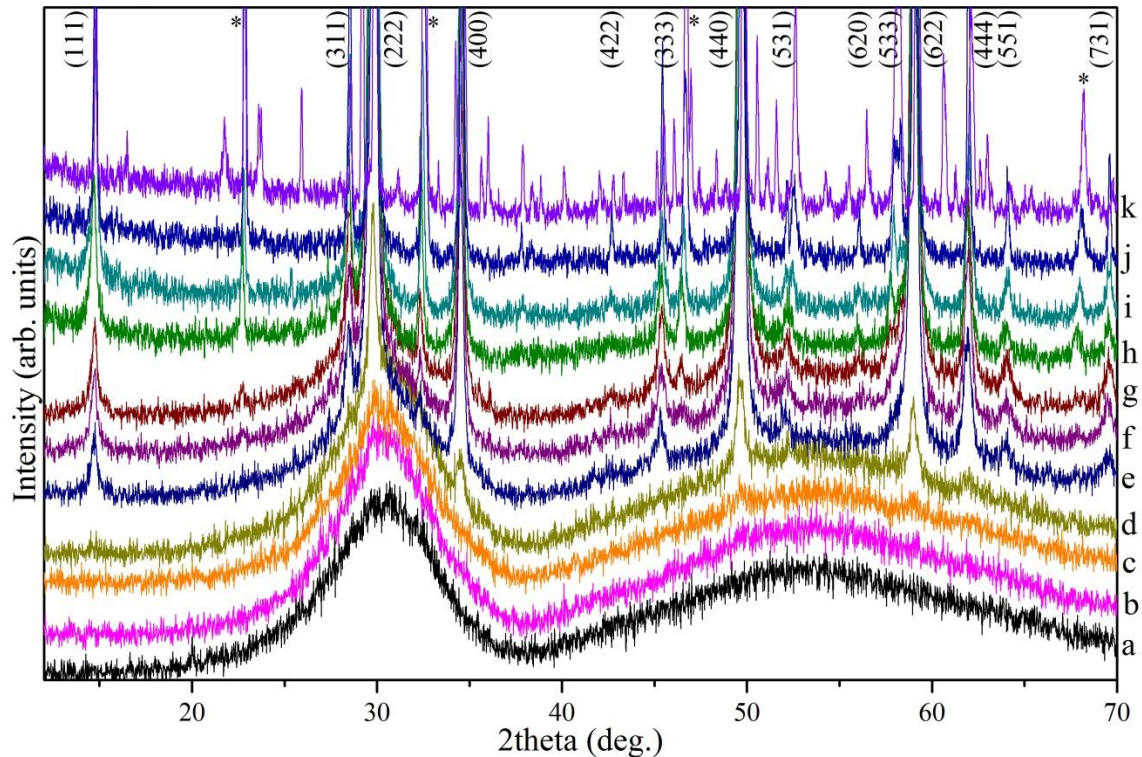

Fig. 21. Powder XRD patterns of Miass pyrochlore at room temperature (a) and annealed at 780 K (b), 790 K (c), 800 K (d), 810 K (e), 820 K (f), 830 K (g), 900 K (h), 1000 K (i), 1200 K (j), 1400 K (k).

Volume change

Using the LCLS code by Prewitt (1974), revised by Copley (1975) and Bismayer (1988) to calculate an idealised unit cell from multiple Bragg signals clearly above the background noise, the unit cell volume decreases with increasing annealing temperature for Panda Hill, Blue River and Miass pyrochlores (Fig. 22). Schelingen pyrochlore shows a no volume change. The Panda Hill pyrochlore reduces its lattice parameter from 10.42 Å to 10.40 Å after annealing at 900 K, but its volume does not decrease further at 1000 K annealing temperature (lattice vector of 10.41 Å). Blue River pyrochlore showed the strongest decrease in unit cell volume (10.46 Å at ambient temperature down to 10.40 Å annealed at 1000 K). Miass lattice parameter decreased from 10.40 Å to 10.37 Å.
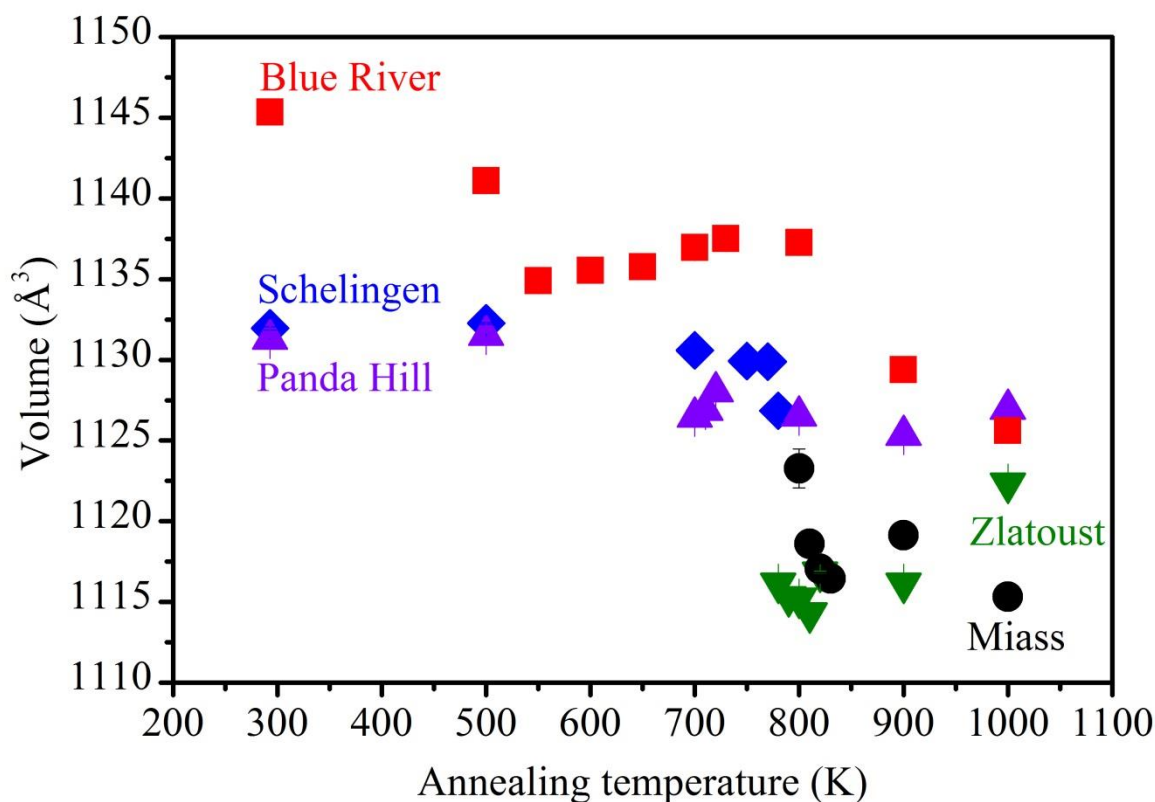
Fig. 22. Unit cell volume calculated using the LCLS software from main mean Bragg signals of pyrochlores Schelingen (◆), Panda Hill (▲), Blue River (■), Zlatoust (▼) and Miass (●). Metamict pyrochlores Zlatoust and Miass show no Bragg signal below 780 and 800 K, respectively.

Full width at half maximum

Schelingen pyrochlore shows no significant changes in the full width at half maximum (FWHM) of its Bragg signal with rising annealing temperature. Hence, it served as a reference for structural ordering in the whole temperature range used for annealing the samples.

The (222) Bragg signal of Panda Hill sample has a linear decreasing trend in its Lorentzian width up to 1000 K annealing temperature (Fig. 31). Its FWHM decreases from 0.14 to 0.09° 2θ. The next largest diffraction signals (622 and 440) also show a clear decrease in width between 500 and 700 K annealing temperature. Both show minor broadening above 800 K. FWHM of Blue River pyrochlore containing small Bragg signals decreases in two steps. Diffraction signals of Zlatoust pyrochlore containing only a very small fraction of crystalline material, narrow in the temperature range of 790 to 820 K. Miass pyrochlore Bragg signals start order at annealing temperature of 800 K sharpen from an initial 0.37° to 0.28° 2θ.

2.7.4 Raman spectroscopy

Raman spectra of the analysed pyrochlores probed in (111) orientation parallel to the sample surface showed at least 13 distinguishable broad bands in the ordered state. Band centres are located at 65, 105, 140, 180, 275, 365, 430, 495, 540, 605, 680, 810 and 860 cm^{-1}. Samples containing high amount of actinides show less and even broader bands, Zlatoust and Miass samples show strong photoluminescence at lower Raman shifts up to 500 cm^{-1} and again above 1000 cm^{-1}.

The samples were tested for homogeneity. The only sample with some impurities was Panda Hill pyrochlore with inclusions of several micrometer diameter - visible in the microscope as darker areas. Raman spectra for these dark inclusions showed an apatite fingerprint (a sharp peak at 967 cm^{-1}) overlapping the pyrochlore signal. Apatite was not seen in XRD patterns or EMP. As they were clearly visible in the sample used for Raman spectroscopy, these inclusions could easily been excluded in measurements.

Panda Hill and Blue River samples showed some variations in the 800 cm^{-1} signal on the untreated sample at different spots, but all spots showed either higher 600 cm^{-1} intensity (Panda Hill) or higher 800 cm^{-1} intensity (Blue River). Schelingen, Zlatoust and Miass showed homogeneous surface. Schelingen pyrochlore was the only untreated sample with a high wavenumber possibly related to a hydrous species around 3608 cm^{-1}. All other samples only showed background intensity were water signals would be expected.
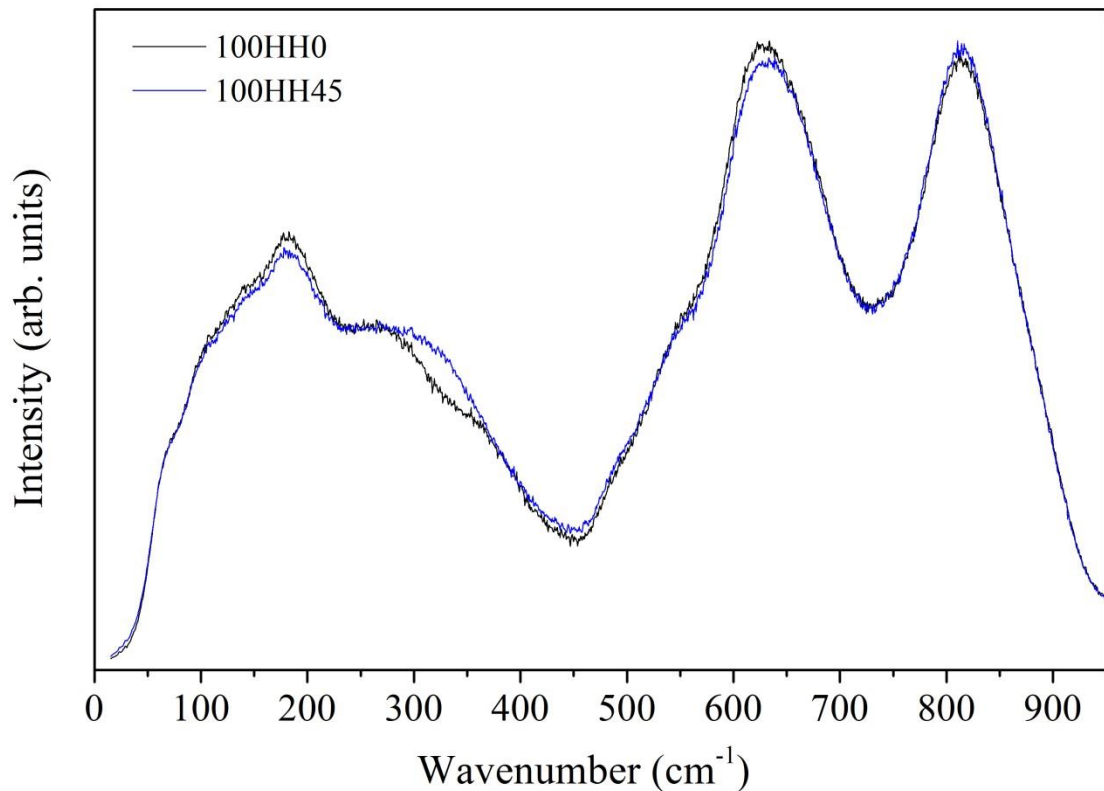
2.7 Results

Fig. 23. Panda Hill pyrochlore in (100) plane, rotated by 45°.

Upon rotation the Panda Hill pyrochlore showed no major deviation in intensity (Fig. 23). The most striking difference occurred in the 300-350 cm^{-1} range. Strong photoluminescence bands occurred at 950-1250 cm^{-1} and 1250-1600 cm^{-1} in all untreated pyrochlores. These bands were reduced significantly upon recrystallization and became pronounced at annealing temperatures above 1000 K. The radiation-damaged pyrochlores also showed photoluminescence at Raman shifts below 600 cm^{-1}. By comparing parallel and cross polarized Raman spectra, intensity differences indicate the occurrence of A modes or E modes. Lower intensity in cross polarized spectra indicate E modes, lower parallel spectra indicate A mode species. Low temperature spectra at 100 and 200 K, respectively, showed no significant deviation with respect to spectra measured at room temperature. The most obvious change is the decrease of 810 and 860 cm^{-1} bands with respect to 605 and 680 cm^{-1} upon rising annealing temperatures. Reordering temperatures differ strongly depending on the initial crystalline volume. All bands strongly overlap resulting in uncertainties in the fitting procedure. Therefore fitted parameters depend to some degree on the initial values. A minimum band number and as few restrictions for the band centre and width as possible were

[45]

2.7 Results

used in the fitting process. Positions and widths were fixed first - starting with the highest annealing temperature, because bands could be positioned with the least uncertainties there. In order to avoid overlapping, as few as possible smaller signals were fitted resulting in an overall worse fit but with lower fitting error. A deviating number of fitted peaks also influences the integrated intensities of neighbouring bands used for the analyses of this study. Schelingen reference pyrochlore shows 5 main bands centred at 180, 275, 540, 605 and 810 cm^{-1}. Smaller bands centred at 65, 105, 140, 365, 430, 495, 680 and 860 cm^{-1} are also present. Panda Hill pyrochlore shows the same pattern as the reference sample (Fig. 24). In its untreated state it differs in a pronounced 810 cm^{-1} band and broader bands in general. Bands centres on 605 and 680 cm^{-1} slightly shift to lower wavenumbers. Minimum Raman shifts of 604 and 649 cm^{-1}, respectively, are reached at 800 K annealing temperature. Band sharpening is visible in the 605 and 680 cm^{-1} FWHM (Fig. 24) up to 800 K where both bands reach an almost unchanged width of 78 and 92 cm^{-1} up to 1400 K. Towards higher annealing temperature, 605 cm^{-1} bands keep their width of 75 cm^{-1} up to 1400 K annealing temperature. While 810 cm^{-1} bands show a linear shift towards higher wavenumbers with rising annealing temperature, their widths scatter around 89 cm^{-1} up to 700 K and around 58 cm^{-1} between 800 and 1400 K.
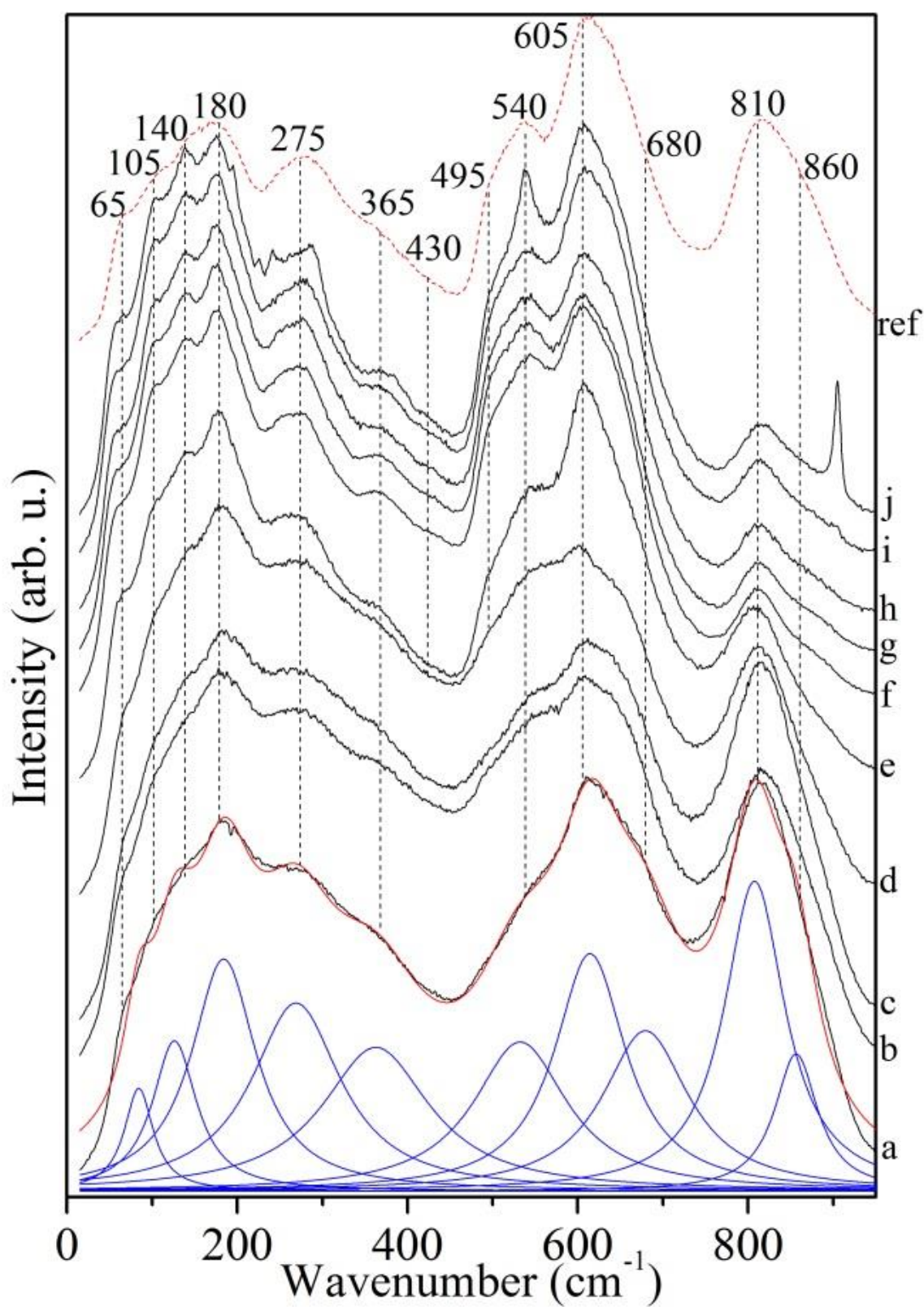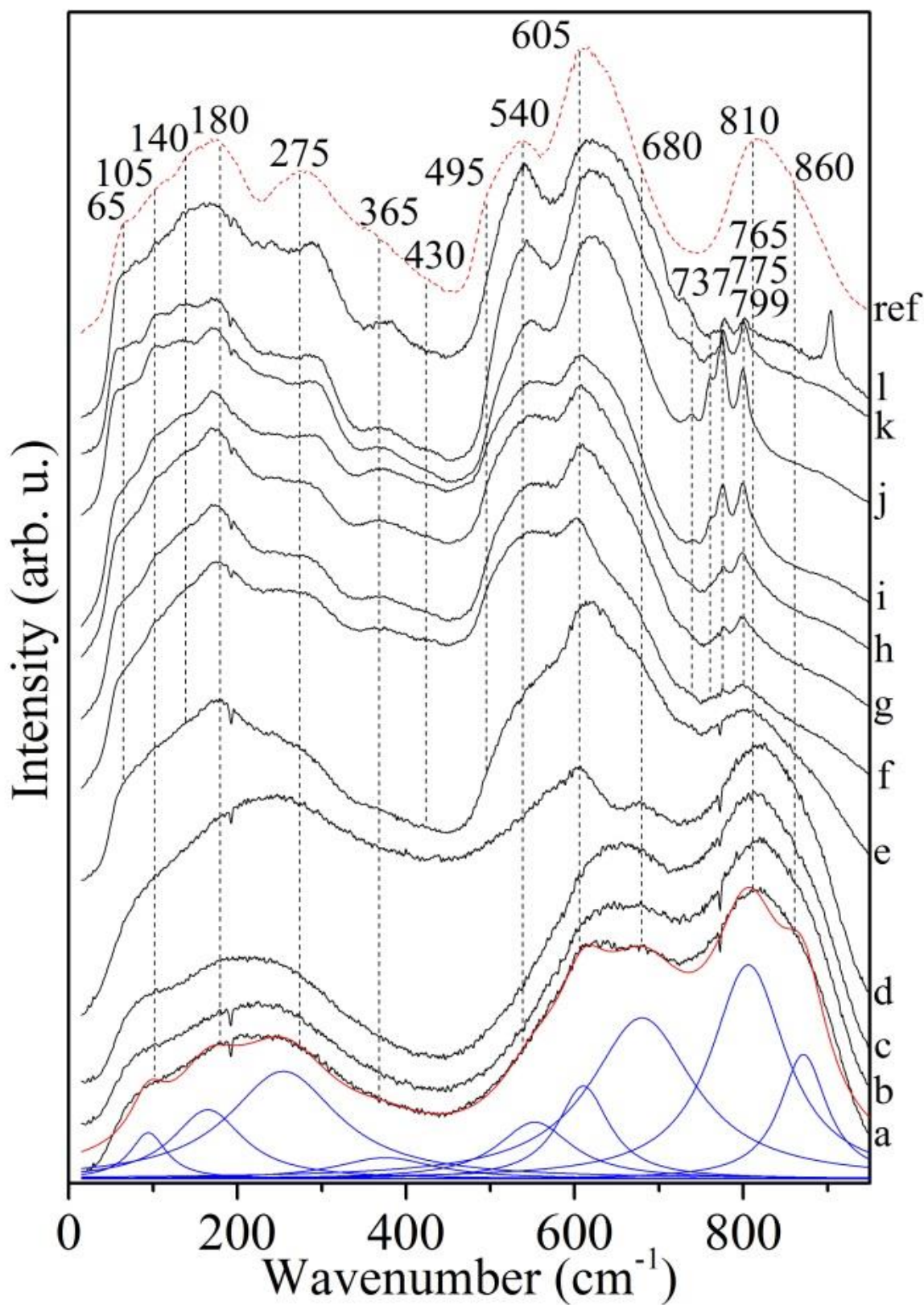
2.7 Results

Fig. 24. Raman spectra of Panda Hill pyrochlore before annealing (a) and after annealing steps of 400 K (b), 500 K (c), 600 K (d), 700 K (e), 800 K (f), 900 K (g), 1000 K (h), 1200 K (i), 1400 K (j), and of untreated Schelingen pyrochlore (ref).

2.7 Results

Blue River pyrochlore shows broader Raman bands than Panda Hill in the untreated sample (Fig. 25a). 605, 680 and 810 cm^{-1} bands are the strongest clearly separable bands in the virgin sample. Lower wavenumbers up to 500 cm^{-1} only show broad bands with no distinct single maximum. At 530 K annealing the 605 cm^{-1} band becomes more pronounced, whereas at 590 K its Raman spectrum almost resembles the Schelingen reference sample. Also starting with an annealing temperature of 590 K, four sharp single bands occur, centred at 737, 765, 775, and 799 cm^{-1} (Fig. 25b). 605 cm^{-1} Raman bands show no clear shift. Widths of the 605 cm^{-1} band show no uniform trend. Widths of 680 cm^{-1} bands decrease from 148 cm^{-1} at 450 K annealing temperature to 104 cm^{-1} at 650 K. At higher temperatures they scatter around this width. 805 cm^{-1} bands scatter around 807 cm^{-1} up to 590 K annealing temperature. At higher annealing temperature these bands are overlapped by the four sharp bands.
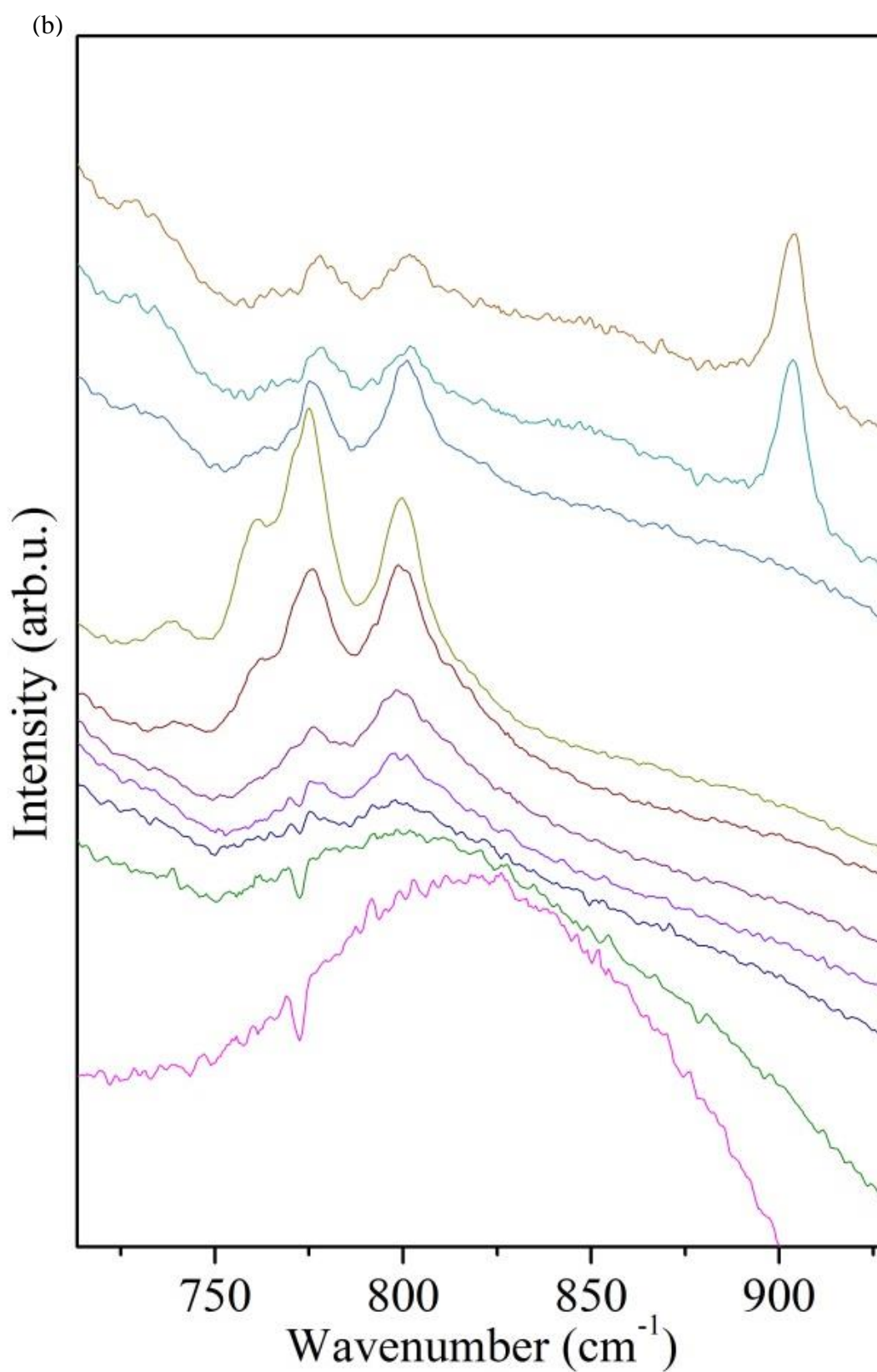
2.7 Results

(a)

2.7 Results

Fig. 25. (a) Raman spectra of Blue River pyrochlore before annealing (a) and after annealing steps of 400 K (b), 500 K (c), 530 K (d), 560 K (e), 590 K (f), 620 K (g), 650 K (h), 800 K (i), 1000 K (j), 1200 K (k), 1400 K (l), and of untreated Schelingen pyrochlore (ref). (b) Enlarged section of modes around 800 cm^{-1}. RT and 1400 K (uppermost spectrum) spectra checked with 488-nm-laser to exclude photoluminescence.

[50]

2.7 Results

The spectrum of untreated Zlatoust pyrochlore (Fig. 26) only has two broad maxima centred at 605 and 835 cm^{-1}. At wavenumbers below 500 and above 1000 cm^{-1} occurs strong photoluminescence. But also between 500 and 1000 cm^{-1} there is some base intensity, affecting the band fitting. Therefore the results should be considered carefully. Zlatoust spectra show no strong changes in the Raman shift and band width upon annealing up to 800 K. At an annealing temperature of 810 K the sample fragmented repeatedly. An unoriented fragment resembled the Schelingen reference sample with a pronounced 606 cm^{-1} band and disappeared photoluminescence (Fig. 26i).
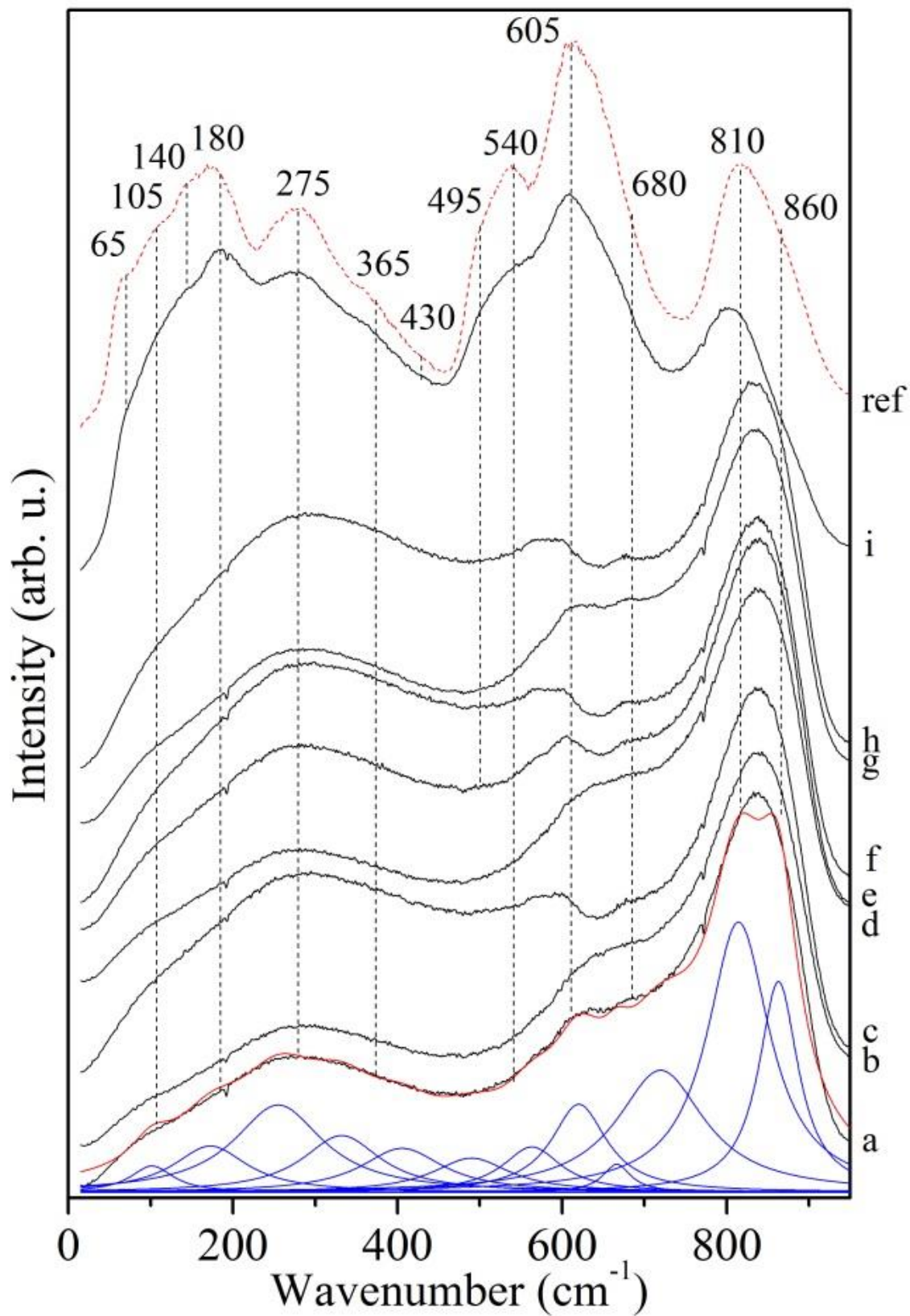
2.7 Results

Fig. 26. Raman spectra of Zlatoust pyrochlore before annealing (a) and after annealing steps of 400 K (b), 500 K (c), 600 K (d), 700 K (e), 780 K (f), 790 K (g), 800 K (h), 810 K (i), and of untreated Schelingen pyrochlore (ref).

2.7 Results

In the amorphous Miass sample, the Raman signal at 810 cm^{-1} is the only one exceeding the photoluminescence and broadened overlapping bands (Fig. 27). Photoluminescence disappears when recrystallization sets in at temperatures above 800 K. On recrystallization the 605 cm^{-1} mode becomes the strongest signal while the mode near 810 cm^{-1} sharply shrinks. Bands of Miass Raman spectra can be followed up to annealing temperatures of 820 K in a continued pattern: a protruding 810 cm^{-1} band and minor maxima centred at 606 and 680 cm^{-1}. Between 600 and 790 K a linear shifts towards higher wavenumbers from 682 to 704 cm^{-1} can be observed. Miass spectra are biased by photoluminescence, especially below 500 and above 1000 cm^{-1}, so that single mode fittings should be considered very carefully. 824 cm^{-1} bands shift linearly up to 832 cm^{-1} between 730 and 820 K annealing. At higher annealing temperatures a maximum level is reached. Photoluminescence disappears during structural ordering at an annealing temperature of 850 K.
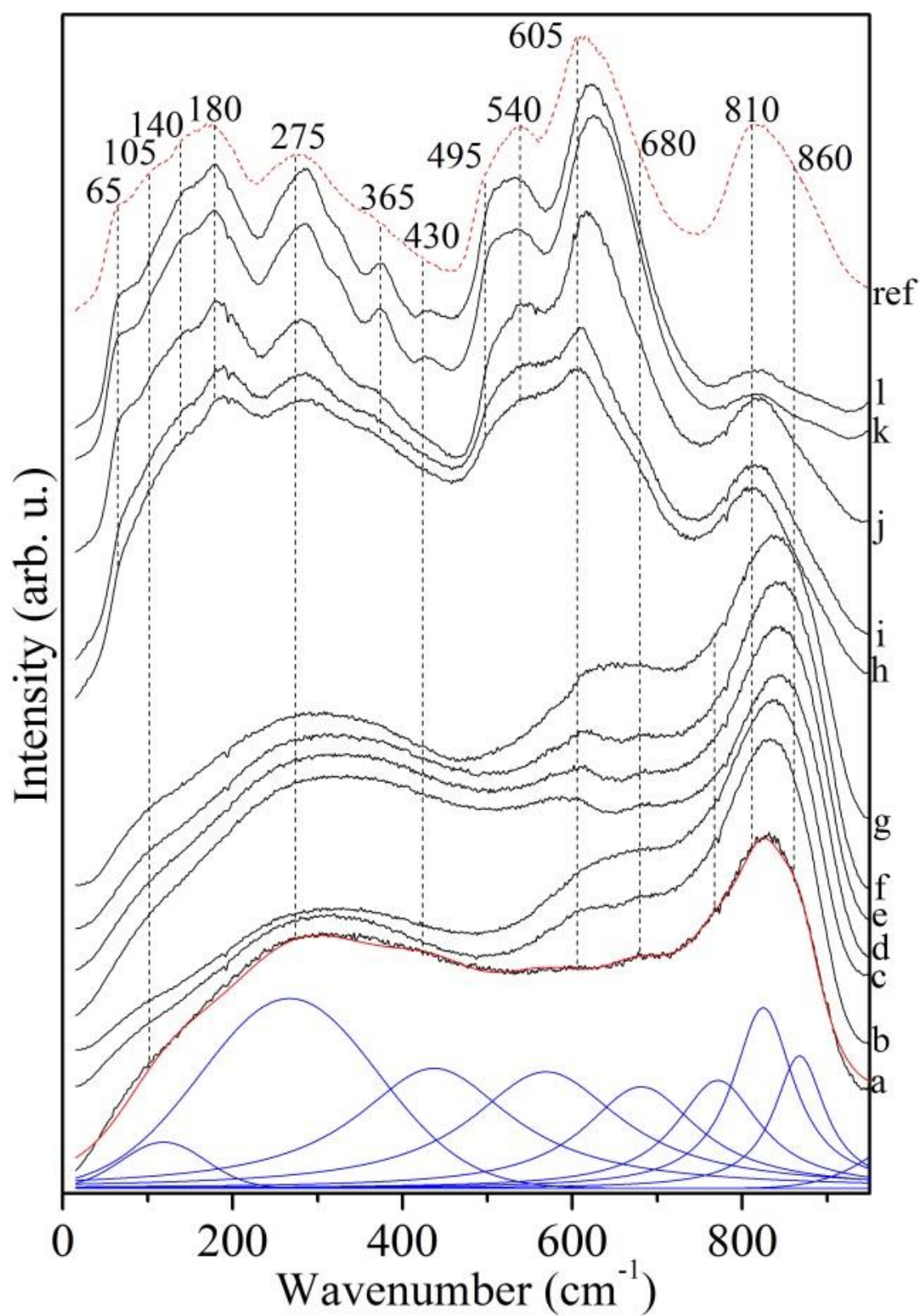
2.7 Results

Fig. 27. Raman spectra of Miass pyrochlore before annealing (a) and after annealing steps of 400 K (b), 500 K (c), 600 K (d), 700 K (e), 780 K (f), 790 K (g), 800 K (h), 810 K (i) and of untreated Schelingen pyrochlore (ref).

[54]

2.7.5 Newania pyrochlores

In addition to these five idiomorphic and chemically rather homogenous pyrochlore samples chosen to establish the 605/810 cm^{-1} band ratio as an indicator for the short-range degree of metamictization, unoriented pyrochlores from Newania, Rajasthan, India, were also probed using Raman spectroscopy (Viladkar *et al.*, in print). Electron microprobe analyses showed inhomogeneous UO_2 content from 0.99% to 18.63%, often within single grains of 50-200 µm diameters. Next to sharp Raman signals at low wavenumbers and a distinct band at 250 cm-1, the broad and overlapping 600 and 800 cm^{-1} could also be observed (Fig. 28).
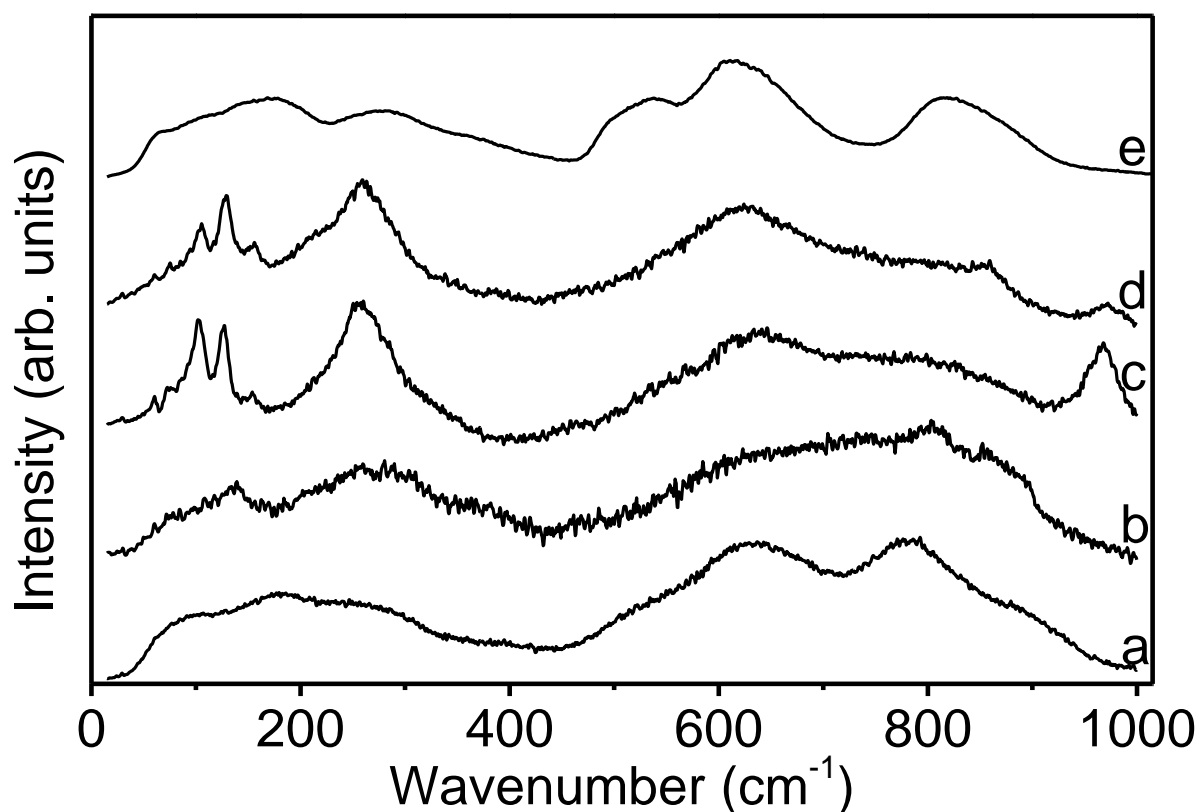

Fig. 28. a–d Raman spectra of 3 Newania pyrochlores, b and c from two different spots of the same pyrochlore. e shows the non-radiation damaged reference pyrochlore from Schelingen, Germany.

2.7.6 Fourier Transform Infrared spectroscopy (FTIR)

The infrared spectrum of the Schelingen pyrochlore shows broad and overlapping maxima. Like the Raman bands, the infrared bands appear strongly broadened. There are two peak intensities centred on 553 and 710 cm^{-1} respectively (Fig. 29). Both show right-hand

shoulders (centred on 620 and 664 cm^{-1}, and 753, 829 and 895 cm^{-1}, respectively). Minor shoulders occur at 664, 753, 829 and 895 cm^{-1}.
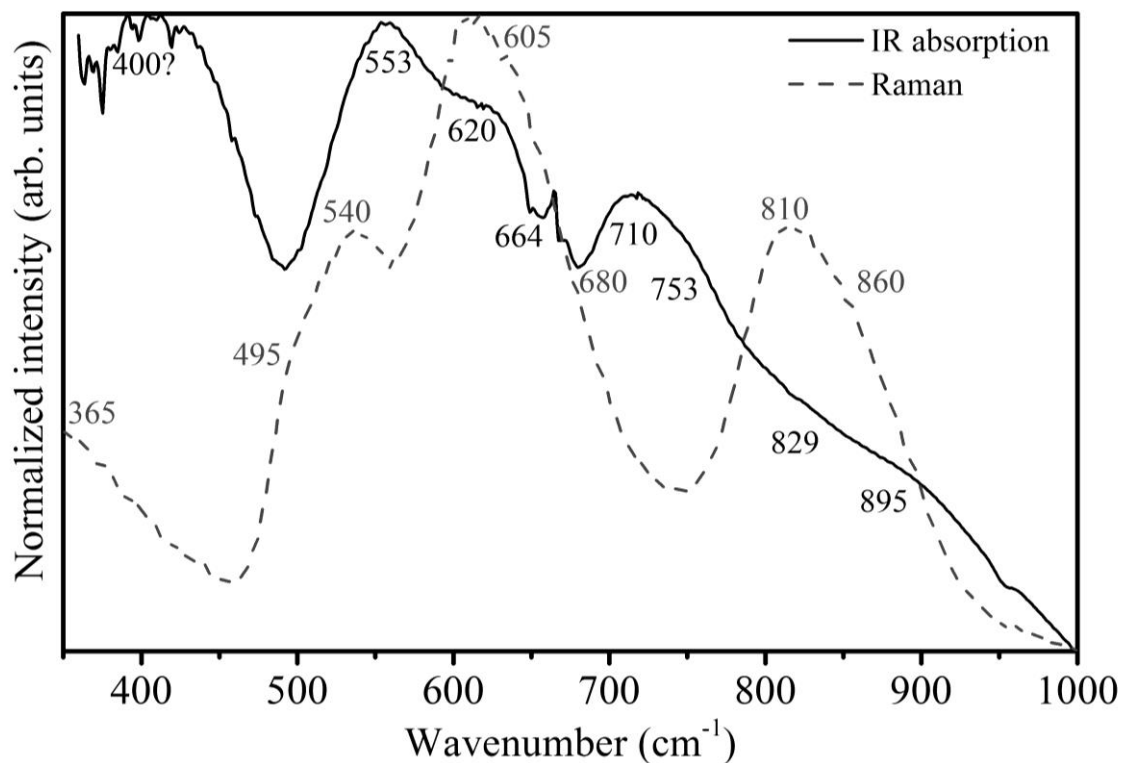

Fig. 29. Comparison of Raman and FTIR spectra of the untreated Schelingen sample.

2.7.7 Thermal analysis

The combined Differential Scanning Calometry / Thermogravimetry (DSC/TG) measurement for the three pyrochlores Panda Hill, Blue River and Miass showed a constant decrease in weight with temperature and one to several temperature intervals of increased heat flux with an overall constantly decreasing heat flux in the annealing range up to 1000 K.

The Panda Hill sample shows major heat flux increase starting at 483 K with a maximum at 660 K followed by a shallow decrease to below the initial heat flux level at 850 K. At 940 K starts a further increase. The samples weight drops continuously by less than 1 % at 1000 K (Fig. 30a).

The Blue River pyrochlore shows an increase of heat flux starting at 433 K with a maximum at 610 K. At 680 K a second increase overlaps the first showing a maximum at 735 K. A third very sharp increase peaks at 780 K. The weight loss is 1.5 % up to 1000 K. There is a sharper weight loss coinciding with the first increase in DSC (Fig. 30b).

2.7 Results

In the metamict Miass sample a very shallow signal increase starts at 470 K with a maximum around 530 K. A sharp signal peaks at 850 K starting at 830 K. The weight loss is in the magnitude of 3 % with an almost constant weight loss from 490 K upwards (Fig. 30c).
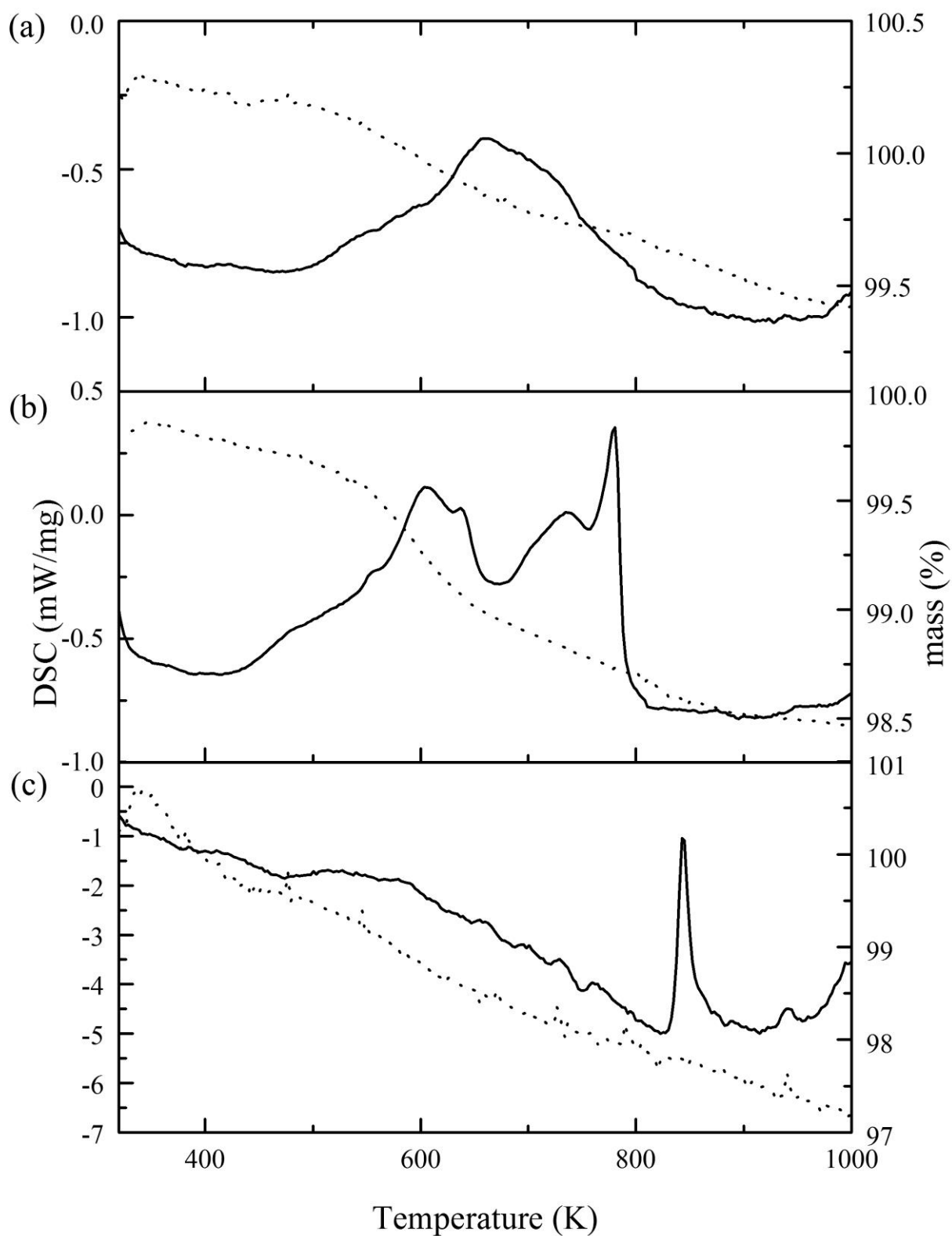
2.7 Results

Fig. 30. Differential scanning calometry curves (solid line, left axis) and thermogravimetry (dotted line, right axis) of pyrochlores from Panda Hill (a), Blue River (b) and Miass (c).

2.8 Discussion

2.8.1 Electron microprobe analysis

Electron microprobe analysis showed the general homogeneity of the samples. Ca is always the main A-site cation – ranging from 0.79 (Blue River) to 1.37 (Schelingen) atoms per formula unit. Nb is the main B-site cation with 1.48 (Blue River) to 1.87 (Schelingen) atoms per formula. F is the major Y-site element of the radiation-damaged samples (0.52 apfu in Blue River and 0.86 apfu in Miass pyrochlore). Although they show some variation, they are comparable in composition.

Schelingen pyrochlore has a rim which is enriched in lighter elements. Panda Hill showed zoning with enriched heavy elements. Both regions were excluded from the average and later Raman measurements were performed in the homogeneous area. In Raman analyses Panda Hill furthermore showed small apatite inclusions which were not seen in the sample pieces probed by EMP and XRD.

Calculating the content relative to 2 B-site cations results in the following sum formulae:

$(Na_{0.3}Ca_{1.4}Fe_{0.1}REE_{0.2})$ $(Ti_{0.1}Nb_{1.9}Zr_{0.1})$ $O_6(O_{0.8}F_{0.4}(OH)_{0.1})$ (Schelingen),

$(Na_{0.6}Ca_{1.2}\square_{0.2})$ $(Ti_{0.2}Nb_{1.7})$ $O_6(O_{0.1}F_{0.8}\square_{0.1})$ (Panda Hill),

$(Na_{0.6}Ca_{0.8}U_{0.2}\square_{0.4})$ $(Ti_{0.2}Nb_{1.5}Ta_{0.3})$ $O_6(O_{0.2}F_{0.5}\square_{0.3})$ (Blue River)

$(Na_{0.7}Ca_{1.0}REE_{0.2}Th_{0.1})$ $(Ti_{0.5}Nb_{1.5})$ $O_6(O_{0.1}F_{0.8}\square_{0.1})$ (Zlatoust) and

$(Na_{0.7}Ca_{1.0}REE_{0.2}Th_{0.1})$ $(Ti_{0.5}Nb_{1.5})$ $O_6(O_{0.1}F_{0.9})$ (Miass).

Hydrous species play a minor role in the analysed samples as the Raman spectra only showed a weak signal in Blue River pyrochlore. The main reason for weight loss seen in thermogravimetry may result from water and/or He or fluorine leaking during recrystallization.

As the phonon bands visible in the Raman spectra should stem from oxygen displacements only, the occupation of 6-coordinated B- (5 phonon modes of neighbouring oxygen atoms) and especially A-site (1 phonon mode of neighbouring oxygen atoms) cations should only be minor in ideal pyrochlore structure. Nonetheless, solid solution will contribute to the band broadening.

2.8 Discussion

From the actinide content measured by EMP (Table 1) and geologic age the total radiation dose can be calculated using α-decays of the ^{232}Th-, ^{235}U- and ^{238}U-decay series as given by Nasdala (Nasdala *et al.* 2001):

$$D_\alpha = 8 \frac{c_U N_A 0.9928}{M_{238} 10^6} \left(e^{\lambda_{238} t} - 1 \right)$$

$$+7 \frac{c_U N_A 0.0072}{M_{235} 10^6} \left(e^{\lambda_{235} t} - 1 \right)$$

$$+6 \frac{c_{Th} N_A}{M_{232} 10^6} \left(e^{\lambda_{232} t} - 1 \right)$$

with U and Th concentrations c_U and c_{Th} in ppm, Avogadro's number N_A, molecular weights of parent isotopes M_{238}, M_{235} and M_{232}, decay constants λ_{U238}, λ_{U235} and λ_{Th232} (Meija *et al.* 2016) and the reported geologic age t in years (Table 5). Actinide contents range from qualitative detection limit to 10.6 wt%, resulting in doses of 0.01 to 115.4×10^{18} decay events per gram by considering the reported crystallisation ages of the carbonatite host rocks. After metamictization, geological conditions may have altered the amorphous state of the samples. More recent deformation ages of host rocks, when the crystal structure might have been (partially) reset, were the metamorphism of the Rocky Mountains and the Urals when temperatures needed for structural healing could have been reached. Doses in Table 5 are the maximum life-time doses.

Table 5. Ages and doses of pyrochlore samples.

Sample	Th (wt%)	U (wt%)	Geologic age (Ma)	Dose (10^{18} α-decays g^{-1})
Schelingen	<0.1	0.1±0.1	16±2[1]	<0.1
Panda Hill	1.6±0.1	0.1±0.1	116±6[2]	1.6±0.1
Blue River	0.1±0.1	10.5±0.1	328±30[3]	115.4±1.0
Zlatoust	6.1±0.1	0.1±0.1	432±12[4]	23.1±0.6
Miass	6.4±0.1	0.1±0.1	432±12[4]	23.1±0.6

[1] Lippolt (1963), [2] Bell & Blenkinsop (1987) [3] Berger *et al.* (2009), [4] Krasnobaev *et al.* (2010)

2.8.2 X-ray diffraction

Integrated Bragg signal and amorphous background intensities were used to estimate the amorphous fraction. The diffraction signal sharpened and the amorphous background decreased significantly with annealing for all samples except the crystalline reference material, indicating recrystallization on the mesoscopic length scale. The stronger the

2.8 Discussion

structure's destruction in XRD patterns, the stronger was the sharpening of the diffraction signals during annealing. The integrated intensity of the amorphous background I_{amorph} devided by the sum of integrated background area and integrated Bragg signals quantifies the amorphous fraction X_{amorph} (Fig. 7 a). Errors are in the order of 5%.

$$X_{amorph} = \frac{I_{amorph}}{I_{amorph} + I_{Bragg}}.$$

The comparability of each background measurement was verified by measuring the crystalline Schelingen reference sample. Its background intensity does not change from measurement to measurement so that the analyses are not biased by instrumental conditions. A decreasing cell volume as it was observed would be expected with ordering, e.g. of the polyhedral groups as a whole, or a release of hydrous species or He. An increasing cell volume with temperature, which could go along with metastable thermal expansion, is not seen in any sample.

Powder XRD patterns provide pyrochlore signals with only minor additional phases in crystalline and weakly radiation-damaged samples (Nb-rutile, columbite, lueshite, Fig. 37). Apatite inclusions in Panda Hill pyrochlore that were observed with Raman spectroscopy were not detectable above the XRD background. The metamict Miass sample began to decompose at 820 K to lueshite ($NaNbO_3$). The decomposed fraction remained small up to 1000 K but rose. Blue River pyrochlore showed no chemical instability until the highest annealing temperature (1000 K).

The full width at half maximum (FWHM) of the (440) diffraction signal decreased with increasing annealing temperature for all samples except the crystalline reference sample from Schelingen (Fig. 31b). The Panda Hill sample (▲) shows a minor decrease of FWHM from 0.2° to 0.1° between 500 and 700 K. This linear trend is also visible in the (222) signal. The FWHM of the partially recrystallized Blue River pyrochlore (□) is reduced clearly from 0.3° at ca. 650 K to 0.1° 2θ near 1000 K. Up to annealing temperatures close to recrystallization, diffraction patterns of the metamict Miass pyrochlore (●) show a broad Gaussian-shaped amorphous background centred near 30.3° 2θ. While the FWHM of this background feature decreases following a linear trend from room temperature up to ca. 790 K, only a small and constant amorphous fraction remains visible at temperatures above ca. 850 K. Sharpening of the diffraction signals increases up to the abrupt onset of recrystallization near 790 K.
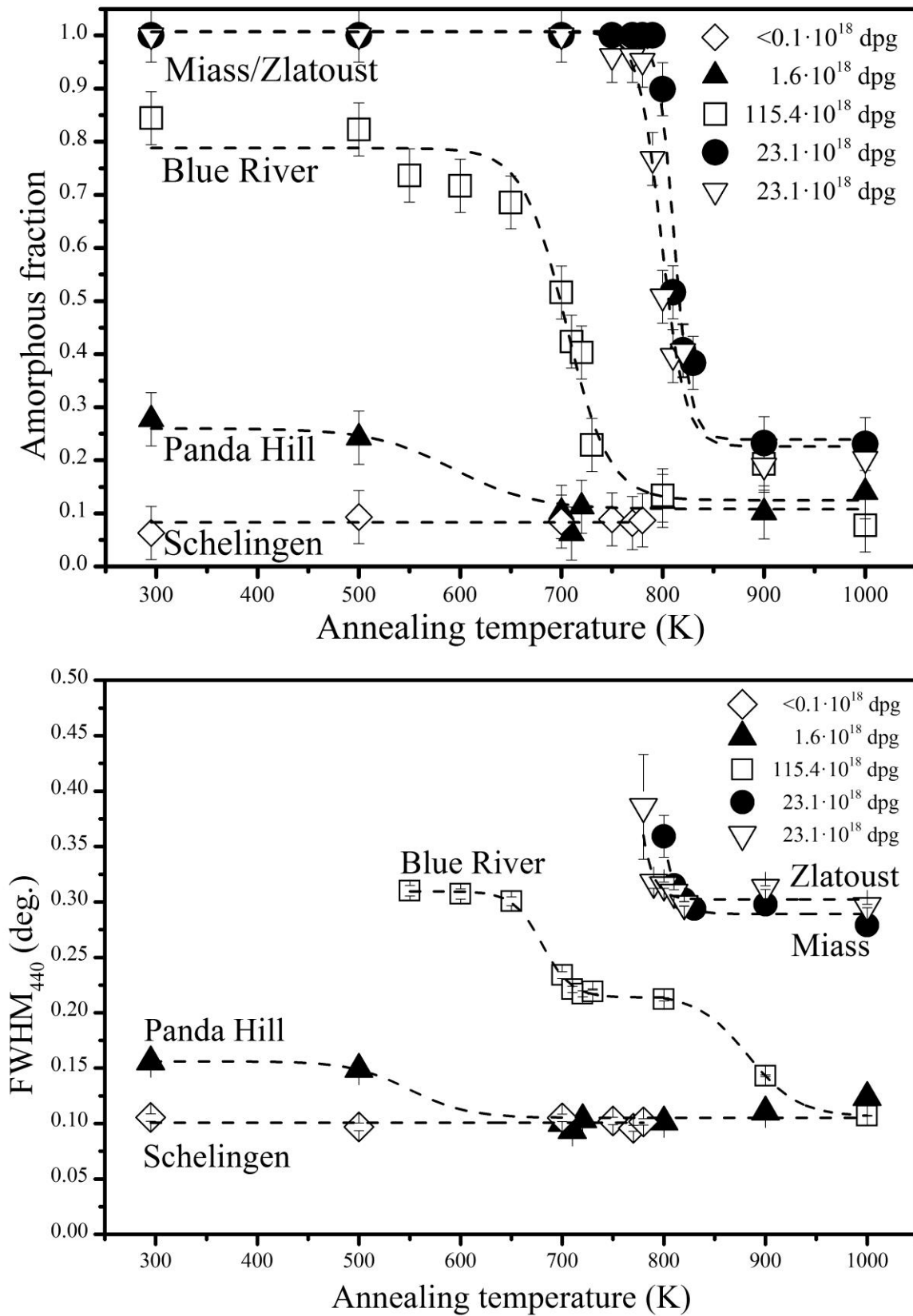
2.8 Discussion

Fig. 31. (a) Amorphous fraction deduced from the XRD amorphous background and the total integrated intensities according to $I_{amorph}/(I_{amorph}+I_{Bragg})$ and (b) FWHM of individual (440) powder XRD signals for pyrochlores from Schelingen ($\diamond$), Panda Hill ($\blacktriangle$), Blue River ($\square$), Zlatoust ($\triangledown$) and Miass ($\bullet$) respectively. Blue River and Zlatoust pyrochlores show only a minor (440) signal below 550 K and 790 K respectively, Miass shows no (440) signal exceeding the background noise below 800 K. Lines are guides for eye.

[62]

The Panda Hill sample was additionally probed by single crystal X-ray diffraction in order to rule out a microcrystalline structure as the Raman signal showed no major intensity changes on rotation, although the sample was not amorphous. Sharp reflexes, however, confirmed an either strongly textured or even monocrystalline structure.

Recrystallization is strongly related to the initial degree of metamictization. While the moderately damaged Panda Hill pyrochlore (amorphous fraction 28 %) shows an increased recrystallization between 500 and 700 K, highly damaged Blue River pyrochlore (amorphous fraction 85 %) starts recrystallizing at a similar temperature, but shows a sharp decrease in amorphous fraction between 700 and 800 K. In contrast, both metamict samples recrystallize in a narrow temperature range of 800 to 850 K.

2.8.3 Raman spectroscopy

Observed modes in pyrochlores are centred at 65, 105, 140, 180, 275 (T_{2g}), 365 (E_g), 430, 495 (A_g), 540 (T_{2g}), 605 (T_{2g}), 680, 810 and 860 cm^{-1} (Fig. 24, Fig. 25, Fig. 26, Fig. 27). The five main Raman bands (180, 275, 540, 610 and 810 cm^{-1}) occur in all samples despite their chemical differences and local structural heterogeneities. As Raman modes in the ideal pyrochlore structure are only caused by the excitement of the X- and Y-site oxygen atoms, cation-site occupancies should affect the signal only secondary. Raman band intensities in cross-polarised arrangements between 450 and 1000 cm^{-1} show considerably lower intensities than the parallel-polarised measurements. Such stronger intensities indicate symmetrical stretching A-modes.

The experimentally observed Raman signals are strongly broadened and show considerable overlap. In addition the Miass pyrochlore shows photoluminescence in the whole spectral range under investigation. Therefore, the pyrochlore spectra of the untreated samples with high degree of metamictization should be interpreted carefully.

From model calculations - verified by experimental measurements - bands have been assigned in literature for deviating composition as A_{1g}-mode in a range of 482-550 cm^{-1}, E_g-mode 281-331 cm^{-1}, and the T_{2g} modes 166-258, 275-450, 450-537, 549-883 cm^{-1} (Vandenborre *et al.* 1983; Fischer *et al.* 2008; Ronconi & Alves 2003; Arenas *et al.* 2010; Hong *et al.* 2003; Li *et al.* 2014; Radhakrishnan *et al.* 2011; Wang *et al.* 2007; Kamba *et al.* 2002; Geisler *et al.* 2004; Mihailova *et al.* 1997; Kulriya *et al.* 2015; Zhang *et al.* 2010;

2.8 Discussion

Glerup *et al.* 2001; Mączka *et al.* 2008; Saha *et al.* 2011; Mączka *et al.* 2009; Moll *et al.* 2011; Park *et al.* 2014; Sattonnay *et al.* 2010; Lummen *et al.* 2008; Begg *et al.* 2001; Lang *et al.* 2009; Sattonnay *et al.* 2013; Mandal *et al.* 2010; Gregg *et al.* 2013; Hess *et al.* 2002; Mandal *et al.* 2009). Assignments of the fundamental vibrational modes to different chemical compositions in the literature are given for the range 140 to 650 cm^{-1}, see Fig. 32. The broad mode above 700 cm^{-1} was assigned either to the T_{2g} vibration (Fischer *et al.* 2008), to a forbidden mode or to a combination of excitations (Glerup *et al.* 2001; Vandenborre *et al.* 1983).
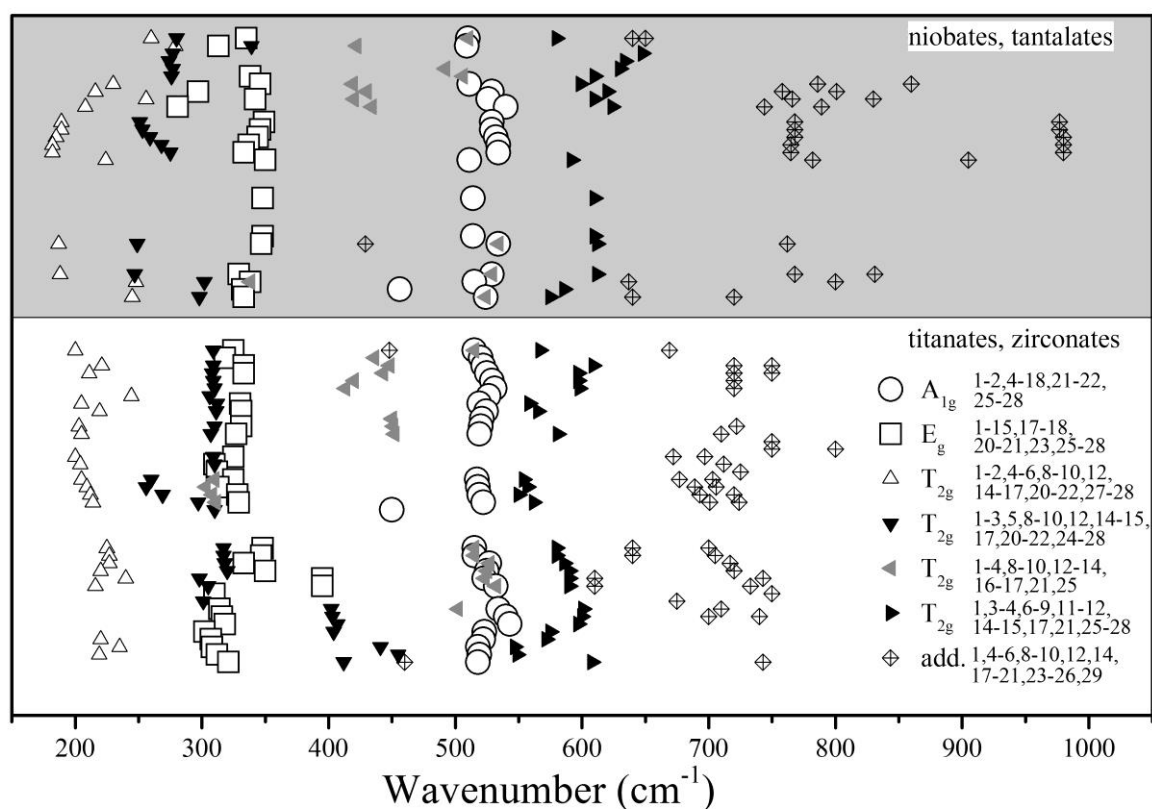

Fig. 32. Experimentally observed peak positions of the Raman bands of pyrochlores and their mode assignments (Vandenborre *et al.* 1983[1]; Fischer *et al.* 2008[2]; Ronconi & Alves 2003[3]; Arenas *et al.* 2010[4]; Hong *et al.* 2003[5]; Li *et al.* 2014[6]; Radhakrishnan *et al.* 2011[7]; Wang *et al.* 2007[8]; Kamba *et al.* 2002[9]; Geisler *et al.* 2004[10]; Mihailova *et al.* 1997[11]; Kulriya *et al.* 2015[12]; Zhang *et al.* 2010[13]; Glerup *et al.* 2001[14]; Mączka *et al.* 2008[15]; Saha *et al.* 2011[16]; Mączka *et al.* 2009[17]; Moll *et al.* 2011[18]; Park *et al.* 2014[19]; Sattonnay *et al.* 2010[20]; Lummen *et al.* 2008[21]; Begg *et al.* 2001[22]; Lang *et al.* 2009[23]; Sattonnay *et al.* 2013[24]; Mandal *et al.* 2010[25]; Gregg *et al.* 2013[26]; Hess *et al.* 2002[27]; Mandal *et al.* 2009[28]).

Pyrochlores of different compositions show comparable Raman spectra because of the oxygen-dependence of Raman-modes that does not vary much with cation variation. As

2.8 Discussion

pyrochlore minerals have several impurities, the Raman bands are expected to be broadened and vacancies can lead to broken selection rules.
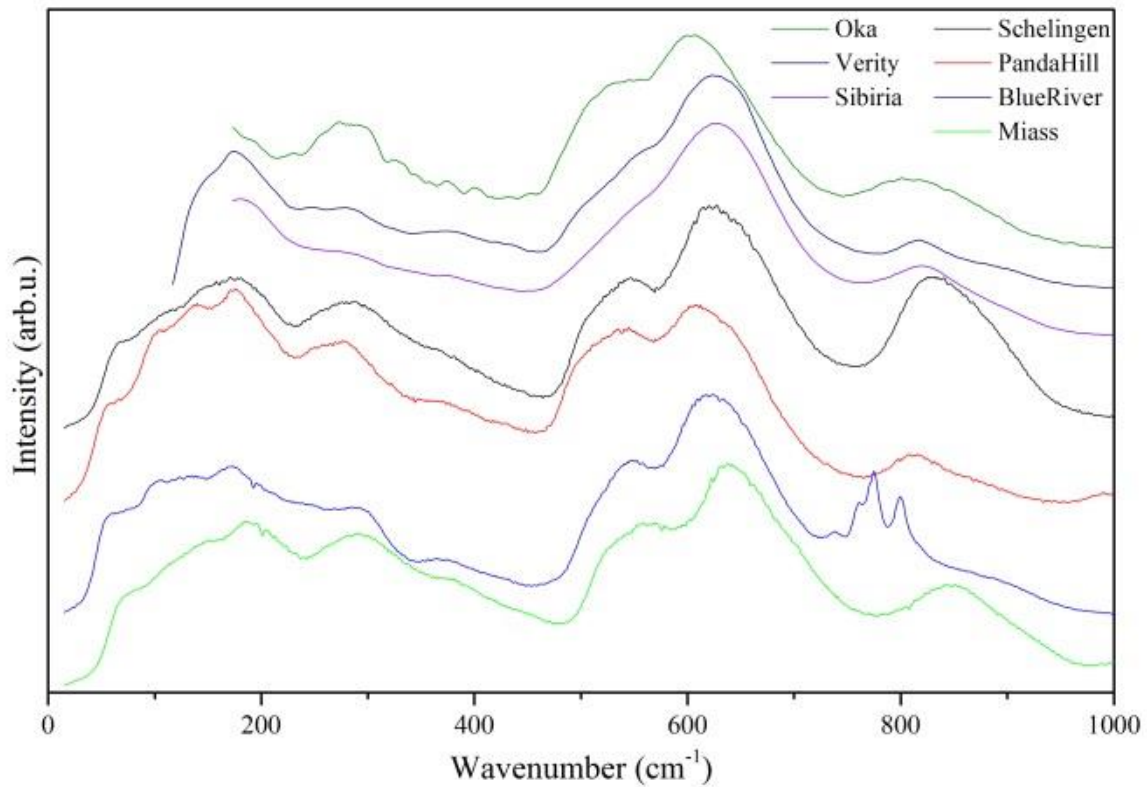

Fig. 33. Spectra of recrystallized pyrochlores (Panda Hill, light green; Blue River, blue; Miass, red; annealed at 1000 K) in comparison to the room temperature spectrum of Schelingen pyrochlore (black), and pyrochlores (Oka, violet; Verity, dark blue; 'Sibiria', dark green) from RRUFF database (Lafuente *et al.* 2015).

The Raman signals at wavenumbers between 700 and 1000 cm^{-1} are sometimes associated with a vibrational mode not occurring in the crystalline but in amorphous structure (e.g. Vandenborre 1983, Moll 2011, Park 2014, Lang 2009, Sattonay 2013). Relating the integrated intensities of the clearest and largest signal at 605 cm^{-1} together with its shoulder peak at around 670 cm^{-1} to the 810 cm^{-1} signal, this ratio can indicate the short-range order.
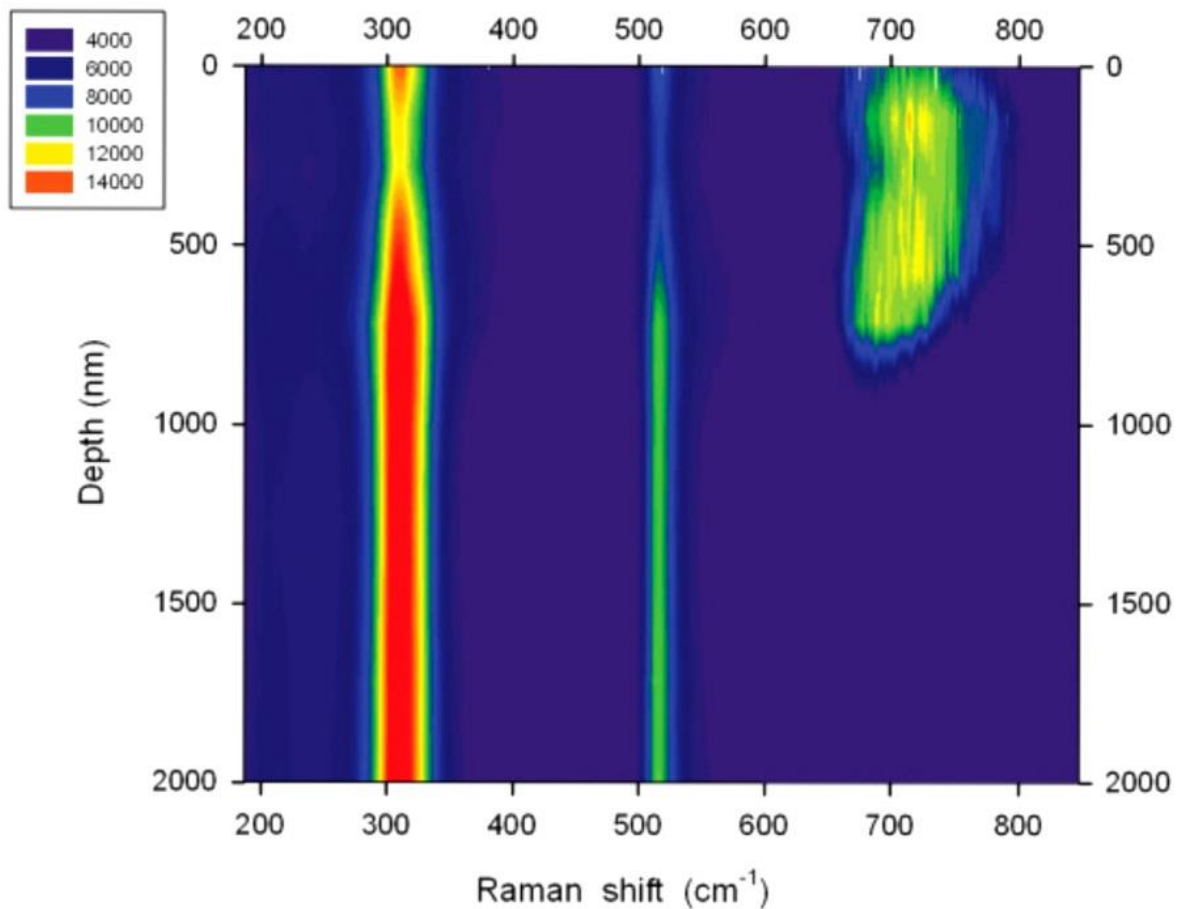
2.8 Discussion

Fig. 34. Irradiated (4-MeV Au ions at 1 ion nm^{-2}) thin sheets of pyrochlore structure (Gd$_2$Ti$_2$O$_7$) showing a broad Raman signal ~710 cm^{-1} in the radiation-damaged volume, measured by (Moll *et al.* 2011).

Vandenborre *et al.* (1983) assumed the 810 cm^{-1} band to be a combination band. One further possibility for the appearance of the Raman band near 810 cm^{-1} may be broken selection rules leading to an infrared signal near 829 cm^{-1} to become visible in the Raman spectrum (Fig. 29). The Raman intensity, however, displays the crystalline fraction insofar that the recrystallization is inversely correlated with its 810 cm^{-1} mode intensity. 810 cm^{-1} could occur because of a distortion of the corner-sharing octahedral network meaning that the phonons would be related to a higher order change, e.g. in the rings, rather than in the distortion of the polyhedra. Fluorite as the parent structure can also show an excitation in the 800-870 cm^{-1} range that is not a first-order phonon mode.

Actinide-oxygen modes could also be an explanation for the broad 810 cm^{-1} excitation observed in the pyrochlore minerals of this study. But if that would be the case, this would mean that a regular actinide-oxygen excitation would only occur in the disordered state. This is rather unlikely. A relation to the amorphous fraction independent of the actinide content is

2.8 Discussion

also illustrated by the actinide-free irradiation study of Moll *et al.* (Moll *et al.* 2011), shown in Fig. 34.

A localized mode (Anderson localization) not visible in XRD can occur for a certain degree of disorder (Anderson 1958). Instead of broaden one signal, this can result in a two-mode excitation close to the end members of the site occupancy in solid solution (Chang & Mitra 1971).
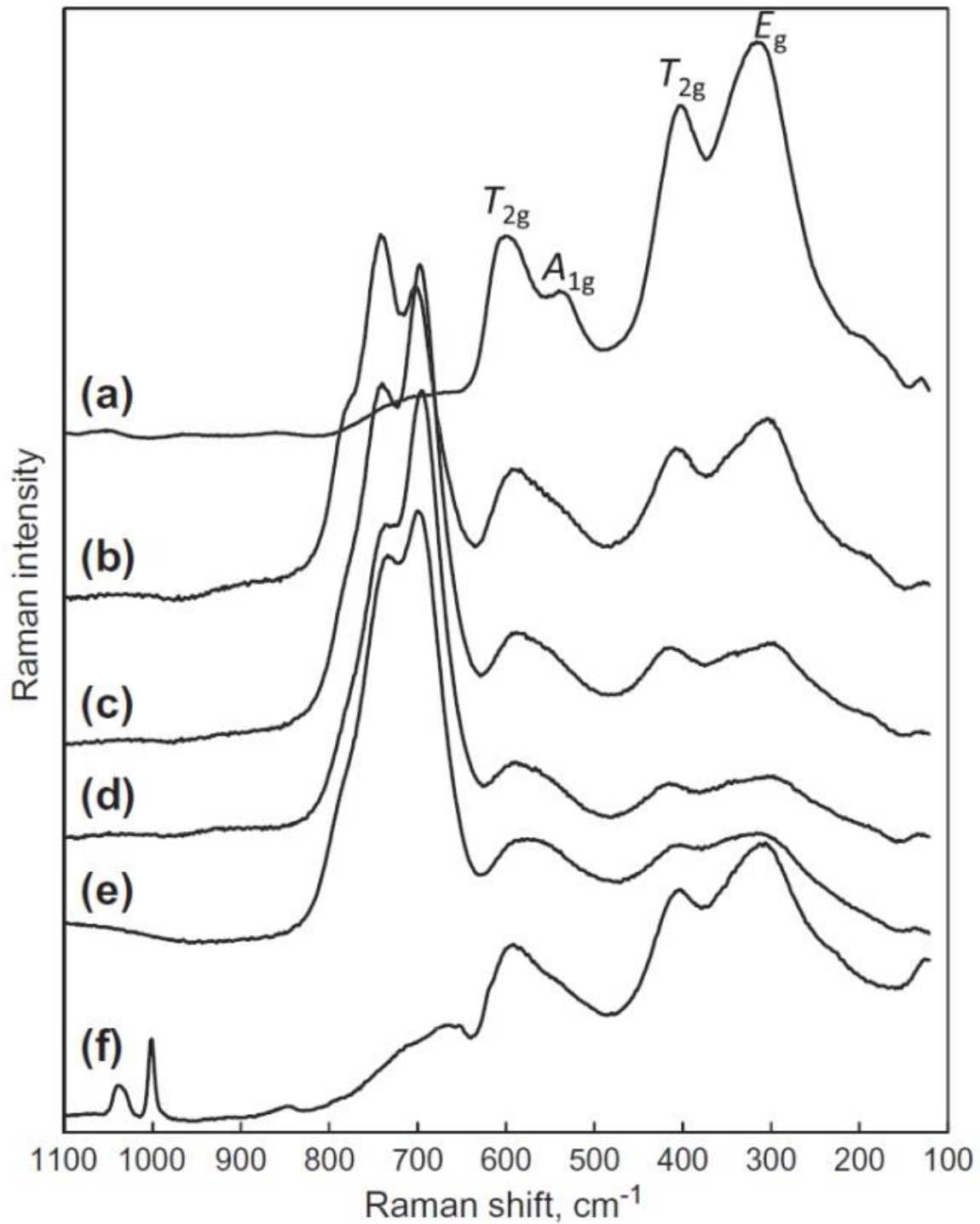
2.8 Discussion

Fig. 35. Raman spectra of air-sintered $Gd_2Zr_2O_7$ without (a) and doped with $U_{0.1}$ (b), $U_{0.2}$ (c), $U_{0.2}$, less Gd (d), $U_{0.2}Ca_{0.2}$ (e), $U_{0.2}Ca_{0.2}$ (e), sintered under N_2-H_2 atmosphere (f) (Gregg *et al.* 2013).

Gregg *et al.* (2013) studied the effect of U-incorporation in a $Gd_2Zr_2O_7$ pyrochlore structure (see Fig. 35). Raman spectra of their analyses showed strong signals between 650 and 800 cm^{-1} with centres around 700 and 740 cm^{-1}, respectively (Manara & Renker 2003).

[68]

2.8 Discussion

They attributed these modes to a combination of two U-O stretching modes, typical for U^{6+} in α-U_3O_8 (700 cm^{-1}) and γ-UO_3 (740 cm^{-1}).

Ta-O modes are also a possible explanation for additional Anderson localized modes in the 700-800 cm^{-1} range mainly assigned to Ta-O stretching modes of corner- or edge-sharing polyhedral (Dobal *et al.* 2001). Dobal *et al.* observed two modes, one centered at 710 and one at 770 cm^{-1} in TiO_2-doped Ta_2O_5 (see Fig. 36). Although crystallizing in a different space group, Ta-O excitations in Ta_2O_5 may resemble Ta-clusters in the probed minerals, especially when doped with Ti.
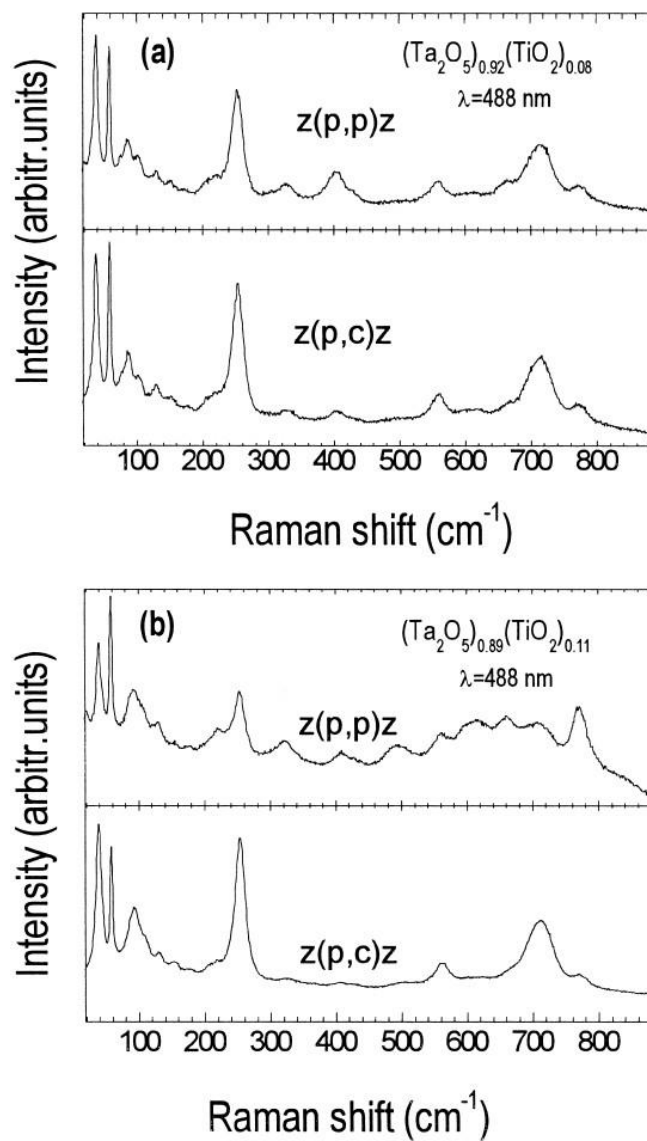

Fig. 36. Polarized Raman spectra of synthetic (a) $(Ta_2O_5)_{0.92}(TiO_2)_{0.08}$ and (b) $(Ta_2O_5)_{0.89}(TiO_2)_{0.11}$ crystals at room temperature (Dobal *et al.* 2001).

[69]

2.8 Discussion

Nb-rutile and lueshite both have their two major Raman bands around 600 and 800 cm^{-1}. Their contribution to the observed spectra is nevertheless small as the two main signals of lueshite do not exactly coincide (see Fig. 37). The main signal of pure NaNbO$_3$ at 576 cm^{-1} is positioned at a local minimum in the pyrochlore spectra. A shift of minor phase Raman bands is a possible result of included impurities. Raman spectra from RRUFF database (Lafuente *et al.* 2015) recorded at 532 nm laser wavelength compared to 514.5 nm excitation wavelength in this work.
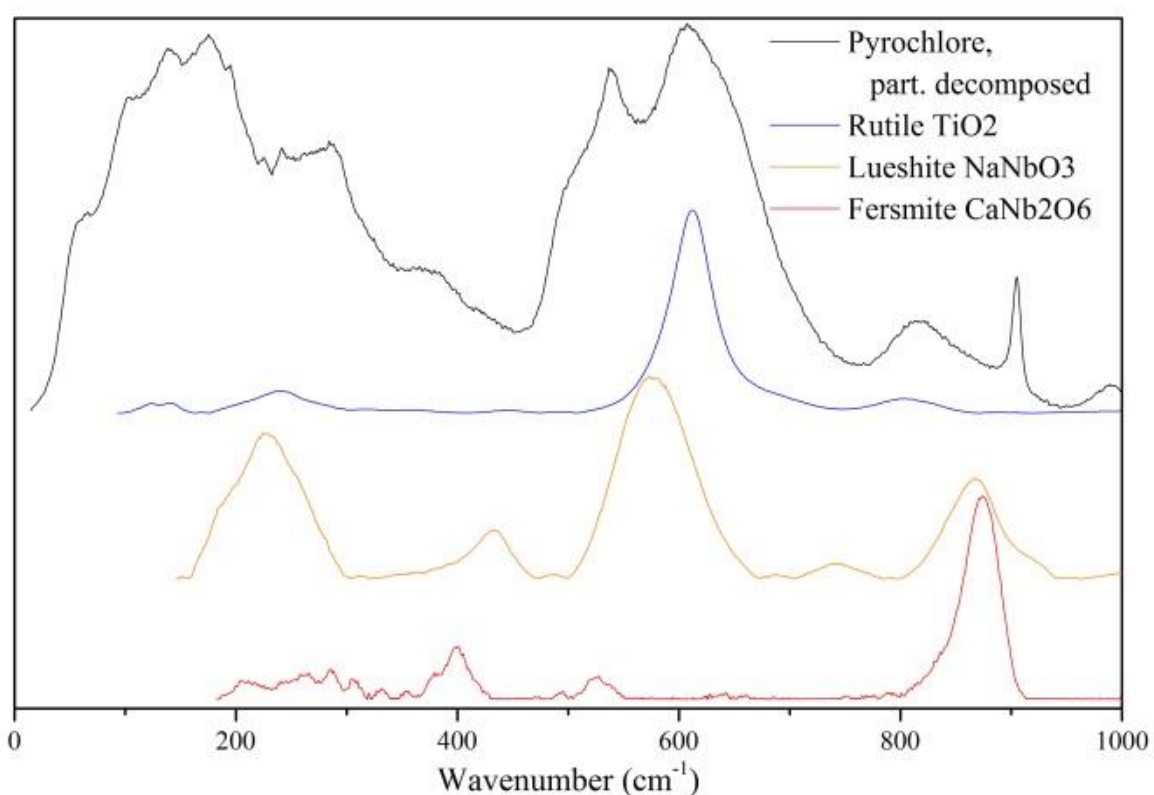

Fig. 37. Raman spectrum of partially decomposed Panda Hill pyrochlore (annealed at 1400K, black line) in comparison to possible products of high-temperature decomposition Nb-rutile (blue), lueshite (NaNbO$_3$, orange) and fersmite (CaNb$_2$O$_6$). Non-pyrochlore data from RRUFF database (Lafuente *et al.* 2015).

The bands were assigned following Vandenborre & Husson (1983) who compared experimental vibrational spectra of several synthetic A$_2^{II}$B$_2^{V}$O$_7$ and A$_2^{III}$B$_2^{IV}$O$_7$ pyrochlores to the calculated modes using ten force and interaction constants. They found for the B-O bonds as the main contributors to the Raman bands that the mass differences for transition elements with very similar electronegativities (like Nb^{5+}, Ta^{5+} and Ti^{4+}, each between 1.5 and 1.6 (IUPAC. Compendium of Chemical Terminology, 2nd ed.) are masked by the dependency of

2.8 Discussion

the force field on the atomic number. Therefore spectra would look very similar. Force field constants of A-O or A-O' (with O' on 8b and O on 48f position) bonds were calculated 6-8 times smaller than the bonds in the octahedral (Vandenborre & Husson 1983).

Five main bands are visible in Raman spectra of all the recrystallized pyrochlores (180, 275, 540, 605 and 810 cm^{-1}, Fig. 24, Fig. 25, Fig. 26, Fig. 27) irrespective of the minor variations in composition (Ta- and Ti-content at the B-site, Ca- and actinide content at the A-site). The 605 cm^{-1} excitation (T_{2g}) becomes the strongest signal with recrystallization while the mode near 810 cm^{-1} sharply shrinks. In general, signal broadening is expected resulting from compositional impurities in a solid-solution mineral such as pyrochlore. Structural disorder should further broaden the signal.

The main differences in the sample spectra result from photoluminescence of the metamict samples in the lower wavenumbers (<600 cm^{-1}) and the change in the 810 cm^{-1} excitation. While photoluminescence fully disappears upon recrystallization, the 810 cm^{-1} band remains present until 1400 K-annealing, but clearly decreases. As the 810 cm^{-1} excitation is related to radiation damage, recrystallization at the local length scale can be deduced from the evolution of the intensity relation of the bands near 605-680 cm^{-1} and 810-860 cm^{-1} at different annealing steps.
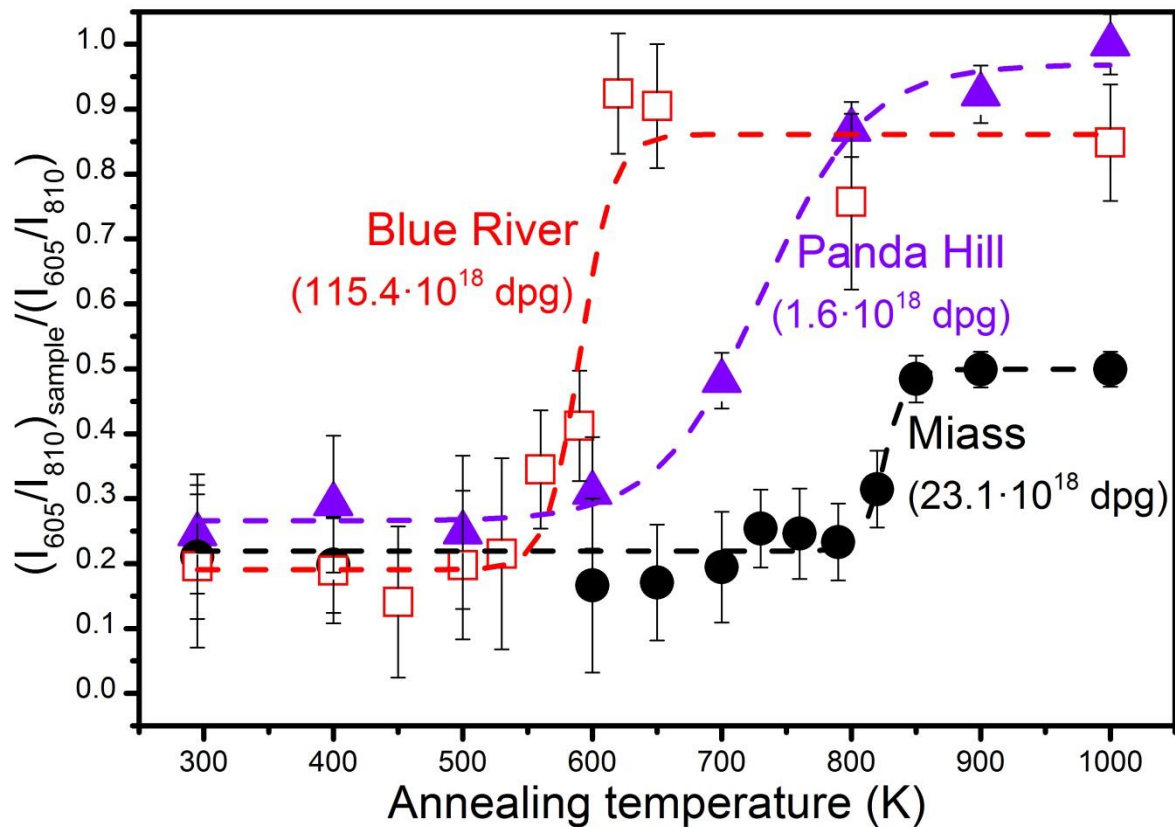
2.8 Discussion

Fig. 38. Ratio of the sum of integrated intensities of fitted modes 605 and 680 cm^{-1} divided by the integrated intensity sum of modes 810 and 860 cm^{-1} for weakly amorphous Panda Hill (▲), intermediate Blue River (□) and strongly metamict Miass (●) pyrochlores (dashed lines are guide for the eye).

Additional sharp signals between 730 and 800 cm^{-1} as occurred in the Blue River pyrochlore, starting after an annealing temperature of 620 K, are not observed in the other samples. Their intensities were not included in the calculation of 605+680 to 810+860 cm^{-1} ratio for high temperature annealing (800 K and 1000 K) where they showed a very sharp signal. At annealing temperatures of 620 and 650 K their very low excitations were not fitted with distinct Lorentzians, but included in the 810 cm^{-1} peak fitting. The main compositional differences of this sample are the Ta- and U-contents. U only occurs around the detection limit in all other samples, Ta only in minor amounts (maximum of 1.7 wt% in Zlatoust pyrochlore). Blue River pyrochlore showed a content of 14.9 wt% Ta and 10.5 wt% U meaning that the B-site is statistically occupied by 17.5% Ta-atoms and the A-site by 9.3% U-atoms. As XRD patterns show no different Bragg signals after these annealing steps, they should result from a local phenomenon or a surface reaction. Interestingly, these excitations decrease again after annealing above 1000 K. Their intensity maximum coincides with the appearance of darker regions along fissures, seen in the microscope. The measurements took

2.8 Discussion

place outside these regions, but there may have been some surface reaction at the probed region not visible in the microscope.

While Ta^{5+} cations have similar ionic radius to Nb^{5+}, their mass of 180.9 amu compared to 92.9 amu for Nb^{5+} differs considerably. With increasing degree of order at the B-site, bands are expected to shift to lower wavenumbers (assuming unchanged coordination) which is indeed observed for all samples after annealing.

Vandenborre *et al.* (1983) assumed the 810 cm^{-1} band to be a combination band. One further possibility for the appearance of the Raman band near 810 cm^{-1} may be broken selection rules leading to the infrared signal near 829 cm^{-1} which may then become visible in the Raman spectrum. The Raman intensity, however, displays the crystalline fraction insofar that the disorder is inversely correlated with its mode intensity.

Broken selection rules occur if there is lower symmetry in the real structure compared to ideal arrangements. This is the case for the relevant short range coordination if additional vacancies and impurities distort the local symmetry. The comparison of Raman and infrared spectra confirms such a violation of selection rules in pyrochlores. With its centrosymmetric space group the pyrochlore structure should not show infrared-active bands where the same bands are Raman-active.

Fig. 29 shows that the crystalline reference sample has infrared maxima centred at 553, 620, 664 and 829 cm^{-1}, corresponding to Raman shifts centred at 540, 610, 680 and 810 cm^{-1}. Six of the seven fundamental infrared-active modes were observed between 70 and 523 cm^{-1} in chemically comparable niobate pyrochlores (Fischer *et al.* 2008; Arenas *et al.* 2010). The seventh mode was assigned to an infrared band between 550 and 850 cm^{-1} which could correspond to the observed band at 553 cm^{-1} in the Schelingen sample. Additional infrared bands within this range are either not fundamental modes or related to clusters with lighter or stronger bond substitutional ions.

The low sensitivity of Raman intensity upon rotation in the untreated samples means that there are almost no orientational effects upon rotating for 45°. The only larger intensity deviation occurred around the 300-350 cm^{-1} band containing the E_g mode. Hence, there is random polyhedral coordination in the untreated samples – even in the low-damaged Panda Hill pyrochlore.

2.8.4 Newania pyrochlore

The spectra of the unoriented Newania pyrochlores (Fig. 28) show bands not observed in the chemically more homogeneous pyrochlores. A minor phase probably overlaps the pyrochlore signal. Low 605/810 cm^{-1} ratios indicate a low crystallinity. The last known metamorphic event at the Newania site at ~904 Ma (Ray *et al.*, 2013; Schleicher *et al.*, 1997) reached high enough temperature to completely reorder former structural damage. The high actinide contents would allow for complete metamictization since. Partially pronounced 605 cm^{-1} bands, however, may indicate a local minimum of U content.

2.8.5 Thermal analysis

Most of the recrystallization of the pyrochlore sample from Panda Hill takes place between 500 and 800 K according to Raman spectroscopic and powder XRD measurements (see Fig. 18, Fig. 19, Fig. 20, Fig. 21, Fig. 24, Fig. 25, Fig. 26, and Fig. 27). The results of the DSC measurements support this very well, showing the occurrence of an exothermic reaction with a maximum in this temperature region, accompanied by an increase in weight loss (Fig. 30). Pyrochlore from the Blue River locality shows sudden recrystallization on the local length scale over a short temperature region, between 530 and 620 K according to Raman spectroscopy. This is consistent with the DSC results, which show a first broadened exothermic maximum around 610 K (Fig. 30b). It can be assumed that the further sharp and defined maximum around 785 K is related to a further recrystallization step because the behaviour of the main Raman signals already show saturation (Fig. 38). This ongoing recrystallization is indicated by the occurrence of the four additional Raman peaks between 730 and 800 cm^{-1} in the annealing range between 590 and 1000 K (Fig. 31a, Fig. 38). Also, the annealing behaviour of the FWHM of the main (440) pyrochlore diffraction signal clearly indicates the reestablishment of the long-range order, at least up to ~ 1000 K (Fig. 30b).

The DSC signal of the Miass sample shows a strong distinct exothermic peak around 850 K, in good agreement with the results of the Raman spectroscopic and powder XRD measurements which show annealing-induced recrystallization up to ~ 850 K. The change of the shape of the Raman signal between 820 and 850 K (Fig. 31a, Fig. 38) coincides very well with high enthalpy of the exothermic DSC peak in this temperature region (Fig. 30c). Within

2.8 Discussion

the limit of the different annealing rates and hence, different kinetics between DSC-TG (in situ) and Raman spectroscopy and powder XRD measurements (both ex situ) (e.g., heating rate of 10 K/min vs. 1 h annealing at each temperature step) the overall results are in good agreement.

3 Metamict titanite

3.1 Titanite structure

Titanite ($CaTiSiO_5$) is a monoclinic ($P2_1/c$) silicate consisting of corner-sharing TiO_6 octahedra connected by the SiO_4 tetrahedra. Ca^{2+} cations occupy interstitials with 7 oxygen ligands (Speer & Gibbs 1976; Hawthorne *et al.* 1991; Zhang *et al.* 2002; Bismayer *et al.* 2010; Beirau *et al.* 2010).
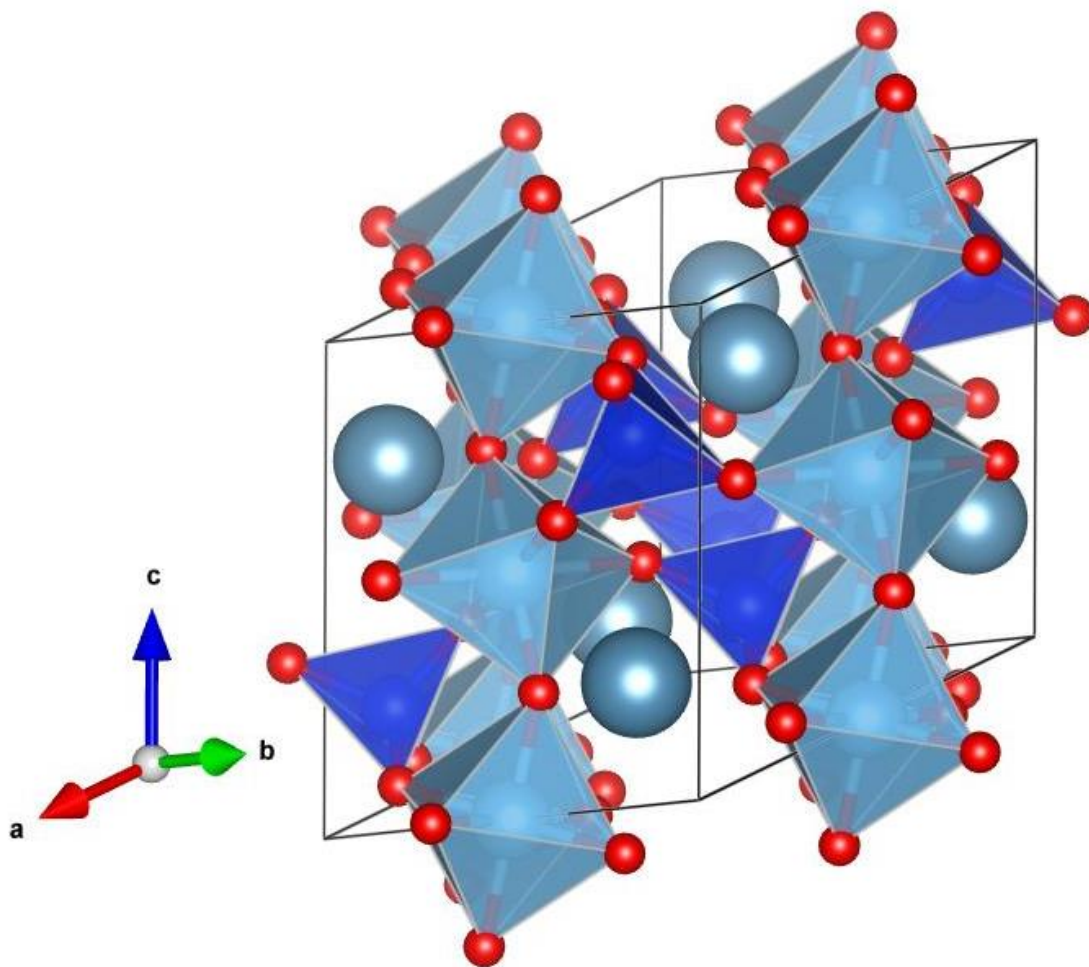

Fig. 39. Titanite structure with octahedrally coordinated Ti, tetrahedrally coordinated Si and Ca atoms in the interstitials.

3.2 Magic angle spin nuclear magnetic resonance spectroscopy (MAS NMR)

For crystalline Rauris and partially amorphous M28696 Cardiff titanites a ^{29}Si magic angle spinning nuclear magnetic resonance spectroscopy was performed. MAS-NMR exploits the

resonance of a radio impulse with the magnetic momentum of the probed isotope. Related energies are quantised

$$E = -\vec{\mu} \cdot \vec{B}$$

with the magnetic moment $\vec{\mu}$ and the external magnetic field $\vec{B}$. [29]Si (abundancy of 4.68% of all Si) has a gyromagnetic ratio $\gamma = \mu/J = 8.458$ MHzT^{-1} (J: total angular momentum, μ: magnetic moment). [29]Silicon cores with a spin of 0.5 align to an external magnetic field (precessing around the magnetic field B with the Larmor frequency ν_0). Their energy level is partially lifted (and their spin is aligned away from the external magnetic field) by a resonant electromagnetic impulse. The relaxing times ('T_1' time towards the external field and 'T_2' time perpendicular to the external field transferring the energy to non-excited cores) back into the initial state are measured and transformed into frequency space by a Fourier transformation.

The electron cloud surrounding the nucleus reduces the external magnetic field. Anisotropy in the electron density and distribution of the core vicinity leads to a shift in the NMR signal. Spinning in a rotation angle of 54.44° towards the static magnetic field B_0 improves the signal quality (Fechtelkord 2004) as higher-order multipolar terms equal out. Chemical signal shifts occur due to different shieldings of the electron cloud in different coordination. [29]Si is measured against a standard (tetramethylsilane, TMS) and given in δ notation as

$$\delta = \frac{\nu_{titanite} - \nu_{TMS}}{10^6 \nu_0}$$

$\nu_{titanite}$ is the resonance or Larmor frequency of [29]Si in titanite and ν_{TMS} the resonance frequency of tetramethylsilane.

Experimental conditions

NMR measurements took place at the Ruhr-Universität, Bochum, on a Superconducting FT-NMR Spectrometer ASX 400 WB with a magnetic field B_0 of 9.397 T, 7 mm MAS NMR probe (spinning rate of 7.0 kHz for Cardiff and 4.0 kHz Rauris sample), radio impulse of 2 μs at 79.49 MHz (90° pulse length 5 μs), 14056-17000 scans with 10-60 s delay. Free induction

decay was Fourier transformed into frequency space by applying an additional 40 Hz Lorentzian line broadening. Measurements are shown relative to the reference Si signal of tetramethylsilane.

3.3 NMR results and discussion

^{29}Si NMR signals for Cardiff titanite slightly shifted centres between annealing steps of 600 and 950 K from -81 to -79 ppm (Table 6, Fig. 40). FWHM decreased with rising annealing temperature, starting between 950 and 1220 K (Fig. 41). The changes are related to changes seen in synchrotron diffraction experiments that show main increase of intensity and decrease in width between 600 and 850 K.
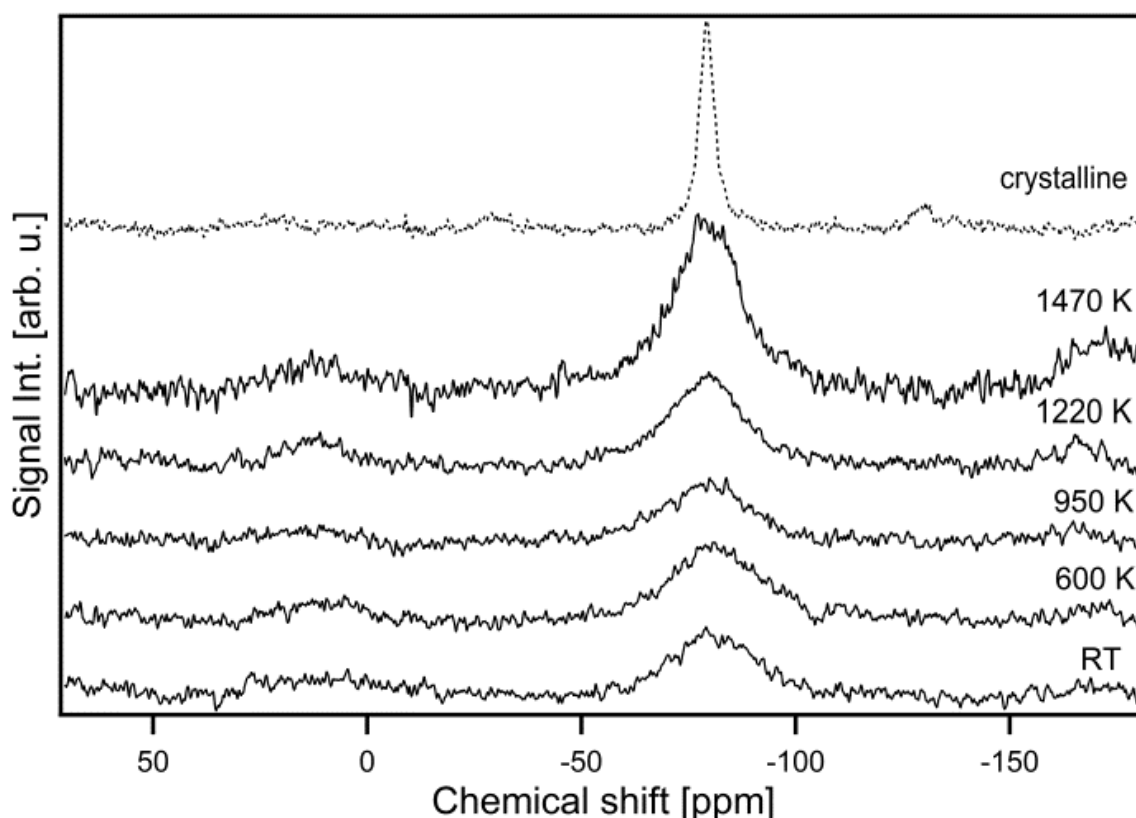

Fig. 40. ^{29}Si MAS NMR spectra of Cardiff titanite at room temperature and after 2 hours annealing at 600, 950, 1220 and 1470 K and of crystalline Rauris titanite (top dashed line).

Depending on the number of bridging oxygen atoms SiO_4 groups show a chemical shift between -65 ppm and -120 ppm in ^{29}Si MAS NMR spectroscopy (e.g. Stebbins 1995; Hawthorne *et al.* 1991, Balmer *et al.* 1997, Hartman *et al.* 1990). As a nesosilicate with four

3.3 NMR results and discussion

non-bridging oxygen atoms titanite has a single calculated shift of -79.6 ppm (Sherriff, Grundy & Hartman 1991). In their studies the authors reported a single peak with a chemical shift around -79 ppm in the ^{29}Si NMR signal attributed to the Si-O bonding which corresponds well to our observations. Although peak broadening resulting from the paramagnetic interaction of iron with the magnetic field is the main pertubating feature visible in all Cardiff NMR spectra recorded in this study, a considerable peak sharpening of the Si-O resonance frequency shift was observed at 1220 and 1470 K respectively. Signal sharpening may occur as a combination of structural ordering of the Si surrounding and a change in the paramagnetic effect of Fe. Assuming an unchanged iron surrounding of Si on annealing, the narrowing can be attributed to an ordering effect of the Si surrounding. This is also supported by a rising Lorentzian fraction (due to the oscillatory local field because of nearest neighbours) clearly indicating an increasing local order while the Gaussian component reflects the excess of a positive or negative static local magnetic field in randomly distributed nearest neighbours. Signal asymmetry in the spectra indicates the presence of more than one environment, but remains basically constant on annealing.

Additionally the paramagnetic interaction may change because of the rearrangement of iron. This would however also lead to a change of the signal shape. While the signal of well crystalline Rauris titanite with almost no radiation damage shows a peak width well below 10 ppm (Rauris sample), the Cardiff titanite had a FWHM of 19 ppm even at the highest annealing temperature (1470 K). The signal suggests that even at the highest annealing temperature a damaged structure with varying Si-O-Ti bond lengths and angles remains, which was also reported by Hawthorne *et al.* (1991). Supposedly this occurs mainly in the Ti-O bonds since these are reported to vary stronger upon heating in crystalline titanite (e.g. Kek *et al.* 1997, Hawthorne *et al.* 1991, Beirau *et al.* 2012).

In contrast to the measurements by Hawthorne *et al.* (1991) an NMR signal could be detected at room temperature. The authors pointed out that the dependence of the ^{29}Si signal on iron might be more complex than just its content since a sample with comparable iron fraction - but a lower degree of metamictisation - showed a clear NMR signal. Hawthorne *et al.* (1991) assumed that either present Fe^{2+} or enhanced quenching by paramagnetic defects with increasing radiation damage might disturb the signal. In nature Ti^{4+} is partially replaced by trivalent iron which can be reduced further and/or rearranged upon metamictisation. This should not have happened to our sample because a controlled O^{2-} fugacity was applied upon annealing.

3.3 NMR results and discussion

Table 6. Pseudo-Voigt fit (constrained Gaussian and Lorentzian width) to the ^{29}Si MAS NMR peaks.

Sample	Position (ppm)	FWHM (ppm)	Shape factor
Cardiff, RT	-81	24	1
Cardiff, 600 K	-81	24	0.6(1)
Cardiff, 950 K	-79	24	0.7(2)
Cardiff, 1220 K	-79	20	0.4(1)
Cardiff, 1470 K	-79	19	0.2(1)
Rauris, RT	-79.3	4.1	0.3(1)

The XRD data of annealed crystalline titanite indicate that the Si-O distances and angles hardly vary until at least 530 K (Kek *et al.* 1997) in contrast to the Ti-O bonds. Changes in the second and higher coordination sphere are considered to lead to strong disorder in the metamict state.
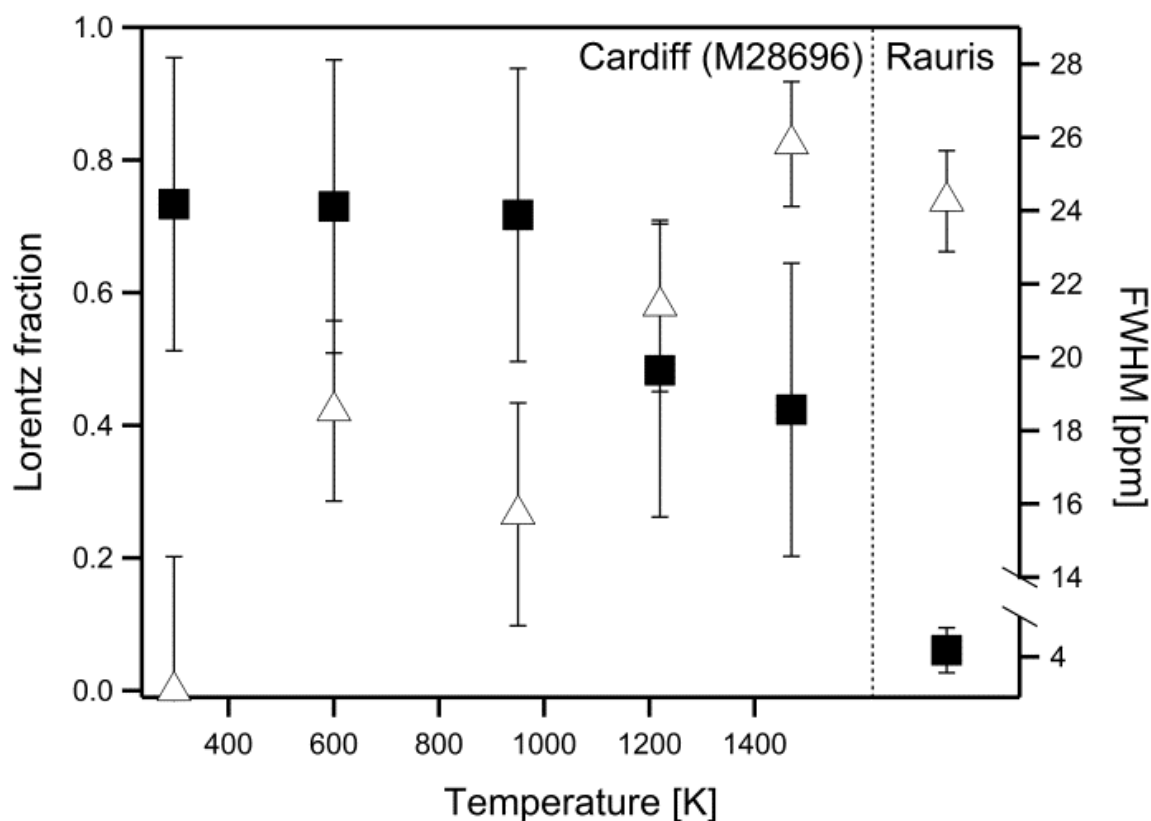
3.3 NMR results and discussion

Fig. 41. FWHM (■) and Lorentz fraction (△) of a Pseudo-Voigt fit to the ^{29}Si MAS NMR signals of Cardiff titanite at room temperature and after 2 hours annealing at 600, 950, 1220 and 1470 K respectively.

The synchrotron XRD studies of the Bragg peak ($\bar{1}3\bar{1}$) show a clear-long range restructuring on annealing between 600 and 850 K (Fig. 42). Paulmann *et al.* (2000) observed a sharpening of the Bragg reflection (080) in Cardiff titanite between 600 and 800 K, applying 15 minutes in-situ annealing progressively. In this temperature range there is no significant change of the NMR signal, possibly indicating that the influence of the paramagnetic iron dominates in the lower temperature range. Another explanation could be that local restructuring of the Si environment only occurs at higher temperatures. In their analysis of synthetic titanite gel Hartman *et al.* (1990) found that originally amorphous material crystallised progressively during 1-hour-annealing steps at 1073, 1273 and 1573 K. Major structural ordering took place between 1073 and 1273 K. Although recrystallisation from the amorphous state will differ significantly from that of the metamict structure, its ^{29}Si NMR recrystallisation temperature range corresponds to that observed here for metamict Cardiff titanite.
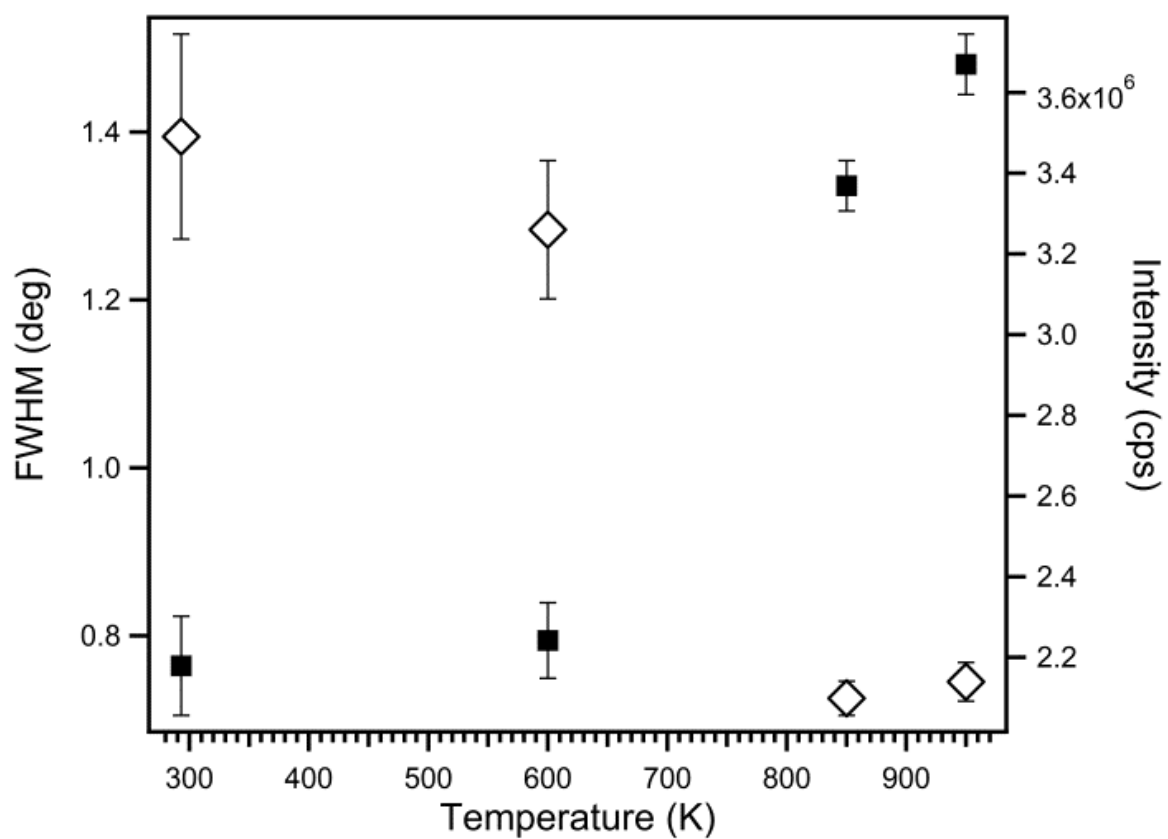
3.3 NMR results and discussion

Fig. 42. Synchrotron X-ray diffraction intensity (■) and FWHM (◇) of the ($\overline{1}3\overline{1}$) reflection of Cardiff titanite at room temperature and after annealing.

4 Conclusions

Radiation-damaged pyrochlore recrystallizes in dependence of the initial degree of metamictization. While the radiation-undamaged Schelingen reference pyrochlore showed no recrystallization at all, Panda Hill and Blue River pyrochlores with an initial amorphous fraction of 28 and 85 % started to recrystallize at low temperatures (~500 K). Metamict pyrochlores from Zlatoust and Miass, however, showed recrystallization only above 800 K. The amorphous fraction was reduced in Panda Hill from 28 % to 14 %, in Blue River from 85 % to 8 % and in Miass from 100 % to 23 % after annealing at T = 1000 K.

The observed differences in the recrystallization lead to a picture of highly recrystallization resistant metamict pyrochlore (Miass) and a significantly less resistant structure with some initial crystalline clusters (Blue River). Recrystallization of the fully metamict phase takes place in a very narrow temperature window and at the highest annealing temperature of all probed samples. Initially existing crystalline clusters in the Blue River sample result in a stepwise recrystallization process. The weakly radiation-damaged pyrochlore recrystallized rather continuous starting at low annealing temperature. Thermogravimetry showed that the recrystallization is not accompanied by a significant weight loss.

The observed Raman bands of all samples deviate from theoretically predicted modes and are very broad, due to chemical impurities and radiation damage. Nevertheless, the degree of local order could be successfully obtained from the ratio between integrated intensities of prominent spectral features (*e.g.* Raman bands around 605 to 680 cm^{-1} and 810 to 860 cm^{-1} for pyrochlore). According to the longer-ranging X-ray diffraction the thermal recrystallization happens in the temperature interval 500 to 700 K for Panda Hill, 650 to 800 K for Blue River and 800 to 850 K for Miass while the local Raman probe finds recrystallization in ranges 500 to 800 K for Panda Hill, 550 - 620 K for Blue River and 820 - 850 K for Miass, respectively.

High amounts of U and Ta lead to the formation of local modes in the Blue River pyrochlore. This effect occurs above 560 K when the material is still disordered (Fig. 3c) and impurity interactions of U/Ta-O stretching modes become prominent (Fig. 6b). This has been observed in natural pyrochlore for the first time.

4 Conclusions

For radiation-damaged Cardiff titanite, local structural ordering in the vicinity of silicon within can – in the context with XRD and previous TEM results (Beirau *et al.*, 2012) – be correlated with the decrease of FWHM of ^{29}Si MAS NMR signals with rising annealing temperature, with the strongest decrease between 950 and 1220 K. This is supported by an increasing Lorentzian fraction in the peak shape on annealing at higher temperatures.

Information on integrated long-range recrystallisation on heating was derived from synchrotron XRD data with major effects taking place between 600 and 850 K. The ^{29}Si NMR signal responds at higher annealing temperatures. We assume that the interference of Fe paramagnetism is too large to reveal local ordering in this temperature range while recrystallisation-induced peak shape changes dominate at higher annealing temperatures.

Bibliography

Aluri, E.R. & Grosvenor, A.P., 2014. An investigation of the electronic structure and structural stability of $RE_2Ti_2O_7$ by glancing angle and total electron yield XANES. *Journal of Alloys and Compounds*, 616, pp. 516–526.

Anderson, P.W., 1958. Absence of Diffusion in Certain Random Lattices. *Physical Review*, 109(5), pp. 1492–1505.

Archer, A. *et al.*, 2014. Order parameter and connectivity topology analysis of crystalline ceramics for nuclear waste immobilization. *Journal of Physics: Condensed Matter*, 26(48), p. 485011.

Arden, K.M. & Halden, N.M., 1999. Crystallization and Alteration History of Britholite in Rare-Earth-Element-Enriched Pegmatitic Segregations Associated with the Eden Lake Complex, Manitoba, Canada. *The Canadian Mineralogist*, 37, pp.1239–1253.

von Ardenne, M., 1938. The electron scanning microscope: Practical realization. *Z. Techn. Phys.*, 19, pp.407–416.

Arenas, D.J. *et al.*, 2010. Raman study of phonon modes in bismuth pyrochlores. *Physical Review B - Condensed Matter and Materials Physics*, 82(21), pp.1–8.

Atencio, D. *et al.*, 2010. The pyrochlore supergroup of minerals: Nomenclature. *Canadian Mineralogist*, 48(3), pp.673–678.

Balmer, M. L. *et al.*, 1997. Solid-state Si-29 MAS NMR study of titanosilicates. *J. Phys. Chem. B*, 101, pp. 9170-9179.

Begg, B.D. *et al.*, 2001. Heavy-ion irradiation effects on structures and acid dissolution of pyrochlores. *Journal of Nuclear Materials*, 288(2-3), pp.208–216.

Beirau, T., 2012. Annealing induced recrystallization of radiation damaged titanite and allanite. *PhD thesis*, Universität Hamburg.

Beirau, T. *et al.*, 2010. Structural phenomena of metamict titanite : a synchrotron, X-ray diffraction and vibrational spectroscopic study. *Phase Transitions*, 83(9), pp.694–702.

Bell, K. & Blenkinsop, J., 1987. mantle heterogeneity Nd and Sr isotopic compositions of East African carbonatites : Implications for mantle heterogeneity. *Geology*, 15(February), pp. 99–102.

Berger, V., Singer, D. & Orris, G., 2009. Carbonatites of the World, Explored Deposits of Nb and REE - database and Grade and Tonnage Models. *USGS Report 2009-1139*, pp. 1–17.

Berzelius, J.J., 1815. Undersökning af Gadolinitens sammansättning. In *Afhandlingar i fysik, kemi och mineralogi, Volume 4*, pp. 217–236.

Bismayer, U., 1988. New Developments in Raman Spectroscopy on Structural Phase Transitions. Physical Properties and Thermodynamic Behaviour of Minerals. *NATA ASI Ser. C, Mathematical and Physical Sciences*, 225, Reidel, Dordrecht, pp. 143-183.

Bismayer, U. 1990. Hard Mode Raman Spectroscopy and its Application to Ferroelastic and Ferroelectric Phase Transitions. *Phase Transitions*, 27, pp. 211-267.

Bismayer, U. *et al.*, 2010. Local phenomena in metamict titanite. *Acta Physica Polonica A*, 117(1), pp. 74–77.

Bragg, W.H. & Bragg, W.L., 1913. The Reflection of X-rays by Crystals. *Proceedings of the Royal Society A*, 88(605), p. 428.

Bibliography

Cai, L., Arias, A.L. & Nino, J.C., 2011. The tolerance factors of the pyrochlore crystal structure. *Journal of Materials Chemistry*, 21(11), p. 3611.

Carpena, J. *et al.*, 1988. Evidence of the contrasted fission-track clock behavior of the apatites from In Ouzzal carbonatites (northwest Hoggar): the low-temperature thermal history of an Archean basement. *Geological Society of America Bulletin*, 100(8), pp. 1237–1243.

Castaing, R. & Guinier, A., 1950. Sur l'exploration et l'analyse élémentarie d'un echantillon par une sonde électronique. *Proceedings 1st Intl. Conf. on Electron Microscopy, Delft*, p. 60-63.

Chang, I.F. & Mitra, S.S., 1971. *Long wavelength optical phonons in mixed crystals*,

Dana, J.D., Dana, E.S. & Gaines, R. V, 1997. *Dana's New Mineralogy: The System of Mineralogy of James Dwight Dana and Edward Salisbury Dana*, Wiley.

Digeos, A.A. *et al.*, 2003. Hot-pressed glass matrix composites containing pyrochlore phase particles for nuclear waste encapsulation. *Advanced Engineering Materials*, 38, pp. 1597–1604.

Dobal, P.S. *et al.*, 2001. Structural modifications in titania-doped tantalum pentoxide crystals: A raman scattering study. *International Journal of Inorganic Materials*, 3(2), pp. 135–142.

Ewing, R.C., 2011. Actinides and radiation effects: impact on the back-end of the nuclear fuel cycle. *Mineralogical Magazine*, 75(4), pp. 2359–2377.

Ewing, R.C. *et al.*, 1988. Metamict minerals: natural analogues for radiation damage effects in ceramic nuclear waste forms. *Nuclear Instruments and Methods in Physics Research B*, 32, pp. 487–497.

Ewing, R.C. *et al.*, 1982. Scientific Basis for Nuclear Waste Management. In S. V. Topp, ed. *MRS Symposium Proceedings*. Elsevier Science Publishing, Aitken, South Carolina.

Ewing, R.C., 1994. The metamict state: 1993 — the centennial. *Nuclear Instruments and Methods in Physics Research Section B: Beam Interactions with Materials and Atoms*, 91(1-4), pp. 22–29.

Ewing, R.C., 2006. The Nuclear Fuel Cycle: A Role for Mineralogy and Geochemistry. *Elements*, 2(6), pp. 331–334.

Ewing, R.C. & Headley, T.J., 1983. Alpha-recoil damage in natural zirconolite ($CaZrTi_2O_7$). *J Nucl Mater*, 119, pp. 102–109.

Ewing, R.C., Weber, W.J. & Lian, J., 2004. Nuclear waste disposal-pyrochlore ($A_2B_2O_7$): Nuclear waste form for the immobilization of plutonium and "minor" actinides. *Journal of Applied Physics*, 95(11 I), pp. 5949–5971.

Eyal, Y. & Fleischer, R.L., 1985. Preferential leaching and the age of radiation damage from alpha decay in minerals. *Geochimica et Cosmochimica Acta*, 49(5), pp. 1155–1164.

Eyal, Y. & Fleischer, R.L., 1985. Timescale of natural annealing in radioactive minerals affects retardation of radiation-damage-induced leaching. *Nature*, 314, pp. 518–520.

Eyal, Y., Lumpkin, G.R. & Ewing, R.C., 1987. Natural Annealing of alpha-recoil Damage in Metamict Minerals of the Thorite Group. *Mat. Res. Soc. Symp. Proc.*, 84, pp. 635–643.

Fechtelkord, M., 2004. Solid state NMR spectroscopy as supporting method in Rietveld structure refinements of rock-forming minerals: New developments and examples. In *EMU Notes in Mineralogy*, Eötvös University Press, Budapest, 6, pp. 421-463.

Bibliography

Fischer, M., Malcherek, T. & Bismayer, U., 2008. Structure and stability of $Cd_2Nb_2O_7$ and $Cd_2Ta_2O_7$ explored by *ab initio* calculations. *Physical Review B*, 78, p.114108.

Friedrich, W., Knipping, P. & Laue, M. v., 1913. Interferenzerscheinungen bei Röntgenstrahlen. *Annalen der Physik*, 346(10), pp. 971-988.

Geisler, T. *et al.*, 2004. Low-temperature aqueous alteration of crystalline pyrochlore: correspondence between nature and experiment. *Mineralogical Magazine*, 68(6), pp. 905–922.

Goldschmidt, V.M., 1924. No Title. *Norsk Ak., Skr.*, 1(5), p.51.

Greegor, R.B. *et al.*, 1989. Characterization of radiation damage at the Nb site. *Mat. Res. Soc. Symp. Proc.*, 127, pp.261–268.

Greegor, R.B. *et al.*, 1985. Investigation of annealed and metamict pyrochlore minerals by X-ray absorption spectroscopy. *Mat. Res. Soc. Symp. Proc.*, 44, pp. 655–662.

Gregg, D.J. *et al.*, 2013. Crystal chemistry and structures of uranium-doped gadolinium zirconates. *Journal of Nuclear Materials*, 438(1-3), pp. 144–153.

Günzler, H., 2003. IR-Spektroskopie - Eine Einführung. *Wiley-VCH*, Weinheim.

Gunn, D.S.D. *et al.*, 2012. Novel potentials for modelling defect formation and oxygen vacancy migration in $Gd_2Ti_2O_7$ and $Gd_2Zr_2O_7$ pyrochlores. *Journal of Materials Chemistry*, 22(11), p. 4675.

Hartman, J. S., Millard, R. L. & Vance, E. R., 1990. A ^{29}Si magic angle spinning NMR and DTA study of thermal crystallization of sphene and zircon gels. *Journal of Materials Science*, 25, pp. 2785-2790.

Hawthorne, F.C. *et al.*, 1991. Alpha-decay damage in titanite. *American Mineralogist*, 76(C), pp. 370–396.

Hedin, A., 1997. *SKB Technical Report 97-13*, Stockholm.

Hemminger, W. & Cammenga, H., 1989. Methoden der Thermischen Analyse, *Springer Verlag*, Berlin.

Holland, H.D. & Gottfried, D., 1955. The effect of nuclear radiation on the structure of zircon. *Acta Crystallographica*, 8(6), pp. 291–300.

Hong, W., Huiling, D. & Xi, Y., 2003. Structural study of Bi_2O_3-ZnO-Nb_2O_5 based pyrochlores. *Materials Science and Engeneering B*, 99, pp. 20–24.

Hurley, P.M. & Fairbairn, H.W., 1953. Radiation damage in zircon: a possible age method. *Geol Soc Am Bull*, 64, pp. 659–674.

Icenhower, J.P. *et al.*, 2003. Dissolution Kinetics of Titanate-Based Ceramic Waste Forms : Results from Single-Pass Flow Tests on Radiation Damaged Specimens, *Pacific Northwest National laboratory PNNL-14252*, Richland, Washington.

International Atomic Energy Agency, 2015. *Nuclear Technology Review 2015*, Wien.

Jafar, M. *et al.*, 2014. Phase evolution and microstructural studies in $CaZrTi_2O_7$ (zirconolite)–$Sm_2Ti_2O_7$ (pyrochlore) system. *Journal of the European Ceramic Society*, 34(16), pp. 4373–4381.

Kamba, S. *et al.*, 2002. Anomalous broad dielectric relaxation in $Bi_{1.5}Zn_{1.0}Nb_{1.5}O_7$ pyrochlore. *Physical Review B*, 66(5), pp.1–8.

Kek, S. *et al.*, 1997. The two-step phase transition of titanite, $CaTiSiO5$: a synchrotron

Bibliography

radiation study. *Z.Kristallogr.*, 212, pp. 9-19

Knoll, M. & Ruska, E., 1932. Das Elektronenmikroskop. *Z. Physik*, 78, pp. 318–339.

Krasnobaev, A. A. *et al.*, 2010. Zirconology of calcite carbonatite of the Vishnevogorsk massif, southern Urals. *Doklady Earth Sciences*, 431(1), pp. 390–393.

Kroumova, E. *et al.*, 2003. Bilbao Crystallographic Server : Useful Databases and Tools for Phase-Transition Studies. *Phase Transitions*, 76(1-2), pp. 155–170.

Kulriya, P.K. *et al.*, 2015. In-situ high temperature irradiation setup for temperature dependent structural studies of materials under swift heavy ion irradiation. *Nuclear Instruments and Methods in Physics Research Section B: Beam Interactions with Materials and Atoms*, 342, pp. 98–103.

Lafuente, B. *et al.*, 2015. The power of databases: The RRUFF prject. In T. Armbruster & R. M. Danisi, eds. *Highlights in Mineralogical Crystallography*.,W. De Gruyter, Berlin, pp. 1–30.

Larson, A.C. & Von Dreele, R.B., 2004. General Structure Analysis System (GSAS). *Structure*, 748(LAUR 86-748), pp. 86–748.

Li, Y., Zhu, X. & Kassab, T. a., 2014. Atomic-scale microstructures, Raman spectra and dielectric properties of cubic pyrochlore-typed $Bi_{1.5}MgNb_{1.5}O_7$ dielectric ceramics. *Ceramics International*, 40(6), pp. 8125–8134.

Lian, J. *et al.*, 2003. The order-disorder transition in ion-irradiated pyrochlore. *Acta Materialia*, 51(5), pp. 1493–1502.

Lima-de-Faria, J., 1958. Heat Treatment of Metamict Euxenites, Polymignites, Yttrotantalites, Samarskites, Pyrochlores, and Allanites. *Mineralogical Magazine*, 31(242), pp. 937–942.

Lippolt, H., Gentner, J. W. & Wimmenauer, W., 1963. Altersbestimmungen nach der Kalium-Argon-Methode an tertiären Eruptivgesteinen Südwestdeutschlands. *Jahreshefte des Geologischen Landesamtes Baden-Württemberg*, 6, p. 507.

Lummen, T.T. a *et al.*, 2008. Phonon and crystal field excitations in geometrically frustrated rare earth titanates. *Physical Review B - Condensed Matter and Materials Physics*, 77(21), pp. 1–11.

Lumpkin, G.R., Ewing, R.C. & Chakoumakos, B.C., 1986. Alpha-recoil damage in zirconolite ($CaZrTi_2O_7$). *J. Mater. Res.*, 1(4), pp. 564-576.

Lumpkin, G.R., Foltyn, E.M. & Ewing, R.C., 1986. Thermal recrystallization of alpha-recoil damaged minerals of the pyrochlore structure type. *Journal of Nuclear Materials*, 139, pp. 113–120.

Lumpkin, G.R. & Ewing, R.C., 1988. Alpha-decay damage in minerals of the pyrochlore group. *Physics and Chemistry of Minerals*, 16(1), pp. 2–20.

Lumpkin, G.R., Ewing, R.C. & Eyal, Y., 1988. Preferential leaching and natural annealing of alpha-recoil tracks in metamict betaflte and samarskite. *Journal of Materials Research*, 3(02), pp. 357–368.

Lumpkin, G.R., 2001. Alpha-decay damage and aqueous durability of actinide host phases in natural systems. *Journal of Nuclear Materials*, 289(1-2), pp. 136–166.

Lumpkin, G.R. *et al.*, 2004. Geochemical behaviour of host phases for actinides and fission products in crystalline ceramic nuclear waste forms. *Geological Society, London, Special Publications*, 236(1), pp. 89–111.

Bibliography

Lumpkin, G.R. & Geisler-Wierwille, T., 2012. Minerals and natural analogues. In *Comprehensive Nuclear Materials*, 1st ed., Elsevier Inc., Amsterdam.

Lumpkin, G.R., Leung, S.H.F. & Ferenczy, J., 2012. Chemistry , microstructure , and alpha decay damage of natural brannerite. *Chemical Geology*, 291, pp. 55–68.

Lumpkin, G.R., Smith, K.L. & Blackford, M.G., 2001. Heavy ion irradiation studies of columbite, brannerite, and pyrochlore structure types. *Journal of Nuclear Materials*, 289(1-2), pp. 177–187.

Manara, D. & Renker, B., 2003. Raman spectra of stoichiometric and hyperstoichiometric uranium dioxide. *Journal of Nuclear Materials*, 321(2-3), pp. 233–237.

Mathieu, R. *et al.*, 2001. Alteration of monazite and zircon and lead migration as geochemical tracers of fluid paleocirculations around the Oklo-Okélobondo and Bangombé natural nuclear reaction zones (Franceville basin, Gabon). *Chemical Geology*, 171(3-4), pp. 147–171.

Meija, J. *et al.*, 2016. Atomic weights of the elements 2013 (IUPAC Technical Report). , 88(3), pp. 265–291.

Meldrum, A., Wang, L.M. & Ewing, R.C., 1996. Ion beam induced amorphization of monazite. *Nuclear Instruments and Methods in Physics Research Section B: Beam Interactions with Materials and Atoms*, 116(1-4), pp. 220–224.

Meschede, D., 2004. Gerthsen Physik 22. ed. D. Meschede, ed., *Springer-Verlag*, Berlin, Heidelberg, New York.

Mihailova, B. *et al.*, 1997. Raman spectroscopy study of pyrochlore Pb2Sc0.5Tal.506.5 crystals. *Solid State Communications*, 103(11), pp. 623–627.

Moll, S. *et al.*, 2011. Irradiation damage in $Gd_2Ti_2O_7$ single crystals: Ballistic versus ionization processes. *Physical Review B - Condensed Matter and Materials Physics*, 84(6).

Nasdala, L. *et al.*, 2001. Metamictisation of natural zircon: accumulation versus thermal annealing of radioactivity-induced damage. *Contributions to Mineralogy and Petrology*, 141(2), pp. 125–144.

Nasdala, L. *et al.*, 2004. Raman spectroscopy: Analytical perspectives in mineralogy research. In *EMU Notes in Mineralogy*, Eötvös University Press, Budapest.

Park, S. *et al.*, 2014. Swift heavy ion irradiation-induced amorphization of La2Ti2O7. *Nuclear Instruments and Methods in Physics Research Section B: Beam Interactions with Materials and Atoms*, 326, pp. 145–149.

Paulmann, C., Bismayer, U. & Groat, L.A., 2000. Thermal annealing of metamict titanite: A synchrotron radiation and optical birefringence study. *Z.Kristallogr.*, 215, pp. 678-682

Radhakrishnan, a N. *et al.*, 2011. Influence of disorder-to-order transition on lattice thermal expansion and oxide ion conductivity in $(Ca_{(x)}Gd_{(1-x)})_2(Zr_{(1-x)}M_{(x)})_2O_7$ pyrochlore solid solutions. *Dalton transactions*, 40(15), pp. 3839–3848.

Raman, C. V, 1928. A new radiation. *Indian J. Phys.*, 2(March), pp. 387–398.

Reed, S.J.B., 2005. *Electron Microprobe Analysis and Scanning Electron Microscopy in Geology*, Cambridge University Press, Cambridge.

Ronconi, C.M. & Alves, O.L., 2003. Structural evolution and optical properties of $Cd_2Nb_2O_7$ films prepared by metallo-organic decomposition. *Thin Solid Films*, 441(1-2), pp. 121–

129.

Salje, E.K.H., Chrosch, J. & Ewing, R.C., 1999. Is "metamictization" of zircon a phase transition? *American Mineralogist*, 84(7-8), pp. 1107–1116.

Sattonnay, G. *et al.*, 2010. Phase transformations induced by high electronic excitation in ion-irradiated $Gd_2(Zr_xTi_{1-x})_2O_7$ pyrochlores. *Journal of Applied Physics*, 108(10), p. 103512.

Sattonnay, G. & Tétot, R., 2014. Atomic scale simulations of pyrochlore oxides with a tight-binding variable-charge model : implications for radiation tolerance. *J. Phys.: Condens. Matter*, 26, p. 10.

Scheerer, T., 1840. Untersuchung des Allanit, Orthit, Cerin und Gadolinit. *Annalen der Physik*, 127(12), pp. 465–505.

Sherriff, B. L., Grundy, H. D. & Hartman, J. S., 1991. The relationship between Si-29 MAS NMR chemical-shift and silicate mineral structure. *European Journal of Mineralogy*, 3, pp. 751-768.

Shoup, S.S. *et al.*, 1997. Aqueous leachability of lanthanide and plutonium titanates. *Journal of Nuclear Materials*, 240(2), pp. 112–117.

Sinclair, W. & Ringwood, A.E., 1981. Alpha-recoil damage in natural zirconolite and perovskite. *Geochem J*, 15, pp. 229–243.

Smekal, A.G.S., 1923. Zur Quantentheorie der Dispersion. *Naturwissenschaften*, 11(43), pp. 873–875.

Speer, J.A. & Gibbs, G. V, 1976. The crystal structure of synthetic titanite, $CaTiOSiO_4$, and the domain textures of natural titanites. *American Mineralogist*, 61, pp. 238–247.

Stebbins, J.F. 1995. Nuclear magnetic resonance spectroscopy of silicates and oxides in geochemistry and geophysics. In Ahrens, T. J., Eds., Handbook of Physical Constants. *American Geophysical Union*, Washington D.C.

Strachan, D.M. *et al.*, 2005. Radiation damage effects in candidate titanates for Pu disposition: Zirconolite. *Journal of Nuclear Materials*, 345(1), pp. 109–135.

Strunz, H. & Nickel, E., 2001. *Strunz Mineralogical Tables. Ninth Edition*, Schweizerbart Science Publishers, Stuttgart.

Tomašić, N. *et al.*, 2008. Metamict Minerals : an Insight into a Relic Crystal Structure Using XRD , Raman Spectroscopy , SAED and HRTEM. *Croatica Chemica Acta*, 81(2), pp. 391–400.

Trachenko, K.O., Dove, M.T. & Salje, E.K.H., 2001. Atomistic modelling of radiation damage in zircon. *Journal of Physics: Condensed Matter*, 13(9), pp. 1947–1959.

Urusov, V.S., Grechanovsky, a E. & Eremin, N.N., 2014. Molecular dynamics study of self-radiation damage in $Gd_2Zr_2O_7$ and $Gd_2Ti_2O_7$ pyrochlores. *Doklady Physics*, 59(6), pp. 263–266.

Vance, E.R. & Metson, J.B., 1985. Radiation damage in natural titanites. *Physics and Chemistry of Minerals*, 12(5), pp. 255–260.

Vandenborre, M.T. *et al.*, 1983. Rare-earth Titanates and Stannates of Pyrochlore Structure ; Vibrational Spectra and Force Fields. *Journal of Raman Spectroscopy*, 14(2), pp. 63–71.

Vandenborre, M.T. & Husson, E., 1983. Comparison of the Force Field in Various Pyrochlore Families. I. The A2B2O7 Oxides. *Journal of Solid State Chemistry*, 50, pp. 362–371.

Vegard, L., 1916. VI. Results of Crystal Analysis. *The London, Edinburgh, and Dublin*

Bibliography

Philosophical Magazine and Journal of Science, 32(187), pp. 67–97.

Viladkar, S., Bismayer, U. & Zietlow, P., in print. Metamict U-rich pyrochlore of Newania Carbonatite, Udaipur, Rajasthan, India. *Journal of the Geological Society of India*.

Weber, W.J., 1981. Ingrowth of lattice defects in alpha irradiated UO2 single cystals. *Journal of Nuclear Materials*, 98, pp. 206–215.

Weber, W.J. *et al.*, 1998. Radiation effects in crystalline ceramics for the immobilization of high-level nuclear waste and plutonium. *Journal of Materials Research*, 13(06), pp.1434–1484.

Wöhler, C., 1826. Ueber den Pyrochlor, eine neue Mineralspezies. In *Poggendorffs Annalen der Physik und Chemie*, Verlag J. A. Barth, Leipzig.

Yudintsev, S. V *et al.*, 2015. The behavior of rare-earth pyrochlores and perovskites under ion irradiation. *Doklady Earth Sciences*, 461(1), pp. 247-253.

Zietlow, P. *et al.*, 2014. ^{29}Si MAS NMR spectroscopy and synchrotron XRD study of metamict Cardiff titanite. *Z.Kristallogr.*, 229, pp. 551-554.

Zietlow, P. *et al.*, in print. Thermal annealing of natural, radiation-damaged pyrochlore. *Z.Kristallogr.*

Zhang, M. *et al.*, 2001. Hydrous species in crystalline and metamict titanites. *American Mineralogist*, 86(7-8), pp. 904–909.

Zhang, M. *et al.*, 2002. Metamictization and recrystallization of titanite: An infrared spectroscopic study. *American Mineralogist*, 87(7), pp. 882–890.

Curriculum vitae

Personal

Name	Peter Zietlow
Date of Birth	05.08.1978
Place of Birth	Northeim
Office address	Universität Hamburg
	Mineralogisch-Petrographisches Institut
	Grindelallee 48
	D-20146 Hamburg
	Fax: +49(0)40 42838-2422
	Phone: +49(0)40 42838-2484
	e-mail: peter.zietlow@mineralogie.uni-hamburg.de

Education

05/2013 – 11/2016   Doctorate studies at University Hamburg, Germany. Research on temperature induced recrystallization of metamict minerals.

10/2009 – 03/2013   ***M. Sc. Geowissenschaften***, emphasis on geomaterials; Georg-August University Göttingen; Germany.

Title of master thesis: „*Textur- und Mikrostrukturanalysen an hochfesten, mikrolegierten HSLA-Stählen*"

10/2006 – 09/2009   ***B. Sc. Geowissenschaften***, Georg-August University Göttingen, Germany.

08/1999 – 06/2002   ***Diplom Verwaltungsbetriebswirt (FH)***, Nds. Fachhochschule für Verwaltung und Rechtspflege, Hannover, Germany.

Professional experience

07/2002 – 12/2006   Administration of local EU programme „LEADER+ im Göttinger Land", Göttingen district, Germany.

Teaching activities

2013-2016   Assistance to Dr. Paulmann for BSc exercise course "Basiswissen Kristallographie"

List of publications

Zietlow, P., Beirau, T., Groat, L. A., Paulmann, C. and Bismayer, U.: ^{29}Si MAS NMR spectroscopy and synchrotron XRD study of metamict Cardiff titanite. Z.Kristallogr., 2014, 229, 551.

Viladkar, S.G., Bismayer, U. and **Zietlow, P.**: Metamict U-rich pyrochlore of Newania Carbonatite, Udaipur, Rajasthan, India. Journal of the Geological Society of India, in print.

Zietlow, P., Beirau, T., Mihailova, B., Groat, L. A., Chudy, T., Shelyug, A., Navrotsky, A., Ewing, R. C., Schlüter, J., Škoda, R. and Bismayer, U.: Thermal annealing of natural, radiation-damaged pyrochlore. Z.Kristallogr., in print.

Contributions to conferences

Zietlow, P., Beirau, T., Mihailova, B., Malcherek, T., Schlüter, J., Paulmann, C., Škoda, R. Groat, L.A. and Bismayer, U.: Metastability and crystallisation of metamict minerals. Deutsche Mineralogische Gesellschaft, Tübingen, 15.09.-19.09.2013, poster presentation.

Zietlow, P., Beirau, T., Mihailova, B., Groat, L.A., Paulmann, C., and Bismayer, U.: XRD and ^{29}Si NMR study of metamict minerals. Deutsche Kristallographische Gesellschaft, Berlin, 17.03.-20.03.2014, poster presentation.

Zietlow, P., Beirau, T., and Bismayer, U.: Recrystallization behaviour of radiation damaged pyrochlore and titanite. Workshop "Radiation damage in structures – Relevance for nuclear waste disposal", Hamburg, 14.07.-15.07.2014, oral presentation.

Zietlow, P., Beirau, T., Groat, L.A., Paulmann, C., and Bismayer, U.: Recrystallisation study of radiation damaged titanite and pyrochlore. Deutsche Mineralogische Gesellschaft, Jena, 21.09.-24.09.2014, poster presentation.

Zietlow, P., Beirau, T., Mihailova, B., and Bismayer, U.: Thermal annealing phenomena of metamict pyrochlores. Deutsche Kristallographische Gesellschaft, Göttingen, 16.03.-19.03.2015, oral presentation.

List of publications

Zietlow, P. and Bismayer, U.: Thermal annealing phenomena of metamict titanite and pyrochlore. Berichtskolloquium SPP 1415, Bad Sooden-Allendorf, 05.05.-06.05.2015, poster presentation.

Zietlow, P., Beirau, T., Mihailova, B., Schlüter, J., Paulmann, C., Škoda, R. Groat, L.A. and Bismayer, U.: Thermal annealing behaviour of radiation damaged pyrochlore. Deutsche Mineralogische Gesellschaft, Berlin, 04.10.-07.10.2015, poster presentation.

Zietlow, P., Beirau, T., Mihailova, B., Schlüter, J., Paulmann, C., Škoda, R. Groat, L.A. and Bismayer, U.: Thermal annealing of radiation damaged minerals. Deutsche Kristallographische Gesellschaft, Stuttgart, 14.03.-17.03.2016, poster presentation.

Zietlow, P. and Bismayer, U.: Thermal annealing phenomena of metamict pyrochlores. Abschlusskolloquium SPP 1415, Wetzlar, 15.06.-17.06.2016, poster and oral presentation.

Acknowledgements

Eidesstattliche Versicherung

Declaration on oath according to § 7 (4) doctoral degree regulations of MIN faculty

Hiermit erkläre ich an Eides statt, dass ich die vorliegende Dissertationsschrift selbst verfasst und keine anderen als die angegebenen Quellen und Hilfsmittel benutzt habe.

I hereby declare, on oath, that I have written the present dissertation by my own and have not used other than the acknowledged resources and aids.

Hamburg, den 03.08.2016   Unterschrift / signature